Two-stage lumen expansion in a human epiblast model is driven by apical actin polymerization followed by osmotic pressure

Dhiraj Indana[1], Andrei Zakharov[2], Youngbin Lim[3], Alexander R. Dunn[4], Nidhi Bhutani[5], Vivek B. Shenoy[2,6] and Ovijit Chaudhuri[1,7#]*

[1] Department of Mechanical Engineering, Stanford University, Stanford, CA 94305 USA

[2] Department of Materials Science and Engineering, University of Pennsylvania, Philadelphia, PA 19104 USA

[3] Cell Sciences Imaging Facility (CSIF), Beckman Center, Stanford University School of Medicine, Stanford, CA 94305 USA

[4] Department of Chemical Engineering, Stanford University, Stanford, CA 94305 USA

[5] Department of Orthopaedic Surgery, Stanford University School of Medicine, Stanford, CA 94305 USA

[6] Center for Engineering Mechanobiology, University of Pennsylvania, Philadelphia, PA 19104 USA

[7] Chemistry, Engineering, and Medicine for Human Health (ChEM-H), Stanford University, Stanford, CA 94305 USA

[*] Corresponding author

[#] Lead contact

e-mail(s): chaudhuri@stanford.edu (corresponding author)

Summary

Post-implantation, the pluripotent epiblast in a human embryo forms a central lumen, paving the way for gastrulation. Osmotic pressure gradients are considered the drivers of lumen expansion across development, but their role in human epiblasts is unknown. Here, we study lumenogenesis in a pluripotent-stem-cell-based epiblast model using engineered hydrogels. We find that leaky junctions prevent osmotic pressure gradients in early epiblasts, and instead, forces from apical actin polymerization drive lumen expansion. Once the lumen reaches a radius of ~12 μm, tight junctions mature, and osmotic pressure gradients develop to drive further growth. Computational modelling indicates that apical actin polymerization into a stiff network mediates initial lumen expansion and predicts a transition to pressure driven growth in larger epiblasts to avoid buckling. Human epiblasts show transcriptional signatures consistent with these mechanisms. Thus, actin polymerization drives lumen expansion in the human epiblast, and may serve as a general mechanism of early lumenogenesis.

Introduction

During human embryonic development, the fertilized egg undergoes multiple rounds of cell division and differentiation to form the pluripotent epiblast at the blastocyst stage, which ultimately gives rise to all tissues in the fetus[1]. Embryo development from the pluripotent epiblast commences upon implantation of the blastocyst into the uterine wall, following which pluripotent stem cells self-organize to form a roughly spherical structure containing a fluid-filled lumen[2]. Lumens or fluid-filled cavities are a ubiquitous feature of metazoans and are often evolutionarily linked to the origin of body-plan complexity[3]. Proper formation of the epiblast lumen is critical for establishing morphogen gradients that drive subsequent embryonic development[4,5]. While the physical mechanism of lumen expansion in the human epiblast is unknown, established mechanisms of de novo lumenogenesis in other model systems involve apoptosis or osmotic pressure gradients[6,7]. Apoptosis drives lumenogenesis in certain mammary epithelial models where cells at the center of a cluster die, resulting in a hollow cavity[8]. Osmotic pressure gradients drive lumen growth in the mouse blastocyst[9-11], MDCK (Madin-Darby canine kidney) cells[12], bile canaliculi[13], and zebrafish inner ear[14]. In each of these cases, apico-basally polarized cells with tight junctions, pump osmolytes into the lumen which builds osmotic pressure and drives water into the lumen, expanding its volume[15,16]. While pressure has been shown to drive lumen expansion in the mouse blastocyst[9-11], mechanisms of lumen expansion in other early embryonic lumens such as the epiblast cavity are much less understood[17,18]. Importantly, mouse epiblasts cannot be used to fully understand human epiblast morphogenesis as they exhibit key morphological differences with human epiblasts – pluripotent stem cells in mouse epiblasts form a hollow cup shaped structure fused with extraembryonic cells called the egg cylinder whereas in humans epiblasts, pluripotent stem cells form a hollow roughly spherical structure[18]. Recently, the study of polarity[19] and pluripotency[20] dynamics necessary for epiblast lumenogenesis have provided key insights into the cellular processes involved, but the physics driving lumen expansion in the human epiblast remains unclear.

Human induced pluripotent stem cell (hiPSC) models of the embryo reproduce key aspects of development and serve as excellent tools to uncover mechanisms orchestrating human embryogenesis[21,22], since human embryos cannot be studied directly due to ethical concerns. hiPSCs have been previously used to model the human epiblast using basement membrane based matrices[20,23-26] such as Matrigel as well as using engineered hydrogels[27]. We have previously

shown that hiPSCs form lumen-containing structures that morphologically and phenotypically model the human epiblast in a highly reproducible manner, when cultured in 3D in engineered hydrogels which model the confinement experienced by the epiblast in vivo due to blastocyst cavity pressure and extraembryonic cells[27]. In this epiblast model (hereafter referred to as hiPSC epiblast), we now dissect the mechanisms regulating lumen expansion. Epiblast lumen nucleation is initiated by exit from naïve pluripotency and subsequent transition to formative and primed pluripotency[20,26,28] through polarization events mediated by cytoskeletal proteins[29] involving the formation of a specialized structure called the apicosome[30]. However, the physical mechanism of lumen expansion in the human epiblast following initial polarization is unknown. Our experiments and simulations reveal a previously undescribed mechanism of lumen expansion mediated by apical actin polymerization that drives early lumen expansion up to a critical lumen size of ~12 μm radius, followed by a transition to osmotic pressure gradient driven lumen growth in lumens larger than 12 μm radius.

Results

hiPSCs form epiblast-like structures in 3D hydrogels

We formed hiPSC epiblasts by culturing single hiPSCs in 3D viscoelastic alginate hydrogels. In the presence of specific biophysical cues of hydrogel stiffness, viscoelasticity, and cell-adhesion ligand (RGD) density, hiPSCs self-organize into lumen-containing structures that are reminiscent of the human epiblast[27]. While the initial elastic modulus of the hydrogels is 20 kPa, these gels exhibit fast stress relaxation, with a stress relaxation half time of ~70 s (Figure S1A). Further, the relaxation modulus over ~30 mins is ~1 kPa, which is on the same order of magnitude as that experienced by the epiblast cells in the mouse blastocyst[10] (Figure S1A). Thus, these hydrogels roughly mimic the confinement faced by the epiblast in the human blastocyst, however, the precise values of human blastocyst pressure and mechanical contribution of extraembryonic cells are unknown. In these hydrogels, hiPSCs proliferate and begin to form lumens around day 3 of culture, creating 3D monolayered cellular structures with a central, roughly spherical lumen (Figures 1A and 1B). Similar to human epiblasts[20,31,32], these structures polarized along the apicobasal axis in response to matrix signaling[27] and maintained expression of pluripotency proteins such as Oct4, Sox2 and Nanog, as well as formative pluripotency factors

such as Otx2[28,33], over 7 days of culture (Figures 1C, S1B and S1C). hiPSC clusters also mirrored the morphological features of human epiblasts. The numbers of cells in hiPSC clusters on different days of culture were akin to human epiblasts, with day 3 and day 7 of in vitro culture corresponding to 7 to 8 days post fertilization (d.p.f.) and 11 to 12 d.p.f in human embryos respectively, suggesting similar proliferation dynamics (Figure 1D). Further, lumen volumes and growth rates of hiPSC clusters were close to those of human epiblasts (Figure 1E). Nuclear morphology metrics such as area and perimeter of hiPSC clusters were also similar to those of human epiblasts (Figure S1D). Overall, hiPSCs in engineered 3D alginate hydrogels maintained pluripotency, polarized along the apicobasal axis, and showed lumenal and nuclear morphological similarities to human epiblasts. Therefore, these structures model the human epiblast, allowing study of mechanisms driving epiblast lumen expansion.

Osmotic pressure gradients and apoptosis do not drive lumen expansion

We sought to understand the mechanisms underlying lumen expansion in hiPSC epiblasts as a model of human epiblasts. Guided by previous studies of lumenogenesis[6,7], we first investigated known mechanisms of de novo lumenogenesis including apoptosis and osmotic pressure gradients. During lumen growth in hiPSC epiblasts, few to none apoptotic cells were detected (Figures S1E to S1G), demonstrating that apoptosis does not drive lumen expansion in hiPSC epiblasts, consistent with previous studies[34].

We next studied the role of osmotic pressure gradients in driving lumen expansion. To build osmotic pressure in the lumen, two requirements need to be met: (i) ion flux into intercellular space or lumen at the apical surface[15], and (ii) formation of tight junctions to prevent osmolytes from leaking[35] (Figure 1F). These requirements allow osmotic pressure to build up, which draws water into the lumen, generating force necessary for lumen growth. To test if hiPSCs formed tight junctions, cell-impermeable fluorescent dextran was added to the culture media. If mature tight junctions were present, dextran would be expected to be excluded from the lumen. Strikingly, dextran entered lumens smaller than ~12 μm in radius, indicating that hiPSCs do not form mature tight junctions during early stages of lumen expansion when the lumen size is below ~12 μm radius (Figures 1G to 1H and S2A to S2H). Dextran also localized to the intercellular spaces in junctions between cells and was excluded from cells themselves suggesting that dextran entered lumens

through diffusion along the intercellular spaces and not via other mechanisms such as transcytosis (Figures S2I and S2J). As tight junction marker ZO-1 localized to the cell-cell boundary of smaller lumens as well (Figure S2K), it was plausible that tight junction formation was gradual with a complete seal forming at a lumen size of ~12 μm radius. But this was not the case. Large macromolecular dextran, with a diameter (~12 nm; 70 kDa dextran) comparable to intercellular space due to adherens junctions (~20 nm)[36,37], entered lumens smaller than ~12 μm in radius but was excluded from lumens larger than this size, highlighting the complete lack of mature tight junctions in hiPSC epiblasts with smaller lumens (Figures 1H and S2G to S2H).

As mature tight junctions were absent in hiPSC epiblasts with smaller lumens (radius < 12 μm; hereafter referred to as smaller epiblasts), any ions pumped into these lumens are expected to leak along the intercellular spaces, preventing large pressures from building up. To confirm that this was the case, diffusion dynamics in smaller lumens were measured by observing fluorescence recovery after photobleaching (FRAP) of dextran. The fluorescence signals recovered ~2 min after photobleaching, suggesting that dextran can freely diffuse along the intercellular spaces (Figures 1I to 1K; Video S1). Taken together, these results reveal a lumen size-dependent initiation of tight junction formation, with lumens below ~12 μm in radius being leaky.

To further assess the role of osmotic pressure gradients in driving lumenogenesis, lumen shapes were examined. Lumen shapes are expected to be convex or bent outward if pressure was the sole driver of epiblast lumenogenesis, whereas irregularly shaped lumens that are bent inwards suggest that osmotic pressure gradients are not a dominant driver of lumen growth[38]. Lumen shapes were highly irregular for smaller lumens but transitioned to a more bulged, convex shape in larger lumens (Figure 1L to 1N). Thus, the irregularly shaped lumens in smaller epiblasts further indicate that osmotic pressure is not a major driver of early lumenogenesis in hiPSC epiblasts, whereas the regularly shaped lumens in larger epiblasts indicate that osmotic pressure gradients could drive lumen expansion in larger lumens. Finally, laser ablation through an entire cell in smaller epiblasts did not cause any drastic change in cell or lumen size or shape indicating that smaller lumens are not pressurized (Figure S2L). Taken together, the lack of tight junctions, free diffusion out of the intralumenal space, and lumen shapes together indicate that initial expansion of the lumen is not driven by osmotic pressure gradients and emphasize the existence of a pressure-independent mechanism of lumenogenesis.

Early lumen expansion is associated with force generation and formation of an apical actin mesh

As epiblast lumenogenesis mechanisms are required to produce forces necessary to overcome resistance from their environment – the surrounding hydrogel in case of the hiPSC epiblast versus extraembryonic cells and blastocyst cavity pressure in case of the human epiblast – we next examined force generation associated with lumenogenesis in order to gain insight into the underlying mechanisms driving early lumen expansion. hiPSC epiblasts of all sizes generated local matrix deformations on the order of tens of micrometers over 18 hr (Figures 2A and 2B; Video S2). As the hydrogels are viscoelastic and viscoplastic, with stresses relaxed on a timescale of minutes and the material undergoing permanent deformation, the magnitude of forces required for the measured matrix deformations depends on the timescale and dynamics of force application. Nonetheless, as some force generation is necessary, we next probed different cellular force generating machineries to uncover the pressure-independent mechanism responsible for epiblast lumenogenesis.

We first examined the role of actomyosin contractility in lumen expansion, given the well-known function of the actomyosin cytoskeleton network in generating contractile forces. Myosin II was mostly punctate and largely localized at the basal surface, which could not explain the pattern of forces associated with lumen expansion (Figures 2C and S3A). Further, inhibition of actomyosin contractility on day 3 of culture or in smaller epiblasts (lumen radius < 12 μm) as well as on day 7 or in larger epiblasts (lumen radius > 12 μm) (Figure 2D), did not significantly impact lumen formation (Figures 2E and S3B). These results demonstrate that actomyosin contractility does not drive lumen expansion in hiPSC epiblasts.

We next examined actin structures and their potential role in driving lumen expansion, as actin polymerization in bundled or branched networks produces protrusive forces that drive cellular morphogenesis in a variety of contexts[39]. In hiPSC epiblasts, F-actin was densely localized at the apical surface (Figure 2F). Super-resolution microscopy using an Airyscan system revealed that apically, F-actin formed a dense mesh-like structure with microvilli protruding from this mesh (Figure 2G). Further, actin nucleation factor N-WASP and actin branching complex Arp2/3 were enriched at the apical surface, which would be expected to promote the formation of a dendritic

actin network (Figure 2H). As formation of a lumen and apical surface are intertwined, the time evolution of the apical actin mesh formation was quantified. Apical surface area per cell increased in size as lumens grew but reached an equilibrium size of ~100 μm^2 at a lumen size of ~12 μm radius (Figures 2I, S3C and S3D). In fact, all cells in larger epiblasts had a similar apical surface area of ~100 μm^2 while cells in smaller epiblasts had a wide range of apical surface areas at any given timepoint that were close to or less than 100 μm^2, highlighting cell-cell variations in apical surface formation (Figure 2J). Distinct lumen growth dynamics were observed for smaller and larger lumens while cell volume and thickness stayed relatively constant (Figures S3E to S3G). Overall, these data show that as lumens form, cells grow their apical surfaces up to an equilibrium value, which is achieved at a lumen size of ~12 μm radius, coinciding with the timing of tight junction formation.

We next tested whether actin polymerization could drive early lumen expansion using inhibition studies. Dendritic actin network growth is driven by the Arp2/3 complex, which is nucleated via N-WASP, while linear actin polymerization is initiated via formins. Strikingly, inhibition of actin polymerization by any of these proteins – Arp2/3 complex, N-WASP, and formins – strongly reduced lumen formation in smaller epiblasts but had no impact on larger epiblasts (Figures 2K, 2L, S3H and S3I). Thus, actin polymerization is necessary for lumen expansion in smaller epiblasts. Given these observations, we hypothesized that the growth of apical actin in each cell generates force to drive epiblast lumen expansion in a pressure-independent manner until apical actin growth equilibrates at a lumen radius of ~12 μm.

Apical actin polymerization drives lumen expansion in smaller epiblasts

To examine how apical actin polymerization could drive lumen expansion, we first performed time-lapse imaging of fluorescently labelled F-actin during early lumen expansion. Interestingly, lumen expansion correlated with apical actin polymerization of only a few cells in the epiblast and, in some cases, specifically correlated with increase in apical length of a single cell while other cells maintained relatively constant apical lengths (Figures 3A and 3B; Video S3 top row). While apical lengths are expected to increase with increasing lumen area, it was striking to see large cell-cell variations in growth dynamics for smaller epiblasts (Figures 3C and 3D). In

line with these features, smaller epiblasts generated radially asymmetric matrix deformations (Figure 3E).

As individual cells polymerize actin to expand their apical surfaces, it would be expected that they resist each other's expansion, and that the hydrogel would resist overall lumen expansion. To study these, we first perturbed the dynamics of apical actin in cells and their neighbors by performing laser ablation of apical actin in individual cells in smaller epiblasts (Figure 3F; Video S4 top row). No immediate change in apical length was observed post ablation, suggesting that the stiff apical actin mesh is not under large levels of compression or tension (Figures 3F to 3I and S4A to S4D; Video S4 top row). As the hydrogels are both viscoelastic and viscoplastic, this observation suggested that the stresses resisting the epiblast expansion were relaxed and the hydrogel was plastically deformed, so that residual stresses remaining on the epiblast are low at any given timepoint. Over a timescale of minutes following ablation, however, apical length of the ablated cell decreased, while that of neighboring cells increased, indicating active actin polymerization driving lateral apical expansion in the neighboring cells and lateral pushing forces (Figures 3G to 3I and S4A to S4D; Video S4 top row). But, as the apical actin signal in the ablated cell began to recover, the apical length of the ablated cell expanded again, suggesting that the apical actin re-growth in the ablated cell pushes back against the neighboring cells (Figures 3G, 3H and S4A to S4D). For comparison, no substantial changes in apical lengths were observed in non-ablated controls on a timescale of minutes (Figure S5). These ablation studies directly connect actin network growth to apical expansion and indicate the following interpretation. In smaller epiblasts, cells resist the growth of apical actin in neighboring cells and when such resistance is disrupted, say via ablation, actin in cells neighboring the ablated cell, can actively polymerize, increasing their apical lengths.

To directly test if the growing hiPSC epiblasts are under compression globally from the hydrogel, we dissolved the hydrogel and observed epiblast morphology (Figure S6). hiPSC epiblasts immediately expanded in size post hydrogel dissolution indicating that epiblasts were under some compression (Figures S6A to S6C). Complementarily, following cell lysis, lumens collapsed, and the hydrogel expanded into the space formerly occupied by the epiblast, confirming that the hydrogel was under compression due to epiblast growth (Figures S6D and S6E). Overall, these observations point to quasi-static actin growth where actin polymerization generated forces

drive apical growth and lumen expansion, and stress relaxation and plasticity in the hydrogel prevent large compression from building up in hydrogel and thus in the apical actin mesh as well.

Under the idea that actin polymerization at the apical surface of single cells drives lumen growth, cell-cell variations in actin polymerization rate and corresponding apical actin mechanics in smaller epiblasts, should result in a wide distribution of apical curvatures (Figures 2J and 3A to 3D). Analysis of lumen curvature showed a broad range of local curvatures in smaller lumens, as cells build their apical surfaces (Figures 3J to 3L). However, once all cells reach a mature apical size with a dense apical actin mesh, which is the case in larger epiblasts (Figures 2I and 2J), apical surfaces became uniformly flatter (Figures 3J to 3L). Taken together, these results show that apical actin polymerization at the apical surface of single cells drives lumen expansion.

Computational model of apical actin polymerization driven lumen expansion

In order to gain insight into the physical mechanisms governing lumen expansion and to investigate the role of actin polymerization in this process, we developed a theoretical model and conducted computational simulations. Before exploring the mechanisms responsible for driving lumen expansion, we first wanted to understand cellular geometric constraints that govern lumen shapes and sizes, agnostic to the specific mechanism driving lumen expansion. In order to do so, we employed a particle-based description of cells to recapitulate lumen size and shape (Figure 4A). Our model incorporated two key geometric constraints observed in experiments as lumens grew: (i) constant cell volume (Figure S3F), and (ii) constant cell layer thickness or cleft length (Figures S3G). These observations imply that cells act effectively as incompressible objects during lumen expansion and can readily adapt their shape to form a confluent layer around the lumen. Based on these assumptions, the predicted apical lengths and number of cells as a function of lumen size (defined in Equations 1 and 2 in Supplementary Methods) from the model were in excellent agreement with the experimental observations (Figures 4B to 4D). The model predicted rapid growth of apical surface area of individual cells in smaller epiblasts (Figure 4C). In larger epiblasts, however, growth of the apical surface in individual cells is predicted to stall (Figures 4B and 4C), in line with experimental observations (Figures 2I and 2J). These predictions independently point to rapid apical growth as a potential mechanism of lumen expansion in smaller epiblasts. As our experiments revealed apical actin polymerization to be responsible for rapid

growth of the apical surface and subsequently lumen expansion, we next assessed the role of apical actin polymerization as well as other physical mechanisms in driving lumen expansion.

To better understand the physics of how apical actin polymerization can drive lumen expansion, we developed a continuum model considering a cell cluster in an elastic hydrogel with a nascent lumen at the interior of the cluster. Cells actively polymerize apical actin allowing rapid growth of the apical surface. Cells in the model also pump ions through the apical and basal surfaces. Water fluxes are driven by osmotic and hydrostatic pressure gradients that result from ion flux and actin-generated stress respectively, but paracellular leaks can dissipate osmotic gradients (Figure 4E). In smaller clusters with leaky junctions, ion concentrations did not build up in the lumen and thus there was no difference in osmotic pressure between the lumen and the hydrogel (Figure 4F). Actin polymerization on the other hand generated stresses that counteract the resistance offered by the elastic hydrogel resulting in lumen expansion (Figure 4G). Using the Laplace relation, the pressure difference across the cell layer was estimated in the scenario of constant intracellular pressure and constant curvature of the cell surface, and accounting for passive and active stresses in the apical actin network (as detailed in Equations 6-9 in Supplementary Methods). Actin stiffness determined the resulting stresses in the network when it is subject to deformation, while the undeformed length factor defines the effective change in the rest length of the apical actin network. Importantly, our model predicted that increasing stiffness of apical actin network enhances lumen growth resulting in water influx into the lumen (Figures 4H and 4I). In contrast, apical actin networks with reduced stiffness are predicted to have smaller lumens. These results highlight the importance of apical actin stiffness in mediating actin polymerization driven lumen expansion.

As the lumen expands, the enclosing cell layer becomes more susceptible to buckling due to increasing stresses in the confining hydrogel that resists the lumen expansion, so we next sought to understand the implications of buckling to lumen growth. To simplify our analysis, we assumed that the gel is elastic with a Young's modulus of 1 kPa, comparable to the relaxed modulus of the hydrogels used in experiments (Figure S1A; Supplementary Methods Table 1), and the cell layer is incompressible, with a Young's modulus of 20 kPa as measured previously in epithelial monolayers[40]. Now, as lumens expand, pressure in the hydrogel is expected to increase while the pressure that the cell layer can withstand[41] without buckling reduces (Figure 4J). Hence, there is a critical lumen size at which the pressure exerted by the hydrogel exceeds the critical buckling

pressure of the cell monolayer, causing it to buckle (Figure 4J). For the Young's modulus of the cell monolayer and modulus of the gel assumed above, the critical lumen size is about 12 μm. To facilitate lumen expansion beyond this critical size, development of lumenal pressure is required to counterbalance the hydrogel pressure, thereby preventing buckling of the cell layer, as buckling is not observed physiologically.

Overall, our computational model for smaller epiblasts demonstrates that apical actin polymerization, which results in growth and stiffening of the apical surface, is sufficient for lumen expansion, even without osmotic pressure gradients. However, modeling predicts that a transition to pressure driven growth is required once the lumen reaches a certain size to avoid cell layer buckling due to increased stress from the surrounding hydrogel.

Mechanism of lumen growth switches to osmotic pressure in larger epiblasts

As apical actin polymerization is equilibrated in larger epiblasts, and given the predicted transition to pressure-driven growth in the modeling, we next examined the mechanism driving further growth of these lumens. Concomitant with the maturation of the apical surfaces (Figures 2I to 2L) at a lumen radius of ~12 μm, hiPSC epiblasts form mature tight junctions (Figures 1G, 1H, S2D to S2H and S2K), which could allow osmotic pressure to build inside the lumen. Further, these lumens have convex, bulged out shapes (Figures 1L to 1N). Overall, these characteristics are consistent with osmotic pressure driven lumen growth[16].

To test if osmotic pressure was responsible for growth of larger lumens, we performed time-lapse imaging. Unlike actin polymerization driven lumen growth, apical lengths of most cells in larger epiblasts generally increased over time and positively correlated with increase in lumen area (Figures 5A to 5D; Video S3 bottom row). Subsequently, larger epiblasts generated radially uniform matrix deformations as they grew (Figures 5E to 5G). Pressure-driven growth is governed by Young-Laplace law, which necessitates cells to be under tension to balance the lumenal pressure[10,12]. Thus, laser ablation of apical actin was performed to examine if cells were under tension or compression. Ablated cells exhibited an immediate increase in apical length post-ablation revealing that cells were under tension (Figures 5H to 5K and S4E to S4H; Videos S4 bottom row and S5). With time, apical length of ablated cells increased further while no change in neighboring cells was observed (Figures 5H to 5K and S4E to S4H; Videos S4 bottom row and

S5). Overall, these results provide strong evidence that osmotic pressure drives lumen growth in larger epiblasts.

To better understand the physics of osmotic pressure driven lumen growth, we applied our numerical model to larger epiblasts with tight junctions. The model enabled us to determine the equilibrium cell and lumen sizes depending on the passive and active ion transport across the cell layer, passive leak through the cleft or intercellular space, as well as the number and mechanical properties of the cells forming the layer (Section B in Supplementary Methods for detailed analysis). For simplicity, we assumed constant properties of the surrounding matrix and cell cortex, although in general they might exhibit nonlinear responses to applied stress. Other relevant parameter values are summarized in Supplementary Methods Table 1. In this case, ion pumping into the lumen increased osmotic pressure and resulted in robust lumen growth (Figures 5L and 5M). Predicted lumen sizes were in excellent agreement with experimental observations (Figure 5N). Balance between apical and basal ion pumping was found to be critical for buildup of osmotic pressure (Figure 5M). Higher basal pumping without apical pumping, and vice versa, prevented accumulation of ions in the lumen and no lumen growth occurred (Figure 5M). Overall, our experiments and model indicate that ion pumping in the presence of tight junctions builds osmotic pressure to drive the growth of larger lumens.

Human epiblasts upregulate actin polymerization related genes during lumen expansion

Finally, to investigate the in vivo relevance of the mechanisms discovered in hiPSC epiblasts, we analyzed transcriptional signatures of the human epiblast as a function of developmental time using single cell RNA sequencing data generated from peri-implantation human embryos[42,43]. Epiblast lumen forms soon after implantation at ~7 d.p.f and expands in volume up to gastrulation at ~14 d.p.f (Figures 1A and 1B)[2]. Based on analysis of epiblast cells from 7 to 14 d.p.f using KNN (k-nearest neighbor) clustering of UMAP (Uniform Manifold Approximation and Projection) dimensionality reduction plots, cells were divided into two subpopulations (Figures 6A and 6B). As the two epiblast subpopulations were roughly separated based on developmental time, we annotated these as early and late epiblasts (Figure 6B). As expected, early epiblast cells showed higher expression of naïve pluripotency markers such as *DNMT3L* and *KLF4* and lower expression of primed pluripotency marker *SFRP2*, as compared to late epiblast cells (Figures 6C and 6D). Interestingly, several actin polymerization related genes

including those encoding for proteins in the Arp2/3 complex such as *ARPC1B, ARPC5, ARPC2* were upregulated in the early epiblast but transitioned to a lower expression level in the late epiblast (Figure 6E and 6F). This is consistent with the expectation from our hiPSC epiblast findings where cells actively build a branched apical actin network at earlier stages of lumen expansion but transition to an equilibrium apical size at later stages (Figure 2I). Similar transcriptional signatures were observed in a different single cell RNA sequencing dataset[43] of 8-12 d.p.f human embryos as well (Figure 6G to 6L). Altogether, the upregulation of actin polymerization genes early in lumenogenesis are suggestive that actin polymerization may drive early lumen expansion in the human epiblast, as we have found in hiPSC epiblasts in this study.

Discussion

Taken together, our experimental and simulation results uncover the physical mechanisms of lumen expansion in hiPSC epiblasts. hiPSC epiblasts closely model the morphology and phenotype of human epiblasts. We describe two distinct lumen-size-dependent mechanisms that generate the force necessary for lumen expansion. hiPSC epiblasts with lumen smaller than ~12 μm radius lack mature tight junctions, allow free diffusion of ions and macromolecules between the lumen and the hydrogel, and prevent large osmotic pressures from building up. Lumen growth in these smaller epiblasts is driven by actin polymerization into a dense network on the apical surface via N-WASP, Arp2/3 and formins. Force generation by actin polymerization, aided by rapid stress relaxation in the hydrogel, ultimately drives lumen growth and overall expansion of the hiPSC epiblast in the hydrogel (Figure 7). When apical actin mesh in individual cells reaches a defined equilibrium size at a lumen radius of ~12 μm, coinciding with the formation of tight junctions, the mechanism of lumen growth switches to osmotic pressure gradient driven (Figure 7). Lastly, transcriptional expression profiles of human epiblasts suggest the existence of similar mechanisms in vivo as those discovered in hiPSC epiblasts.

Mechanisms of human epiblast lumenogenesis have been difficult to explore owing to ethical concerns, technical challenges with in vitro culture of human embryos and limitations of stem-cell models of the human epiblast[18]. Matrigel or reconstituted basement membrane dependent models of the human epiblast provide a limited window into lumen growth as cells quickly differentiate in culture[24,27], thus only allowing the study of early polarization and lumen opening

events[19,25,30]. In mice, while peri-implantation development is significantly different from humans, a few different mechanisms have been suggested to play a role in epiblast lumenogenesis: (i) electrostatic repulsion between apically deposited anti-adhesive proteins such as podocalyxin which have a high negative charge[34] and (ii) lumenal fluid transport due to osmotic gradients[44]. However, these mechanisms do not provide complete physical explanations for sustained lumen expansion. While anti-adhesive proteins such as podocalyxin can help create a "non-stick" apical surface, electrostatic repulsive forces are negligible on a length scale of microns due to Debye-Hückel screening in electrolyte solutions[15]. While podocalyxin plays an important role in establishing cell polarity and potentially in lumen nucleation, direct contribution of podocalyxin to sustained lumen expansion is not expected. Directed fluid transport on the other hand does not in itself generate force for lumen expansion unless the fluid is pressurized or accompanied by other cellular force generating mechanisms. By using engineered hydrogels which provide a prolonged window into human epiblast lumen expansion, we rule out these suspected mechanisms and discover a force generating mechanism responsible for sustained lumen growth.

Here, we discovered a mechanism of actin-polymerization-driven lumen expansion in the human epiblast, which may be relevant to other contexts in development. Actin polymerization and assembly into branched networks via Arp2/3 complex is known to generate pushing forces and drive several cellular processes including lamellipodial protrusions during migration, vesicle trafficking and polarization[45,46]. Further, actin forces generated by actin polymerization at the apical surface have been proposed to drive apical surface and/or junction expansion in other systems, including *Xenopus* embryos[47] and *Drosophila* eye[48]. Such actin structures also play a vital role during early embryogenesis[46,49]. For example, expanding apical actin rings in a pre-implantation mouse embryo push cells against each other, stabilizing cell-cell junctions[50] and allowing the formation of a pressurized blastocyst cavity[10]. While these actin rings help seal the mouse embryo before lumen formation[50], the actin structures we discovered in hiPSC epiblasts serve to expand lumens and are distinct from those observed in the mouse blastocyst. We find that in hiPSC epiblasts, apical actin polymerization and formation of a branched actin mesh generates force to drive initial lumen expansion. Theoretical modeling confirms that actin polymerization forces and network stiffness are sufficient to drive lumen growth. Apical actin as well as actomyosin networks are a common feature of epithelia, but the structural features of apical actin mesh and how actin polymerization is physically aligned to drive lumenogenesis are yet to be

explored. As this is the first time that actin polymerization forces have been considered as a driving force for lumen expansion, it is possible that this mechanism could be relevant to other contexts in development. Several tissues including the zebrafish gut[51], *Drosophila* lung[52] and MDCK cysts[38] have lumenal surfaces that are bent inwards and have dense apical actin. Because osmotic-pressure driven growth is expected to result in bulged out lumens, osmotic pressure driven growth might not explain early lumenal growth in these other contexts.

The existence of two distinct mechanisms of lumen growth, dependent on a critical lumen size at which tight junction formation and apical maturation occur, highlights close crosstalk between the cell polarity machinery, growth of apical domains, tight junctions, and lumen size. Cell geometries are also tightly controlled with cell volume and thickness staying roughly constant during both actin polymerization and osmotic pressure driven lumen growth. Further, cell-layer stretching and cycles of lumen inflation and collapse, which are characteristic of pressure driven lumen growth in other model systems[9,10,12,14], are not observed in hiPSC epiblasts, suggesting that pressures generated in the epiblast are relatively low. While high pressures are useful for disrupting structures such as zona pellucida during blastocyst hatching[17], they could cause tissue rupture[10,12] and compromise embryo integrity. Moreover, lumen volumes and cell numbers closely follow a power law relationship during pressure driven growth, highlighting a careful balance between pressure magnitude and cell number, thereby allowing cells to maintain a fixed volume and thickness. Such control over embryo size could be pivotal for subsequent embryonic patterning events such as amnion formation and gastrulation by establishing appropriate signaling gradients[4,5,44,53]. Notably, we did also find mechanisms of robustness in this system. While inhibition of actin polymerization disrupts early lumen formation, lumens ultimately form as cells multiply even with continuous actin inhibition, highlighting the presence of alternate mechanisms of epiblast lumenogenesis to ensure robust development, but such a delay in lumenogenesis could possibly impact other developmental processes. Overall, our results provide a quantitative understanding of the mechanisms that drive epiblast lumenogenesis and suggest that size control and robustness are inherently coded into these mechanisms.

Limitations of the study

While 3D live imaging of apical surface would improve visualization of actin polymerization driven lumen growth, live imaging of hiPSC epiblasts with high z-resolution was not possible due to phototoxicity effects upon increased laser exposure. hiPSC epiblasts replicate many features of the human epiblast, but a few key differences remain. For example, our epiblast model does not undergo amnion formation, an event that coincides with epiblast cavity growth. Moreover, our model lacks extraembryonic cells and their corresponding biochemical signals. The role of extraembryonic cells and mechanisms of amnion formation require further investigations. Also, several new questions arise about the function of the epiblast lumen. While the epiblast lumen has been suggested to shield the epiblast cells from extraembryonic signaling to ensure robust gastrulation[54], the existence of size-dependent mechanisms of lumen growth points to a larger role for the epiblast lumen in regulating embryo size and orchestrating embryonic development. To our knowledge, the actin polymerization driven lumen growth mechanism discovered here is the only force-generating, pressure-independent lumenogenesis mechanism and could be at play in other model systems as well. Finally, our theoretical model assumes that 3D lumens retain their symmetric spherical shape during both stages of expansion, allowing us to simplify our analysis to the 2D geometry of the mid-plane cross-section to elucidate the underlying mechanisms. However, the modeling of elongated lumens will require inclusion of more sophisticated geometries and consideration of stress anisotropy. In conclusion, this study advances our understanding of human embryonic development and expands our knowledge of the biological toolkits that cells utilize to make a lumen.

Acknowledgments

The authors gratefully acknowledge all current and past members of the Chaudhuri Lab for helpful discussions. The authors acknowledge the Stanford Cell Sciences Imaging Facility (CSIF) for microscope (Zeiss lattice light sheet 7 and Zeiss LSM 780 inverted multiphoton laser scanning confocal microscope) and software access (Imaris). The authors acknowledge Gordon Wang, Ph.D., and the Stanford Neuroscience Microscopy Service for access to and help with super-resolution microscopy (Zeiss Airyscan2 LSM 980 inverted confocal microscope). The authors thank Zeiss specialists Win Zaw, Ph.D. and Benjamin Figueroa, Ph.D. for help with joint deconvolution (jDCV) processing of Airyscan2 super-resolution images. The authors thank Dr.

Vittorio Sebastiano (Department of Obstetrics and Gynecology, Stanford University) for providing the hiPSC line derived from BJ fibroblasts and Dr. Marc Levenston (Department of Mechanical Engineering, Stanford University) for use of mechanical testing equipment (Instron). This work was supported by a Stanford School of Engineering Graduate Fellowship to D.I., a Stanford Bio-X Interdisciplinary Initiatives Program Seed grant for O.C. and N.B., and a National Science Foundation grant MCB 2148041 for O.C.

Author contributions

D.I. and O.C. conceived and designed the experiments. D.I. performed the experiments, data analysis, and statistical tests. D.I. and Y.L. performed experiments using light sheet microscopy. A.Z. and V.B.S performed computational simulations and analysis. N.B. and A.R.D. contributed to experimental design and provided analytical guidance. D.I., A.Z., V.B.S. and O.C. wrote the manuscript with input from all authors.

Declaration of Interests

The authors declare that they have no competing interests.

Ethics statement

The hiPSC epiblasts used in this study lack extraembryonic cells including hypoblast and trophectoderm, and do not have human organismal potential, i.e., cannot form a whole human embryo. Furthermore, all experiments were terminated by no later than day 7 of culture. All protocols used in this work with hiPSCs have been approved by the Stanford University Stem Cell Research Oversight Committee (SCRO protocol 837).

Main figure titles and legends

Figure 1: hiPSC epiblasts model the human epiblast and osmotic pressure does not drive lumenogenesis in hiPSC epiblasts. (A) Schematic of peri-implantation human embryos and hiPSC epiblasts. **(B)** Immunostains of human and hiPSC epiblasts. Human epiblast images were generated in and modified with permission from ref.[32]. **(C)** Immunostains of Oct4, Sox2, Nanog, Otx2 (formative pluripotency), Ezrin and Podocalyxin (apical polarity) in hiPSC epiblasts. **(D)** Quantification of cell numbers in human[32] and hiPSC epiblasts (mean ± s.d.; ns: not significant $p > 0.05$, one-way ANOVA; $n = 43$ (day 3), 26 (day 5), 32 (day 7) hiPSC epiblasts; $N = 3$ biological replicates). Data for human epiblasts was generated in ref.[32]. **(E)** Correlation between lumen volume and cell numbers in human[20,24,31,32,55] and hiPSC epiblasts (mean ± s.d. for hiPSC epiblasts; $n = 16$ (human), 101 (hiPSC epiblasts)). **(F)** Schematic of osmotic pressure driven lumenogenesis. **(G)** Tight junction permeability assay. Fluorescence images of cell-impermeant dextran. **(H)** Quantification of dextran intensity inside lumen. Lines indicate sigmoidal fits and 95% CI. (n, R^2) = 3 kDa: (290, 0.71), 10 kDa: (229, 0.81), 40 kDa: (213, 0.69), 70 kDa: (228, 0.69). **(I)** Fluorescence recovery after photobleaching (FRAP) of lumenal dextran. **(J)** Normalized lumenal dextran intensity quantification for cluster shown in (I). Line (red) indicates least squares fit based on a FRAP model[56] and 95% CI. **(K)** Estimation of fluorescence recovery half-time ($\tau_{1/2}$) (mean ± 95% CI). **(L to N)** Quantification of lumen solidity. ($n = 290$ for plot (N)). Scale bars: 2 mm (A), 20 μm (B and C), 50 μm (G), 10 μm (I), 25 μm (L).

Figure 2: Early lumen expansion is associated with force generation and apical actin mesh formation. (A) Timelapse (hh:mm) images of lumen expansion and growth. Black outlines indicate lumenal surface. **(B)** Matrix deformations generated during lumen growth for clusters shown in (A). **(C)** Immunostains of myosin II, phalloidin (F-actin) and DAPI (nucleus) in hiPSC epiblasts. **(D)** Quantification of lumen radius on different days of culture (mean ± s.d.; ****$p < 0.0001$, one-way ANOVA; $n = 43$ (day 3), 26 (day 5), 32 (day 7); $N = 3$ biological replicates). **(E)** Percent epiblasts with lumen in the presence of different actomyosin contractility inhibitors (mean ± s.e.m.; ns: not significant $p > 0.05$, one-way ANOVA; $n \geq 5$; $N = 3$ biological replicates). **(F and G)** Representative confocal (F) and super-resolution (G) images of apical actin mesh. **(H)** Immunostains of Arp2/3 and N-WASP in hiPSC epiblasts. Red arrowheads highlight apical localization of Arp2/3 and N-WASP. **(I)** Quantification of average apical surface area per cell as a function of lumen size ($n = 101$ hiPSC epiblasts). **(J)** Quantification of apical surface area of individual cells in an epiblast. Shaded (gray) region indicates range (max-min) of areas per epiblast ($n = 11$ hiPSC epiblasts; ≥ 3 cells per hiPSC epiblast). **(K and L)** Representative brightfield images (K) and quantification of percent epiblasts with lumen (L) in the presence of Arp2/3 (CK-666), formin (SMIFH2) and N-WASP (Wiskostatin) inhibitors (mean ± s.e.m.; ****$p < 0.0001$, ***$p < 0.001$, **$p < 0.01$, ns: not significant $p > 0.05$, one-way ANOVA; $n = 3$; $N = 3$ biological replicates). Scale bars: 40 μm (A and B), 20 μm (C), 50 μm (F and G), 20 μm (H), 25 μm (K).

Figure 3: Apical actin polymerization drives lumen expansion in smaller epiblasts. (A) Timelapse (min) images of F-actin during lumen growth. Red outlines indicate lumenal surface. **(B)** Quantification of cell apical length and lumen area during lumen growth for epiblast shown in

(A). **(C)** Spearman correlation values between lumen area and cell apical lengths for smaller epiblasts. Rows indicate each epiblast's apical lengths correlated to corresponding lumen area. Spearman correlation values for each pair are listed and range between: 1 (perfect correlation), 0 (no correlation), and −1 (perfect anti-correlation). For Spearman correlation values > 0.5, p-value is < 0.05. Cells are listed in decreasing order of their respective Spearman correlation values. **(D)** Percent cells per epiblast whose apical lengths are positively correlated (Spearman correlation value > 0.5) with lumen area (mean ± s.d.). **(E)** Representative matrix deformations generated during lumen growth in smaller epiblasts and quantification of radial asymmetry in matrix deformation (mean ± s.d). Asymmetry index = magnitude of vector sum of deformations / average magnitude of deformations. **(F)** Apical actin ablation and recovery. Outlines indicate ablated surface. **(G)** Kymograph showing apical actin of ablated and neighboring cells for epiblast shown in (F). Length of colored lines = apical length; intensity of colored lines = average apical actin intensity. **(H)** Quantification of apical length and actin intensity of ablated and neighboring cells for smaller epiblasts. **(I)** Quantification of post-ablation and final apical lengths of ablated and neighboring cells, and lumen area for smaller epiblasts. Apical lengths of the two neighbors were averaged (mean ± s.d.; ***p < 0.001, ns: not significant p > 0.05, Mann-Whitney; $n = 8$; $N = 4$ biological replicates). **(J)** Representative cross-sectional immunostains of smaller and larger epiblasts. **(K)** 3D reconstruction of lumenal surface and quantification of Gaussian curvature for epiblasts shown in (J). **(L)** Frequency distribution of Gaussian curvature for epiblasts shown in (J). Scale bars: 10 μm (A and K), 20 μm (E, F and J), 1 μm (G).

Figure 4: Computational modeling indicates that actin polymerization forces are sufficient to drive early lumen expansion, but must transition to pressure driven growth when a critical lumen size is reached. (A to D) Schematic and predictions of an analytical model for estimating evolution of cell apical surface area and cell number with increase in lumen size, for fixed cell volume and cell thickness or cleft length. **(E)** Schematic of the theoretical model of actin polymerization driven lumen growth. Hydrogel is considered linear elastic for this model with a modulus of 1 kPa which is the relaxed modulus of viscoelastic alginate hydrogels used in experiments. $\tilde{L}_a$: initial length of apical actin mesh; L_a: final length of apical actin mesh; ξ_a: undeformed length factor; K_a: stiffness of apical actin mesh; J_a: ion flux into lumen; J_{leak}: ion leak along the leaky junctions; P_{gel}: stress exerted by the hydrogel on the cell cluster. **(F)** Model shows that osmotic pressure does not build in leaky lumens. Ions pumped into the lumen diffuse out along the leaky junctions in smaller epiblasts preventing buildup of osmotic pressure. **(G)** Cells actively polymerize apical actin that generates stress to deform the hydrogel and drive lumen expansion. Dashed line indicates spontaneous lumen opening. Cell volume and cell thickness or cleft length are assumed to be constant. **(H and I)** Plots showing that increase in apical actin stiffness (K_a) and decrease in undeformed length factor (ξ_a) result in higher lumen growth rates. Lumen growth rates as a function of apical actin stiffness (K_a) for given values of undeformed length factor (ξ_a) are shown in (I). All other parameters were kept constant. $H_a = h_b = 0.6$ μm, $R_{cell} = 6$ μm, $L_a/\tilde{L}_a = 12$, $L_b/\tilde{L}_b = 1$. **(J)** Buckling pressure considerations predict a transition to pressure-driven lumen growth at ~12 μm lumen radius to prevent cell layer buckling.

Figure 5: Osmotic pressure drives lumen growth in larger epiblasts. (A) Timelapse (min) images of F-actin during lumen expansion. **(B)** Quantification of cell apical length and lumen area

during lumen growth for epiblast shown in (A). **(C)** Spearman correlation values between lumen area and cell apical lengths for larger epiblasts. Rows indicate each epiblast's apical lengths correlated to corresponding lumen area. Cells are listed in decreasing order of their respective Spearman correlation values. **(D)** Percent cells per epiblast whose apical lengths are positively correlated (Spearman correlation value > 0.5) with lumen area (mean ± s.d.; **p < 0.01, Mann-Whitney; n = 5 (smaller epiblasts), 5 (larger epiblasts); N = 5 biological replicates). **(E)** Representative matrix deformations generated during lumen growth in larger epiblasts. **(F)** Quantification of maximum matrix deformation per hour (mean ± s.d.; **p < 0.01, Mann-Whitney; n = 8 (smaller epiblasts), 7 (larger epiblasts); N = 5 biological replicates). **(G)** Quantification of radial asymmetry in matrix deformation (mean ± s.d.; ***p < 0.001, Mann-Whitney; n = 8 (smaller epiblasts), 7 (larger epiblasts); N = 5 biological replicates). Asymmetry index = magnitude of vector sum of deformations / average magnitude of deformations. **(H)** Apical actin ablation and recovery. Red outline indicates ablated surface. **(I)** Kymograph showing apical actin of ablated and neighboring cells for epiblast shown in (H). **(J)** Quantification of apical length and actin intensity of ablated and neighboring cells for larger epiblasts. **(K)** Quantification of post-ablation and final apical lengths of ablated and neighboring cells, and lumen area for larger epiblasts. Apical lengths of the two neighbors were averaged (mean ± s.d.; **p < 0.01, ns: not significant p > 0.05, Mann-Whitney; n = 5; N = 4 biological replicates). **(L and M)** Schematic and predictions of the theoretical model of osmotic pressure driven lumen growth. Ion pumping into the lumen builds osmotic pressure as ions cannot diffuse out along tight junctions. c_{cell} is the total concentration of ions in the cells at equilibrium and c_{lum} is the total concentration of ions in the lumen at equilibrium. **(N)** Model predictions closely match experimental observations of lumen radius, number of cells and cell apical surface area of larger epiblasts. Scale bars: 20 μm (A, E and H), 1 μm (I).

Figure 6: Human epiblasts show transcriptional signatures consistent with actin polymerization driven lumen expansion. (A) UMAP plot of human epiblast cells generated from scRNA-seq data of peri-implantation human embryos[42] (71 epiblast cells) colored with timepoints (d.p.f). **(B)** KNN (k-nearest neighbor) based cell clustering. The two subpopulations are annotated as early and late epiblast. **(C to F)** Normalized expression level of naïve pluripotency genes (C), primed pluripotency genes (D), actin polymerization related genes (E) and other relevant genes (F) (median and quartiles; ****p < 0.0001, **p < 0.01, *p < 0.05, Mann-Whitney; n = 34 (early epiblast cells), 37 (late epiblast cells)). **(G)** UMAP plot of human epiblast cells generated from scRNA-seq data of peri-implantation human embryos[43] (274 epiblast cells) colored with timepoints (d.p.f) **(H)** KNN (k-nearest neighbor) based cell clustering. The three subpopulations are annotated as early, mid and late epiblast. **(I to L)** Normalized expression level of naïve pluripotency genes (I), primed pluripotency genes (J), actin polymerization related genes (K) and other relevant genes (L) (median and quartiles; ****p < 0.0001, **p < 0.01, *p < 0.05, ns: not significant p > 0.05, Kruskal-Wallis; n = 78 (early epiblast cells), 111 (mid epiblast cells), 85 (late epiblast cells)).

Figure 7: Summary of mechanisms driving lumen expansion in human epiblasts.

STAR★Methods

KEY RESOURCES TABLE

REAGENT or RESOURCE	SOURCE	IDENTIFIER
Antibodies		
Rabbit Polyclonal Anti-Oct4	Cell Signaling Technology	Cat#2750; Lot#5; RRID:AB_823583
Rabbit Monoclonal Anti-Sox2	Cell Signaling Technology	Cat#3579; Clone D6D9; Lot#8; RRID:AB_2195767
Rabbit Monoclonal Anti-Nanog	Cell Signaling Technology	Cat#4903; Clone D73G4; Lot#8; RRID:AB_10559205
Goat Polyclonal Anti-Otx2	R&D Systems	Cat#AF1979; Lot#KNO0922011; RRID:AB_2157172
Mouse Monoclonal Anti-Ezrin	Sigma-Aldrich	Cat#E8897; Clone 3C12; Lot#049M4838V; RRID:AB_476955
Mouse Monoclonal Anti-Podocalyxin	R&D Systems	Cat#MAB1658; Clone 222328; Lot#JKW0219121; RRID:AB_2165984
Mouse Monoclonal Anti-ZO-1	Thermo Fisher Scientific	Cat#33-9100; Clone ZO1-1A12; Lot#TL277395; RRID:AB_2533147
Rabbit Polyclonal Anti-phospho-myosin light chain 2	Cell Signaling Technology	Cat#3674; Lot#5; RRID:AB_2147464
Mouse Monoclonal Anti-Arp2/3 complex	Sigma-Aldrich	Cat#MABT95; Clone 13C9; Lot#3574550; RRID:AB_11205567
Rabbit Polyclonal Anti-N-WASP	Thermo Fisher Scientific	Cat#PA5-52198; Lot#WK3443175A; RRID:AB_2644914

Rabbit Polyclonal Anti-Active Caspase-3	R&D Systems	Cat#AF835SP; Lot#CFZ4223041; RRID:AB_2243952;
Alexa Fluor 555 Goat Anti-Rabbit IgG	Thermo Fisher Scientific	Cat#A21428; Lot#2192278; RRID:AB_2535849
Alexa Fluor 647 Goat Anti-Rabbit IgG	Thermo Fisher Scientific	Cat#A21244; Lot#2390713; RRID:AB_2535812
Alexa Fluor 555 Donkey Anti-Goat IgG	Thermo Fisher Scientific	Cat#A21432; Lot#1697092; RRID:AB_2535853
Alexa Fluor 555 Goat Anti-Mouse IgG1	Thermo Fisher Scientific	Cat#A21127; Lot#2384708; RRID:AB_2535769
Alexa Fluor 647 Goat Anti-Mouse IgG1	Thermo Fisher Scientific	Cat#A21240; Lot#2482960; RRID:AB_2535809
Alexa Fluor 555 Goat Anti-Mouse IgG2a	Thermo Fisher Scientific	Cat#A21137; Lot#2335727; RRID:AB_2535776
Chemicals, peptides, and recombinant proteins		
ProNova UP VLVG alginate	NovaMatrix	Cat#4200501; Batch#BP-1212-24; Batch#BP-1903-04
MES hydrate	Sigma-Aldrich	Cat#M8250
Sodium chloride	Fisher Scientific	Cat#S671
RGD peptide (GGGGRGDSP)	Peptide 2.0	Custom order
N-hydroxysulfosuccinimide (Sulfo-NHS)	Thermo Fisher Scientific	Cat#24510
N-(3-dimethylaminopropyl)-*N*'-ethylcarbodiimide hydrochloride (EDC)	Sigma-Aldrich	Cat#E6383
Hydroxylamine hydrochloride	Sigma-Aldrich	Cat#255580
DMEM/F-12	Thermo Fisher Scientific	Cat#11330057
Calcium sulfate dihydrate	Sigma-Aldrich	Cat#C3771

hESC-qualified Matrigel LDEV-free	Corning	Cat#354277
mTeSR1	STEMCELL Technologies	Cat#85850
ROCK inhibitor Y-27632	STEMCELL Technologies	Cat#72304
Accutase	STEMCELL Technologies	Cat#07920
LookOut Mycoplasma PCR Detection Kit	Sigma-Aldrich	Cat#MP0035
Paraformaldehyde	Alfa Aesar	Cat#43368-9M
Sucrose	Fisher Scientific	Cat#S5-3
O.C.T. Compound	Tissue-Tek	Cat#23-730-571
DPBS	Fisher Scientific	Cat#21-600-010
DPBS containing Ca^{2+} and Mg^{2+}	Cytiva	Cat#SH30264.01
Triton X-100	Sigma-Aldrich	Cat#T8787
Cytochalasin D	Thermo Fisher Scientific	Cat#PHZ1063
Bovine serum albumin (BSA)	Sigma-Aldrich	Cat#A4503
Goat serum	Gibco	Cat#16210072
Glycine	Fisher Scientific	Cat#G46-1
DAPI	Thermo Fisher Scientific	Cat#D1306
Alexa Fluor 488 Phalloidin	Invitrogen	Cat#A12379
Alexa Fluor 555 Phalloidin	Invitrogen	Cat#A34055
ProLong Gold antifade reagent	Life Technologies	Cat#P36930
Ethylenediaminetetraacetic acid (EDTA)	Sigma-Aldrich	Cat#E9884
SYTOX Green Nucleic Acid Stain	Thermo Fisher Scientific	Cat#S7020
3 kDa Texas Red dextran	Thermo Fisher Scientific	Cat#D3328
10 kDa Texas Red dextran	Thermo Fisher Scientific	Cat#D1828
40 kDa Texas Red dextran	Thermo Fisher Scientific	Cat#D1829
70 kDa Texas Red dextran	Thermo Fisher Scientific	Cat#D1830

Dimethyl sulfoxide (DMSO)	Fisher Scientific	Cat#BP231-100
Blebbistatin (myosin II inhibitor)	Abcam	Cat#ab120425
ML-7 (myosin light chain kinase inhibitor)	Tocris Bioscience	Cat#4310
ML-141 (selective Cdc42 Rho family inhibitor)	Tocris Bioscience	Cat#4266
CK-666 (Arp2/3 inhibitor)	Sigma-Aldrich	Cat#SML0006
SMIFH2 (formin inhibitor)	Sigma-Aldrich	Cat#S4826
Wiskostatin (N-WASP inhibitor)	Abcam	Cat#ab141085
Cytochalasin D (actin polymerization inhibitor)	Sigma-Aldrich	Cat#C8273
SiR-actin	Cytoskeleton Inc.	Cat#CY-SC001
N-acetyl-L-cysteine (NAC)	Sigma-Aldrich	Cat#A9165
1 μm diameter fluorescent carboxylate-modified microspheres (FluoSpheres)	Thermo Fisher Scientific	Cat#F8816
CellEvent Caspase-3/7 GR	Thermo Fisher Scientific	Cat#C10432
Z-VAD-FMK (pan-caspase inhibitor)	AAT Bioquest	Cat#13300
Deposited data		
Single-cell RNAseq of human in vitro cultured embryos	Xiang et al.[42]	GEO: GSE136447
Single-cell RNAseq of human in vitro cultured embryos	Zhou et al.[43]	GEO: GSE109555
Experimental models: Cell lines		
Human: RiPSC.BJ iPSC line generated through synthetic mRNA reprogramming of BJ human fibroblast cells	Durruthy-Durruthy et al.[57]; Laboratory of Vittorio Sebastiano	N/A
Human: AICS-0024 iPSC line (WTC11)	AICS	AICS-0024; RRID:CVCL_JM15
Human: PODXL-EGFP hESC line	Taniguchi et al.[30]; Laboratory of Kenichiro Taniguchi	N/A
Software and algorithms		
Original code	This paper	https://github.com/azakharov1/Lumen

FIJI/ImageJ (2.9.0)	Schindelin et al.[58]	https://imagej.net/software/fiji/
Prism (9.3.1)	GraphPad	https://www.graphpad.com/features
MATLAB (R2017b)	MathWorks	https://www.mathworks.com/products/%20matlab.html
PIVlab (2.31)	Thielicke & Sonntag[59]	https://www.mathworks.com/matlabcentral/fileexchange/27659-pivlab-particle-image-velocimetry-piv-tool-with-gui
RStudio (2023.09.1+494)	Posit	https://posit.co/download/rstudio-desktop/
Seurat (v4.2.0)	Hao et al.[60]	https://satijalab.org/seurat/
Imaris (9.9)	Bitplane	https://imaris.oxinst.com/

RESOURCE AVAILABILITY

Lead contact

Further information and requests for resources and reagents should be directed to and will be fulfilled by the lead contact, Ovijit Chaudhuri (chaudhuri@stanford.edu).

Materials availability

This study did not generate any new unique reagents.

Data and code availability

- All data reported in this paper will be shared by the lead contact upon request. This paper analyzes existing, publicly available data. These accession numbers for the datasets are listed in the key resources table.

- All original code has been deposited on GitHub and is publicly available as of the date of publication. URL is listed in the key resources table.

- Any additional information required to reanalyze the data reported in this paper is available from the lead contact upon request.

EXPERIMENTAL MODEL AND STUDY PARTICIPANT DETAILS

Cell lines and culture

Three hPSC lines were used in this study. First, was a hiPSC line (RiPSC.BJ) generated through synthetic mRNA reprogramming of BJ human fibroblast cells[57] (a gift from Dr. Vittorio Sebastiano (Department of Obstetrics and Gynecology, Stanford University)). Second, was a hiPSC line purchased from Coriell Institute (AICS-0024) in which MYH10 has been endogenously tagged with mEGFP using CRISPR/Cas9 technology in WTC-11 (GM25256) hiPSCs. Third, was a hPSC line expressing PODXL-EGFP generated using H9 human embryonic stem cells (hESCs)[30] (a gift from Dr. Kenichiro Taniguchi (Medical College of Wisconsin)). hiPSCs were first expanded to generate a large cell bank within 2 passages of purchased or gifted cells: passage 29 and 30 for MYH10-mEGFP hiPSCs and passage 16 and 17 for untagged hiPSCs. Both hiPSC lines have been authenticated by original sources for successful differentiation to the three germ layers and also authenticated in-house for pluripotency by Oct4, Sox2 and Nanog immunostaining.

hiPSCs were cultured on TC-treated 100 mm dish (Corning 430167) coated with LDEV-free hESC-qualified Matrigel (Corning 354277) in mTeSR1 media (STEMCELL Technologies) at 37°C in 5% CO_2. hiPSCs cultured in mTeSR1 were used for encapsulation in alginate hydrogels at 70% confluency as single cells using Accutase (STEMCELL Technologies) following the manufacturer's protocol. For each experiment, a new hiPSC vial (of passage numbers listed above) was thawed, cultured as described above and encapsulated in alginate hydrogels without continued passaging. This was done to ensure high-quality of hiPSCs and to maintain hiPSCs at a low passage number and normal karyotype as characterized previously[57]. Both hiPSC lines were checked for mycoplasma contamination and tested negative (LookOut Mycoplasma PCR Detection Kit, Sigma-Aldrich MP0035).

METHOD DETAILS

Alginate preparation

Sodium alginate rich in guluronic acid blocks was purchased (ProNova UP VLVG; 28 kDa molecular weight; NovaMatrix). RGD (arginine–glycine–aspartate) peptides were coupled to alginate using carbodiimide chemistry[61]. First, alginate was dissolved overnight at 1% (w/v) in a 0.1 M MES hydrate (Sigma-Aldrich M8250), 0.3 M sodium chloride (Fisher Scientific S671) buffer with a pH of 6.5. *N*-hydroxysulfosuccinimide (Sulfo-NHS, Thermo Fisher Scientific 24510), *N*-(3-dimethylaminopropyl)-*N*'-ethylcarbodiimide hydrochloride (EDC, Sigma-Aldrich E6383) and GGGGRGDSP (Peptide 2.0) peptide were sequentially mixed in the alginate solution and the reaction was allowed to proceed for 20 hr until quenched by adding hydroxylamine hydrochloride (Sigma-Aldrich 255580). The alginate was then dialyzed in deionized water for 3 days, purified with activated charcoal, sterile filtered, frozen, lyophilized and stored at -20°C. For cell encapsulation, lyophilized alginate was reconstituted at 3% (w/v) in serum-free DMEM/F-12 (Thermo Fisher Scientific 11330057). Reconstituted 3% (w/v) alginate was diluted with solution containing cells and crosslinked using calcium sulfate (Sigma-Aldrich C3771) to make hydrogels with 2% (w/v) final alginate concentration, initial elastic modulus of 20 kPa, loss tangent of ~0.08, stress relaxation half-time of ~70 s, and 1500 μM RGD density as described previously[27]. Detailed protocols for RGD-conjugation of alginate, preparation of alginate hydrogels and exact recipes for alginate hydrogels used in this study have been published previously[27,62].

Hydrogel mechanical characterization

Compression tests were performed using an Instron 5848 MicroTester to quantify the initial elastic modulus and stress relaxation behavior of the alginate hydrogels. Alginate disks of 2 mm thickness and 4 mm diameter were prepared and equilibrated in DMEM/F-12 for 24 hr. Unconfined compression tests were then performed on alginate disks using a 4 mm diameter cylindrical probe. Gels were compressed from 0 to 10% compressive strain at a deformation rate of 1 mm per min. 10% compressive strain was then maintained for 1 hr and the corresponding stress was measured over time (stress relaxation test). To calculate the initial elastic modulus, a

straight line was fitted to stress vs. strain data for the initial strain ramp between 5% and 10% compressive strain. The slope of this linear fit was reported as the initial elastic modulus. Next, to quantify the stress relaxation behavior at 10% compressive strain, the time at which relaxation modulus drops to half of its initial value was measured and reported as $\tau_{1/2}$. Final relaxed modulus during the stress relaxation test (~1 kPa) was taken as the effective hydrogel stiffness for cellular processes (including lumen growth) that were much slower than the hydrogel stress relaxation half-time (~70 s).

Encapsulation of cells within hydrogels

To make hydrogels, appropriate volumes of 3% (w/v) alginate and dissociated single hiPSCs were added to a luer lock syringe (Cole-Parmer). In a second syringe, appropriate volumes of calcium sulfate and serum-free DMEM/F-12 were added. The two syringes were connected with a coupler and the solutions were mixed by passing them back and forth six times. The mixture of cell, alginate and calcium sulfate solution were either directly deposited into an 8-well Lab-Tek chamber slide (Thermo Fisher Scientific) or onto a hydrophobic glass plate which was then covered with another glass plate with a 1 mm spacer between plates. The cell alginate mixture was then allowed to gel for 30 mins at room temperature. Hydrogels had a final alginate density of 2% (w/v), cell concentration of 1 million per mL of hydrogel and calcium concentration of 33 mM. Hydrogels were punched out using a 6 mm diameter biopsy punch, immersed in mTeSR1 media with 10 μM ROCK inhibitor (Y-27632, STEMCELL Technologies) to prevent dissociation-induced apoptosis and transferred to an incubator at 37°C and 5% CO_2. 24 hr post encapsulation, media was changed to mTeSR1, which was replenished daily.

Sample preparation for immunofluorescence

hiPSCs cultured in hydrogels were fixed with 4% paraformaldehyde (PFA, Alfa Aesar) for 1 hr, and then washed three times with DPBS containing Ca^{2+} and Mg^{2+} (cPBS, Cytiva). For immunostaining of whole hiPSC epiblasts, these hydrogels were immersed in cPBS and stored at 4°C until used. For immunostaining two-dimensional sections of hydrogels, gels were placed in 30% (w/v) sucrose (Fisher Scientific) overnight and then transferred to 50% (v/v) of 30% (w/v)

sucrose and OCT compound solution (Tissue-Tek) for 5 hr. The hydrogel was then embedded in OCT, frozen, and sectioned at 40 μm thickness using a cryostat (Leica CM1950).

Immunofluorescence of two-dimensional sections and whole hiPSC epiblasts

For two-dimensional sections, samples were washed three times in DPBS (Fisher Scientific), permeabilized with 0.5% Triton X-100 (Sigma-Aldrich) in DPBS for 15 mins and blocked for 1 hr with 1% bovine serum albumin (BSA, Sigma-Aldrich), 10% goat serum (Gibco), 0.3 M glycine (Fisher Scientific), and 0.1% Triton X-100 in DPBS. The samples were incubated overnight with primary antibodies. After washing three times with 0.1% Triton X-100 in DPBS, DAPI (1:1000 dilution; 5 mg/ml stock solution, Thermo Fisher Scientific) and Alexa Fluor 488 Phalloidin (1:80 dilution; Invitrogen A12379) or Alexa Fluor 555 Phalloidin (1:200 dilution; Invitrogen A34055) were incubated for 1.5 hr to stain the nucleus and F-actin along with appropriate secondary antibodies, such as goat anti-Rabbit IgG AF647 (Invitrogen, 1:200 dilution) and goat anti-mouse IgG1 AF555 (Invitrogen, 1:200 dilution). Following three washes with 0.1% Triton X-100 in DPBS, ProLong Gold antifade reagent (Life Technologies) was applied to minimize photobleaching. Images were acquired on a Leica SP8 laser scanning confocal microscope using a HC PL APO 63×/1.4 NA oil immersion objective. Primary antibodies used in study were Oct4 (Cell Signaling Technology #2750), Sox2 (Cell Signaling Technology #3579), Nanog (Cell Signaling Technology #4903), Otx2 (R&D systems AF1979), Ezrin (Sigma-Aldrich E8897), Podocalyxin (R&D systems MAB1658), ZO-1 (Thermo Fisher Scientific 33-9100), phospho-myosin light chain 2 (Cell Signaling Technology #3674), Arp2/3 complex (Sigma-Aldrich MABT95), N-WASP (Thermo Fisher Scientific PA5-52198); all used at 1:200 dilution.

For immunostaining of whole hiPSC epiblasts, PFA-fixed hiPSC epiblasts were first recovered from alginate hydrogels by incubating the hydrogel for 5 mins at room temperature in 50 mM EDTA (ethylenediaminetetraacetic acid) solution. EDTA chelates calcium ions and dissolves the alginate hydrogel, following which mild centrifugation was performed to collect the hiPSC epiblasts. Next, for immunostaining, the same protocol as above was followed with slight modifications: (i) all steps were performed in ultra-low attachment 24-well plates (Corning), (ii) longer incubation – 1 hr permeabilization, 3 hr blocking and overnight secondary antibody steps.

Images were acquired on a Leica SP8 laser scanning confocal microscope using a HC FLUOTAR L 25×/0.95 NA water immersion objective.

SYTOX and Caspase-3/7 staining

hiPSCs in alginate hydrogels were incubated with SYTOX Green Nucleic Acid Stain (1 μM; Invitrogen, Thermo Fisher Scientific S7020) for 1 hr at 37°C and imaged on a Leica SP8 laser scanning confocal microscope with a HC FLUOTAR L 25×/0.95 NA water immersion objective.

For Caspase-3/7 staining, hiPSCs in alginate hydrogels without (control) or with a pan caspase inhibitor (20 μM Z-VAD-FMK; added from Day 1 of culture onwards) were incubated with CellEvent Caspase-3/7 reagent (2 μM; Invitrogen, Thermo Fisher Scientific C10432) for 30 min at 37°C and imaged on a Nikon Ti2 spinning disk confocal microscope with a CFI Plan Fluor DLL 10×/0.3 NA air objective or a CFI Apo LWD Lambda S 40×/1.15 NA water immersion objective.

Tight junction permeability studies

Cell impermeable fluorescent dextran was used to assess tight junction permeability in hiPSC epiblasts. Dextrans with the following molecular weights were used: 3 kDa (Thermo Fisher Scientific D3328), 10 kDa (Thermo Fisher Scientific D1828), 40 kDa (Thermo Fisher Scientific D1829) and 70 kDa (Thermo Fisher Scientific D1830). All these dextrans are conjugated with Texas Red fluorophore and are zwitterionic. For permeability assay, dextran dissolved in mTeSR1 at a final concentration of 10 μM was added to the hydrogel and incubated at 37°C for 1 hr. hiPSC epiblasts were then imaged using Leica SP8 laser scanning confocal microscope with a HC FLUOTAR L 25×/0.95 NA water immersion objective.

To quantify tight junction permeability, outlines were drawn manually around the lumen boundary, inside a cell and in the hydrogel using both the fluorescent dextran and brightfield images to measure dextran intensity in the lumen, cell, and hydrogel using ImageJ (NIH). Cell dextran intensity normalized to that in the hydrogel was consistently ~0.1 confirming that dextrans were cell impermeable. Lumenal dextran intensity was then normalized to that in the hydrogel, called normalized lumenal dextran intensity (NLDI), as a measure of tight junction permeability.

Lumen size and shape metrics were measured in ImageJ. Lumen radius was determined from measured lumen area assuming a perfect circle.

$$Lumen\ radius = \sqrt{\frac{Measured\ lumen\ area}{\pi}} \quad [1]$$

Fluorescence recovery after photobleaching (FRAP) studies

For quantifying diffusion dynamics in smaller epiblasts which lacked tight junctions, fluorescence recovery of dextran was observed after photobleaching on a Zeiss LSM 780 laser scanning confocal microscope using a LCI PLAN NEO 25×/0.8 NA oil immersion objective at 37°C and 5% CO_2. hiPSCs were incubated with 3 kDa dextran for 1 hr before imaging as described in the previous section. For photobleaching, lumen boundary was manually outlined and excited with a micro-point laser at 594 nm (as excitation peak of Texas Red-labelled-dextran is 595 nm) to bleach lumenal dextran using 100 scan iterations of 100% laser power (max power: 0.194 mW). Images were taken before and after bleaching, at 1 min intervals.

Recovery profiles obtained after photobleaching were measured as NLDI (see previous section) and normalized such that initial NLDI was 1 and post-bleach NLDI was 0. The data was then fit to a previously described experimental recovery curve which assumes bleaching of a 2D circular spot followed by free diffusion of non-bleached molecules into the bleached spot from all directions[56]:

$$F(t) = ke^{-\left(\frac{\tau_D}{2t}\right)}\left[I_0\left(\frac{\tau_D}{2t}\right) + I_1\left(\frac{\tau_D}{2t}\right)\right] \quad [2]$$

where I_0 and I_1 are modified Bessel functions of the first kind of zero and first order, k is the mobile fraction and τ_D is the characteristic diffusion time. $\tau_{1/2}$ (diffusion half-time) was calculated as the time at which fluorescence recovers to half the final equilibrated value. While this model accurately fit the experimental data ($R^2 > 0.99$), the assumptions of this model are not completely valid for lumenal bleaching as dextran can diffuse into the lumen only via intercellular spaces and not along all radial directions. Thus, the diffusion coefficient obtained from τ_D cannot be directly compared to diffusion coefficients predicted by the Stokes-Einstein equation.

Inhibition studies

For all small-molecule inhibition studies, the drug was added 24 hr before imaging or continuously starting on day 2 of culture (for plots labelled continuous inhibition). The inhibitors used were Blebbistatin (10 μM; Abcam ab120425, myosin II inhibitor), ML-7 (10 μM; Tocris Bioscience 4310, myosin light chain kinase inhibitor), ML-141 (2 μM; Tocris Bioscience 4266, selective Cdc42 Rho family inhibitor), Y-27632 (10 μM; STEMCELL 72304, ROCK inhibitor), CK-666 (50-100 μM; Sigma-Aldrich SML0006, Arp2/3 inhibitor), SMIFH2 (10-20 μM; Sigma-Aldrich S4826, formin inhibitor) and Wiskostatin (5-10 μM; Abcam ab141085, N-WASP inhibitor). All drugs were dissolved in dimethyl sulfoxide (DMSO) and diluted in mTeSR1 media before adding to hiPSCs. DMSO alone was added to mTeSR1 media as a vehicle control. Percent clusters with lumen was manually quantified from brightfield images using ImageJ.

SiR-actin staining and live cell imaging

For live imaging of F-actin in hiPSC epiblasts, SiR-actin (100 nM; Cytoskeleton Inc. CY-SC001) was added to hiPSCs in hydrogels for 12 hr following manufacturer's protocol. SiR-actin did not impact F-actin or hiPSC epiblast morphogenesis (Figure S7) and has been previously shown to not alter F-actin dynamics at a concentration of 100 nM or lower[63]. For timelapse imaging of F-actin, mTeSR1 media was supplemented with 100 nM SiR-actin (to maintain strong F-actin fluorescence) and 2.5 mM *N*-acetyl-L-cysteine (NAC, Sigma-Aldrich A9165; antioxidant to reduce phototoxicity). Fluorescent F-actin (excitation peak of SiR-actin is 652 nm) and brightfield images were acquired every 15 min for a total duration of 8 hr on a Leica SP8 laser scanning confocal microscope with a HC FLUOTAR L 25×/0.95 NA water immersion objective at 37°C and 5% CO_2.

For quantifying timelapse data, lumen areas and apical lengths of individual cells were manually measured using ImageJ. To understand the correlation between lumen growth and increase in cell apical actin lengths for a fixed number of cells, 4 hr time windows were picked from acquired data, during which there was no change in cell number in both smaller and larger epiblasts. Correlation between lumen area and individual cell apical lengths was quantified by calculating Spearman correlation values between each pair of curves in GraphPad Prism (9.3.1). Percent cell apical lengths positively correlated with lumen area was calculated by counting

number of cells whose correlation with lumen area has a Spearman value >0.5 and dividing by total number of cells in a given epiblast. 3D timelapse imaging of hiPSC epiblasts with high z-resolution was not possible due to phototoxicity effects upon increased laser exposure.

Super-resolution microscopy

Super-resolution microscopy was performed to visualize apical actin mesh in SiR-actin stained hiPSC epiblasts, using a Zeiss Airyscan2 LSM 980 inverted confocal microscope with a LCI PLAN NEO 25×/0.8 NA oil immersion objective at 37°C and 5% CO_2. Images were acquired in super-resolution mode with a voxel size of 0.0974 × 0.0974 × 0.81 μm^3 (x y z) and processed using 15 iterations of a 3D iterative joint deconvolution (jDCV) algorithm (Zeiss).

Laser ablation studies

Laser ablation was performed to determine the stress state of actin in SiR-actin stained hiPSC epiblasts, using a Zeiss LSM 780 laser scanning confocal microscope with a LCI PLAN NEO 25×/0.8 NA oil immersion objective at 37°C and 5% CO_2. A micro-point laser at 405 nm was used to ablate apical actin or to cut through the entire thickness of a cell in both smaller and larger epiblasts using 150 scan iterations of 100% laser power (max power: 1.85 mW). Images were taken before and after ablation, at 1 min intervals.

To measure recoil or retraction of apical actin in hiPSC epiblasts, apical lengths and apical actin intensity of ablated cell and its neighboring cells as well as lumen area were manually measured using ImageJ at each time-point: pre-ablation, immediately post-ablation and at 1 min intervals post-ablation up to 13 min. Apical lengths and apical actin intensities of ablated and neighboring cells at different timepoints were stitched together to generate kymographs of the combined apical surface of the three cells (1 ablated + 2 neighbors).

Note that laser ablation did not disrupt the integrity of the cell membrane. No indication of a punctured membrane or leakage of cytoplasmic material was observed in brightfield images during laser ablation experiments for both smaller and larger epiblasts. Ablated cells stayed alive for longer than 2 hr post-ablation and maintained their nuclear and cellular size during this period

(Figures S7E and S7F). In some larger epiblasts, laser ablation resulted in drastic lumen collapse, further highlighting that lumens in larger epiblasts are pressurized (Video S5).

Hydrogel dissolution and cell lysis

Alginate hydrogels were dissolved by adding 50 mM EDTA (ethylenediaminetetraacetic acid) solution. Images were captured continuously on a Nikon Ti2 spinning disk confocal microscope with a CFI Plan Fluor DLL 10×/0.3 NA air objective.

Cell lysis was performed by adding a lysing solution composed of 1% Triton X-100 and 50 μM Cytochalasin D to hiPSC epiblasts. Images were captured continuously on a Nikon Ti2 spinning disk confocal microscope with a CFI Plan Fluor DLL 10×/0.3 NA air objective.

Theoretical model and computational simulations

Description of the main hypotheses and equations of the physical models and the methods underlying the numerical simulations are provided in supplementary information.

QUANTIFICATION AND STATISTICAL ANALYSIS

Quantification of hydrogel deformations

For quantifying hydrogel deformations, 1 μm diameter fluorescent carboxylate-modified microspheres (FluoSpheres, Thermo Fisher Scientific F8816) were encapsulated in alginate hydrogels. Timelapse images of fluorescent beads were collected during lumen growth in both smaller and larger epiblasts on a Leica SP8 laser scanning confocal microscope with a HC FLUOTAR L 25×/0.95 NA water immersion objective at 37°C and 5% CO_2. Acquired images were corrected for drift using an ImageJ plugin (StackReg). Next, the drift-corrected images were used to calculate matrix deformations in MATLAB by tracking beads using a particle image velocimetry algorithm (PIVlab; open source code) using three cross-correlation windows (128 × 128, 64 × 64, and 32 × 32 pixel interrogation windows). Maximum matrix deformation was selected from within ~100 μm^2 around the cells. Radial asymmetry of matrix deformations (asymmetry index) was quantified by taking the ratio of magnitude of vector sum of deformations

to average magnitude of deformations. Finally, note that the direct estimation of forces from matrix deformations is challenging due to hydrogel viscoelasticity and plasticity. Thus, in this study, matrix deformations were used as a proxy for force generation, as matrix deformation only occurred as a result of cellular forces in these gels.

Two-dimensional image analysis

Lumen solidity: hiPSC epiblasts were first incubated with fluorescent dextran (see previous section on tight junction permeability studies) to visualize smaller lumens. Outlines of lumen were manually drawn in ImageJ using fluorescent dextran or brightfield images. Lumen size and shape metrics including lumen solidity were measured in ImageJ. Lumen radius was determined from measured lumen area assuming a perfect circle (see equation [1]).

Nuclear area and perimeter: Nuclear area and perimeter of hiPSC and human epiblasts as well as hiPSCs in 2D culture, were respectively measured from immunostained images acquired in-house and from previously published sources[24,31,32,55,64-66]. Using ImageJ, nuclear images were thresholded, smoothened using median filter (radius of 4 pixels), and processed using a Watershed algorithm (ImageJ) to separate touching nuclei. Nuclear area and perimeter were then measured in ImageJ.

Cell thickness of hiPSC epiblasts: For quantifying average thickness of cell layer in smaller and larger epiblasts, 5 lines were manually drawn per cluster from the apical to the basal surface and their corresponding lengths were measured from immunostained images of whole hiPSC epiblasts in ImageJ. These 5 lengths were averaged and reported as the average cell thickness.

Demarcation of lumen boundary: For validating use of F-actin, dextran and brightfield images for demarcating lumen boundary, lumen outlines were drawn using fluorescent images of podocalyxin (PODXL-EGFP hPSC line), F-actin (SiR-actin), dextran and brightfield images and compared (Figure S2A to S2C). As expected, dextran entered lumens in smaller epiblasts but not in larger epiblasts (Figure S2A). As dextran occupies the enter lumenal volume in smaller epiblasts, we considered dextran as the most reliable marker of lumenal surface. All lumen outlines were comparable with only minor differences, suggesting that podocalyxin, F-actin, dextran and brightfield images can all be used to reliably demarcate the lumenal surface (Figure S2B). Lumen

area measured using dextran, F-actin and brightfield were all similar without any statistically significant differences (Figure S2B). However, lumen area measured using podocalyxin was slightly smaller, possibly because podocalyxin, a transmembrane protein, extends into the lumenal volume (Figure S2B).

Three-dimensional image analysis

Lumen volume, number of cells, apical surface area and cell volume quantification: High resolution z-stacks of nucleus and F-actin in immunostained whole hiPSC epiblasts were acquired (see previous section on immunofluorescence of whole hiPSC epiblasts) using a Leica SP8 laser scanning confocal microscope with a HC FLUOTAR L 25×/0.95 NA water immersion objective. Images were acquired with a voxel size of 0.0909 × 0.0909 × 0.5691 μm^3 (x y z). Lumen volume, number of cells, apical surface area of individual cells and individual cell volumes of hiPSC epiblasts were quantified from these high-resolution z-stacks using Imaris 9.9 software (Bitplane). Nuclear images were used to quantify number of cells with Surfaces program in Imaris. F-actin images were used to quantify lumen volume and apical surface area of individual cells with Surfaces program in Imaris. Nucleus and F-actin images were both used to segment individual cells and quantify cell volumes with Cells program in Imaris. Lumen radius was determined from measured lumen volume assuming lumen to be a perfect sphere.

$$Lumen\ radius = \sqrt[3]{\frac{3\ .\ (Measured\ lumen\ volume)}{4\pi}} \quad [3]$$

Lumen curvature quantification: To quantify lumen surface curvature in smaller and larger epiblasts, lumen surfaces reconstructed in Imaris from high-resolution z-stacks of immunostained whole hiPSC epiblasts were exported to ImageJ. LimeSeg plugin in ImageJ was then used to compute gaussian curvature at each point of lumen surface.

Morphological comparison of human and hiPSC epiblasts

To compare morphological features of human and hiPSC epiblasts, number of cells and lumen volumes of hiPSC epiblasts on different days of culture were compared to those of human

epiblasts. Average number of cells in human epiblasts on different days post fertilization were previously reported[32]. To quantify the evolution of lumen volumes as a function of number of cells in human epiblasts (Figure 1E), previously published data and images were used. Lumen volumes were estimated from previously reported radius of gyration values of human epiblasts[24], assuming human epiblasts to be a perfect sphere and individual cell volume to be ~1500 μm^3 (which was the average cell volume in hiPSC epiblasts). For these human epiblasts, number of cells were reported[24]. Next, to obtain additional data points from human epiblasts, we analyzed published 2D immunostained images of human epiblasts[20,24,31,32,55] and measured lumen area and total cell area in the mid-plane of human epiblasts. This 2D lumen area and total cell area in mid-plane were used to estimate 3D lumen volume and number of cells in the human epiblast using the following assumptions: (i) human epiblast tissue and lumen are perfectly spherical, (ii) each cell in human epiblast has a cell volume of ~1500 μm^3 (which was the average cell volume in hiPSC epiblasts). A key limitation of this comparison is that human embryo images are only available from in vitro cultured human embryos where embryos are attached to 2D tissue culture plates, resulting in somewhat altered lumen and cell morphology.

Analysis of single cell RNA sequencing data

Human embryo derived single cell RNA sequencing datasets[42,43] were analyzed using Seurat R package (v4.2.0). Unprocessed datasets were obtained from publicly available GEO repositories: GSE136447[42] and GSE109555[43]. Datasets were filtered to only include epiblast cells based on previously annotated populations in respective studies. Default setups in Seurat were used unless noted otherwise. Cells with ≤4,500 genes detected were discarded from analysis. Gene expression was calculated by normalizing raw counts by the total count, multiplying by 10,000 and performing log-transformation. Then, principal component analysis was performed in Seurat. Cell clusters were identified by a K-nearest neighbor (KNN) clustering approach with a resolution of 0.8. Non-linear dimensionality reduction was performed using Uniform Manifold Approximation and Projection (UMAP) algorithm (dimensions 1 to 10). UMAP showed that cell clusters obtained by KNN based clustering were roughly separated based on embryo age (days post fertilization) and were annotated accordingly. Finally, average expression level of different genes of interest were plotted for each cell cluster.

Statistical analysis

Statistical analyses were performed using GraphPad Prism 9.3.1 software. List of all statistical tests used, and corresponding exact number of samples (*n* values) and exact *P* values are provided in Table S1. All Mann-Whitney tests used were two-tailed tests. Bar plots and respective error bars are defined throughout the figures. For ANOVA tests, F values and degrees of freedom (DFn: degrees of freedom between groups; DFd: degrees of freedom within groups) are provided in Table S1. *P* values less than 0.05 were considered statistically significant. All tests used were two-tailed unless mentioned otherwise.

In Figure 1, hiPSC epiblast immunostaining images (Figures 1B and 1C) are representative of 3 independent biological replicates. In Figure 2, images (Figures 2C, 2F, 2G, 2H and 2K) are representative of 3 independent biological replicates. In Figure 3, images (Figure 3J) are representative of ≥3 independent biological replicates. In Figure S1, hiPSC epiblast immunostaining images (Figures S1B, S1C, S1F and S1G) are representative of ≥2 independent biological replicates. In Figure S2, hiPSC epiblast immunostaining images (Figure S2K) are representative of 3 independent biological replicates. In Figure S3, hiPSC epiblast immunostaining images (Figure S3A) are representative of 3 independent biological replicates. For all experimental plots, data are pooled from ≥3 biological replicates unless mentioned otherwise in the figure captions. *N* (biological replicates) values for all plots are listed in Table S1.

Video S1 [supporting Fig. 1]. Fluorescence recovery after photobleaching (FRAP) of lumenal dextran. Red arrowhead indicates bleached lumenal dextran.

Video S2 [supporting Fig. 2]. Brightfield timelapse imaging of lumen expansion in a smaller (top row) and a larger (bottom row) epiblast. Red arrowhead indicates lumen.

Video S3 [supporting Figs. 3 and 5]. F-actin and brightfield timelapse imaging of lumen growth in a smaller (top row) and a larger (bottom row) epiblast.

Video S4 [supporting Figs. 3 and 5]. Apical F-actin ablation and recovery in a smaller (top row) and a larger (bottom row) epiblast. Dotted red box indicates ablated apical surface. Red arrowhead follows the ablated cell during the timelapse. Cyan arrowhead indicates the absence of blebbing post-ablation.

Video S5 [supporting Fig. 5]. Examples of apical junction ablation in larger epiblasts resulting in lumen collapse. Dotted red box indicates ablated apical surface. Red arrowhead follows the ablated cell during the timelapse.

Table S1 [supporting Figs. 1, 2, 3, 5 and 6]. List of statistical tests used and corresponding *n* (sample size), *N* (biological replicates) and *P* values for all plots.

Methods S1 [supporting Figs. 4 and 5]: Procedures for computational modeling

References

1. Rossant, J., and Tam, P.P.L. (2017). New Insights into Early Human Development: Lessons for Stem Cell Derivation and Differentiation. Cell Stem Cell *20*, 18-28. https://doi.org/10.1016/j.stem.2016.12.004.

2. Shahbazi, M.N., and Zernicka-Goetz, M. (2018). Deconstructing and reconstructing the mouse and human early embryo. Nature Cell Biology *20*, 878-887. 10.1038/s41556-018-0144-x.

3. Martindale, M.Q. (2005). The evolution of metazoan axial properties. Nature Reviews Genetics *6*, 917-927. 10.1038/nrg1725.

4. Zhang, Z., Zwick, S., Loew, E., Grimley, J.S., and Ramanathan, S. (2019). Mouse embryo geometry drives formation of robust signaling gradients through receptor localization. Nature Communications *10*, 4516. 10.1038/s41467-019-12533-7.

5. Girgin, M.U., Broguiere, N., Hoehnel, S., Brandenberg, N., Mercier, B., Arias, A.M., and Lutolf, M.P. (2021). Bioengineered embryoids mimic post-implantation development in vitro. Nature Communications *12*, 5140. 10.1038/s41467-021-25237-8.

6. Blasky, A.J., Mangan, A., and Prekeris, R. (2015). Polarized Protein Transport and Lumen Formation During Epithelial Tissue Morphogenesis. Annual Review of Cell and Developmental Biology *31*, 575-591. 10.1146/annurev-cellbio-100814-125323.

7. Sigurbjörnsdóttir, S., Mathew, R., and Leptin, M. (2014). Molecular mechanisms of de novo lumen formation. Nature Reviews Molecular Cell Biology *15*, 665-676. 10.1038/nrm3871.

8. Debnath, J., Mills, K.R., Collins, N.L., Reginato, M.J., Muthuswamy, S.K., and Brugge, J.S. (2002). The Role of Apoptosis in Creating and Maintaining Luminal Space within Normal and Oncogene-Expressing Mammary Acini. Cell *111*, 29-40. https://doi.org/10.1016/S0092-8674(02)01001-2.

9. Ruiz-Herrero, T., Alessandri, K., Gurchenkov, B.V., Nassoy, P., and Mahadevan, L. (2017). Organ size control via hydraulically gated oscillations. Development *144*, 4422-4427. 10.1242/dev.153056.

10. Chan, C.J., Costanzo, M., Ruiz-Herrero, T., Mönke, G., Petrie, R.J., Bergert, M., Diz-Muñoz, A., Mahadevan, L., and Hiiragi, T. (2019). Hydraulic control of mammalian embryo size and cell fate. Nature *571*, 112-116. 10.1038/s41586-019-1309-x.

11. Dumortier, J.G., Le Verge-Serandour, M., Tortorelli, A.F., Mielke, A., de Plater, L., Turlier, H., and Maître, J.-L. (2019). Hydraulic fracturing and active coarsening position the lumen of the mouse blastocyst. Science *365*, 465-468. 10.1126/science.aaw7709.

12. Latorre, E., Kale, S., Casares, L., Gómez-González, M., Uroz, M., Valon, L., Nair, R.V., Garreta, E., Montserrat, N., del Campo, A., et al. (2018). Active superelasticity in three-

dimensional epithelia of controlled shape. Nature *563*, 203-208. 10.1038/s41586-018-0671-4.

13. Dasgupta, S., Gupta, K., Zhang, Y., Viasnoff, V., and Prost, J. (2018). Physics of lumen growth. Proceedings of the National Academy of Sciences *115*, E4751-E4757. doi:10.1073/pnas.1722154115.

14. Mosaliganti, K.R., Swinburne, I.A., Chan, C.U., Obholzer, N.D., Green, A.A., Tanksale, S., Mahadevan, L., and Megason, S.G. (2019). Size control of the inner ear via hydraulic feedback. eLife *8*, e39596. 10.7554/eLife.39596.

15. Torres-Sánchez, A., Kerr Winter, M., and Salbreux, G. (2021). Tissue hydraulics: Physics of lumen formation and interaction. Cells & Development, 203724. https://doi.org/10.1016/j.cdev.2021.203724.

16. Chugh, M., Munjal, A., and Megason, S.G. (2022). Hydrostatic pressure as a driver of cell and tissue morphogenesis. Seminars in Cell & Developmental Biology. https://doi.org/10.1016/j.semcdb.2022.04.021.

17. Kim, Y.S., and Bedzhov, I. (2022). Mechanisms of formation and functions of the early embryonic cavities. Seminars in Cell & Developmental Biology. https://doi.org/10.1016/j.semcdb.2022.04.020.

18. Carleton, A.E., Duncan, M.C., and Taniguchi, K. (2022). Human epiblast lumenogenesis: From a cell aggregate to a lumenal cyst. Seminars in Cell & Developmental Biology. https://doi.org/10.1016/j.semcdb.2022.05.009.

19. Wang, S., Lin, C.-W., Carleton, A.E., Cortez, C.L., Johnson, C., Taniguchi, L.E., Sekulovski, N., Townshend, R.F., Basrur, V., Nesvizhskii, A.I., et al. (2021). Spatially resolved cell polarity proteomics of a human epiblast model. Science Advances *7*, eabd8407. doi:10.1126/sciadv.abd8407.

20. Shahbazi, M.N., Scialdone, A., Skorupska, N., Weberling, A., Recher, G., Zhu, M., Jedrusik, A., Devito, L.G., Noli, L., Macaulay, I.C., et al. (2017). Pluripotent state transitions coordinate morphogenesis in mouse and human embryos. Nature *552*, 239-243. 10.1038/nature24675.

21. Fu, J., Warmflash, A., and Lutolf, M.P. (2021). Stem-cell-based embryo models for fundamental research and translation. Nature Materials *20*, 132-144. 10.1038/s41563-020-00829-9.

22. Bao, M., Cornwall-Scoones, J., and Zernicka-Goetz, M. (2022). Stem-cell-based human and mouse embryo models. Current Opinion in Genetics & Development *76*, 101970. https://doi.org/10.1016/j.gde.2022.101970.

23. Zheng, Y., Xue, X., Shao, Y., Wang, S., Esfahani, S.N., Li, Z., Muncie, J.M., Lakins, J.N., Weaver, V.M., Gumucio, D.L., and Fu, J. (2019). Controlled modelling of human epiblast

and amnion development using stem cells. Nature *573*, 421-425. 10.1038/s41586-019-1535-2.

24. Simunovic, M., Metzger, J.J., Etoc, F., Yoney, A., Ruzo, A., Martyn, I., Croft, G., You, D.S., Brivanlou, A.H., and Siggia, E.D. (2019). A 3D model of a human epiblast reveals BMP4-driven symmetry breaking. Nature Cell Biology *21*, 900-910. 10.1038/s41556-019-0349-7.

25. Taniguchi, K., Shao, Y., Townshend, Ryan F., Tsai, Y.-H., DeLong, Cynthia J., Lopez, Shawn A., Gayen, S., Freddo, Andrew M., Chue, Deming J., Thomas, Dennis J., et al. (2015). Lumen Formation Is an Intrinsic Property of Isolated Human Pluripotent Stem Cells. Stem Cell Reports *5*, 954-962. https://doi.org/10.1016/j.stemcr.2015.10.015.

26. Schindler, M., Siriwardena, D., Kohler, T.N., Ellermann, A.L., Slatery, E., Munger, C., Hollfelder, F., and Boroviak, T.E. (2021). Agarose microgel culture delineates lumenogenesis in naive and primed human pluripotent stem cells. Stem Cell Reports *16*, 1347-1362. 10.1016/j.stemcr.2021.04.009.

27. Indana, D., Agarwal, P., Bhutani, N., and Chaudhuri, O. (2021). Viscoelasticity and Adhesion Signaling in Biomaterials Control Human Pluripotent Stem Cell Morphogenesis in 3D Culture. Advanced Materials *33*, 2101966. https://doi.org/10.1002/adma.202101966.

28. Pera, M.F., and Rossant, J. (2021). The exploration of pluripotency space: Charting cell state transitions in peri-implantation development. Cell Stem Cell *28*, 1896-1906. 10.1016/j.stem.2021.10.001.

29. Molè, M.A., Weberling, A., Fässler, R., Campbell, A., Fishel, S., and Zernicka-Goetz, M. (2021). Integrin β1 coordinates survival and morphogenesis of the embryonic lineage upon implantation and pluripotency transition. Cell Rep *34*, 108834. 10.1016/j.celrep.2021.108834.

30. Taniguchi, K., Shao, Y., Townshend, R.F., Cortez, C.L., Harris, C.E., Meshinchi, S., Kalantry, S., Fu, J., O'Shea, K.S., and Gumucio, D.L. (2017). An apicosome initiates self-organizing morphogenesis of human pluripotent stem cells. Journal of Cell Biology *216*, 3981-3990. 10.1083/jcb.201704085.

31. Deglincerti, A., Croft, G.F., Pietila, L.N., Zernicka-Goetz, M., Siggia, E.D., and Brivanlou, A.H. (2016). Self-organization of the in vitro attached human embryo. Nature *533*, 251-254. 10.1038/nature17948.

32. Shahbazi, M.N., Jedrusik, A., Vuoristo, S., Recher, G., Hupalowska, A., Bolton, V., Fogarty, N.M.E., Campbell, A., Devito, L.G., Ilic, D., et al. (2016). Self-organization of the human embryo in the absence of maternal tissues. Nature Cell Biology *18*, 700-708. 10.1038/ncb3347.

33. Kinoshita, M., Barber, M., Mansfield, W., Cui, Y., Spindlow, D., Stirparo, G.G., Dietmann, S., Nichols, J., and Smith, A. (2021). Capture of Mouse and Human Stem Cells with

Features of Formative Pluripotency. Cell Stem Cell *28*, 453-471.e458. https://doi.org/10.1016/j.stem.2020.11.005.

34. Bedzhov, I., and Zernicka-Goetz, M. (2014). Self-Organizing Properties of Mouse Pluripotent Cells Initiate Morphogenesis upon Implantation. Cell *156*, 1032-1044. https://doi.org/10.1016/j.cell.2014.01.023.

35. Shen, L., Weber, C.R., Raleigh, D.R., Yu, D., and Turner, J.R. (2011). Tight Junction Pore and Leak Pathways: A Dynamic Duo. Annual Review of Physiology *73*, 283-309. 10.1146/annurev-physiol-012110-142150.

36. Farquhar , M.G., and Palade , G.E. (1965). CELL JUNCTIONS IN AMPHIBIAN SKIN. Journal of Cell Biology *26*, 263-291. 10.1083/jcb.26.1.263.

37. Otani, T., Nguyen, T.P., Tokuda, S., Sugihara, K., Sugawara, T., Furuse, K., Miura, T., Ebnet, K., and Furuse, M. (2019). Claudins and JAM-A coordinately regulate tight junction formation and epithelial polarity. Journal of Cell Biology *218*, 3372-3396. 10.1083/jcb.201812157.

38. Vasquez, C.G., Vachharajani, V.T., Garzon-Coral, C., and Dunn, A.R. (2021). Physical basis for the determination of lumen shape in a simple epithelium. Nature Communications *12*, 5608. 10.1038/s41467-021-25050-3.

39. Fletcher, D.A., and Mullins, R.D. (2010). Cell mechanics and the cytoskeleton. Nature *463*, 485-492. 10.1038/nature08908.

40. Harris, A.R., Peter, L., Bellis, J., Baum, B., Kabla, A.J., and Charras, G.T. (2012). Characterizing the mechanics of cultured cell monolayers. Proceedings of the National Academy of Sciences *109*, 16449-16454. doi:10.1073/pnas.1213301109.

41. Trushko, A., Di Meglio, I., Merzouki, A., Blanch-Mercader, C., Abuhattum, S., Guck, J., Alessandri, K., Nassoy, P., Kruse, K., Chopard, B., and Roux, A. (2020). Buckling of an Epithelium Growing under Spherical Confinement. Developmental Cell *54*, 655-668.e656. https://doi.org/10.1016/j.devcel.2020.07.019.

42. Xiang, L., Yin, Y., Zheng, Y., Ma, Y., Li, Y., Zhao, Z., Guo, J., Ai, Z., Niu, Y., Duan, K., et al. (2020). A developmental landscape of 3D-cultured human pre-gastrulation embryos. Nature *577*, 537-542. 10.1038/s41586-019-1875-y.

43. Zhou, F., Wang, R., Yuan, P., Ren, Y., Mao, Y., Li, R., Lian, Y., Li, J., Wen, L., Yan, L., et al. (2019). Reconstituting the transcriptome and DNA methylome landscapes of human implantation. Nature *572*, 660-664. 10.1038/s41586-019-1500-0.

44. Kim, Y.S., Fan, R., Kremer, L., Kuempel-Rink, N., Mildner, K., Zeuschner, D., Hekking, L., Stehling, M., and Bedzhov, I. (2021). Deciphering epiblast lumenogenesis reveals proamniotic cavity control of embryo growth and patterning. Science Advances *7*, eabe1640. doi:10.1126/sciadv.abe1640.

45. Gautreau, A.M., Fregoso, F.E., Simanov, G., and Dominguez, R. (2022). Nucleation, stabilization, and disassembly of branched actin networks. Trends in Cell Biology *32*, 421-432. https://doi.org/10.1016/j.tcb.2021.10.006.

46. Schwayer, C., Sikora, M., Slováková, J., Kardos, R., and Heisenberg, C.-P. (2016). Actin Rings of Power. Developmental Cell *37*, 493-506. https://doi.org/10.1016/j.devcel.2016.05.024.

47. Sedzinski, J., Hannezo, E., Tu, F., Biro, M., and Wallingford, J.B. (2017). RhoA regulates actin network dynamics during apical surface emergence in multiciliated epithelial cells. Journal of Cell Science *130*, 420-428. 10.1242/jcs.194704.

48. Del Signore, S.J., Cilla, R., and Hatini, V. (2018). The WAVE Regulatory Complex and Branched F-Actin Counterbalance Contractile Force to Control Cell Shape and Packing in the Drosophila Eye. Developmental Cell *44*, 471-483.e474. 10.1016/j.devcel.2017.12.025.

49. Lim, H.Y.G., and Plachta, N. (2021). Cytoskeletal control of early mammalian development. Nature Reviews Molecular Cell Biology *22*, 548-562. 10.1038/s41580-021-00363-9.

50. Zenker, J., White, M.D., Gasnier, M., Alvarez, Y.D., Lim, H.Y.G., Bissiere, S., Biro, M., and Plachta, N. (2018). Expanding Actin Rings Zipper the Mouse Embryo for Blastocyst Formation. Cell *173*, 776-791.e717. https://doi.org/10.1016/j.cell.2018.02.035.

51. Alvers, A.L., Ryan, S., Scherz, P.J., Huisken, J., and Bagnat, M. (2014). Single continuous lumen formation in the zebrafish gut is mediated by smoothened-dependent tissue remodeling. Development *141*, 1110-1119. 10.1242/dev.100313.

52. Dong, B., Hannezo, E., and Hayashi, S. (2014). Balance between Apical Membrane Growth and Luminal Matrix Resistance Determines Epithelial Tubule Shape. Cell Reports *7*, 941-950. https://doi.org/10.1016/j.celrep.2014.03.066.

53. Ryan, A.Q., Chan, C.J., Graner, F., and Hiiragi, T. (2019). Lumen Expansion Facilitates Epiblast-Primitive Endoderm Fate Specification during Mouse Blastocyst Formation. Developmental Cell *51*, 684-697.e684. https://doi.org/10.1016/j.devcel.2019.10.011.

54. Pfeffer, P.L. (2022). Alternative mammalian strategies leading towards gastrulation: losing polar trophoblast (Rauber's layer) or gaining an epiblast cavity. Philosophical Transactions of the Royal Society B: Biological Sciences *377*, 20210254. doi:10.1098/rstb.2021.0254.

55. Molè, M.A., Coorens, T.H.H., Shahbazi, M.N., Weberling, A., Weatherbee, B.A.T., Gantner, C.W., Sancho-Serra, C., Richardson, L., Drinkwater, A., Syed, N., et al. (2021). A single cell characterisation of human embryogenesis identifies pluripotency transitions and putative anterior hypoblast centre. Nature Communications *12*, 3679. 10.1038/s41467-021-23758-w.

56. Soumpasis, D.M. (1983). Theoretical analysis of fluorescence photobleaching recovery experiments. Biophysical Journal *41*, 95-97. https://doi.org/10.1016/S0006-3495(83)84410-5.

57. Durruthy-Durruthy, J., Briggs, S.F., Awe, J., Ramathal, C.Y., Karumbayaram, S., Lee, P.C., Heidmann, J.D., Clark, A., Karakikes, I., Loh, K.M., et al. (2014). Rapid and Efficient Conversion of Integration-Free Human Induced Pluripotent Stem Cells to GMP-Grade Culture Conditions. PLOS ONE *9*, e94231. 10.1371/journal.pone.0094231.

58. Schindelin, J., Arganda-Carreras, I., Frise, E., Kaynig, V., Longair, M., Pietzsch, T., Preibisch, S., Rueden, C., Saalfeld, S., Schmid, B., et al. (2012). Fiji: an open-source platform for biological-image analysis. Nature Methods *9*, 676-682. 10.1038/nmeth.2019.

59. Thielicke, W., and Sonntag, R. (2021). Particle Image Velocimetry for MATLAB: Accuracy and enhanced algorithms in PIVlab. Journal of Open Research Software *9*, 12. 10.5334/jors.334.

60. Hao, Y., Hao, S., Andersen-Nissen, E., Mauck, W.M., Zheng, S., Butler, A., Lee, M.J., Wilk, A.J., Darby, C., Zager, M., et al. (2021). Integrated analysis of multimodal single-cell data. Cell *184*, 3573-3587.e3529. https://doi.org/10.1016/j.cell.2021.04.048.

61. Rowley, J.A., and Mooney, D.J. (2002). Alginate type and RGD density control myoblast phenotype. Journal of Biomedical Materials Research *60*, 217-223. https://doi.org/10.1002/jbm.1287.

62. Charbonier, F., Indana, D., and Chaudhuri, O. (2021). Tuning Viscoelasticity in Alginate Hydrogels for 3D Cell Culture Studies. Current Protocols *1*, e124. https://doi.org/10.1002/cpz1.124.

63. Lukinavičius, G., Reymond, L., D'Este, E., Masharina, A., Göttfert, F., Ta, H., Güther, A., Fournier, M., Rizzo, S., Waldmann, H., et al. (2014). Fluorogenic probes for live-cell imaging of the cytoskeleton. Nature Methods *11*, 731-733. 10.1038/nmeth.2972.

64. Rodin, S., Domogatskaya, A., Ström, S., Hansson, E.M., Chien, K.R., Inzunza, J., Hovatta, O., and Tryggvason, K. (2010). Long-term self-renewal of human pluripotent stem cells on human recombinant laminin-511. Nature Biotechnology *28*, 611-615. 10.1038/nbt.1620.

65. Zhang, X., Simerly, C., Hartnett, C., Schatten, G., and Smithgall, T.E. (2014). Src-family tyrosine kinase activities are essential for differentiation of human embryonic stem cells. Stem Cell Research *13*, 379-389. https://doi.org/10.1016/j.scr.2014.09.007.

66. Nakagawa, M., Taniguchi, Y., Senda, S., Takizawa, N., Ichisaka, T., Asano, K., Morizane, A., Doi, D., Takahashi, J., Nishizawa, M., et al. (2014). A novel efficient feeder-free culture system for the derivation of human induced pluripotent stem cells. Scientific Reports *4*, 3594. 10.1038/srep03594.

Figure

hiPSC epiblast model recapitulates human epiblast phenotype and morphology

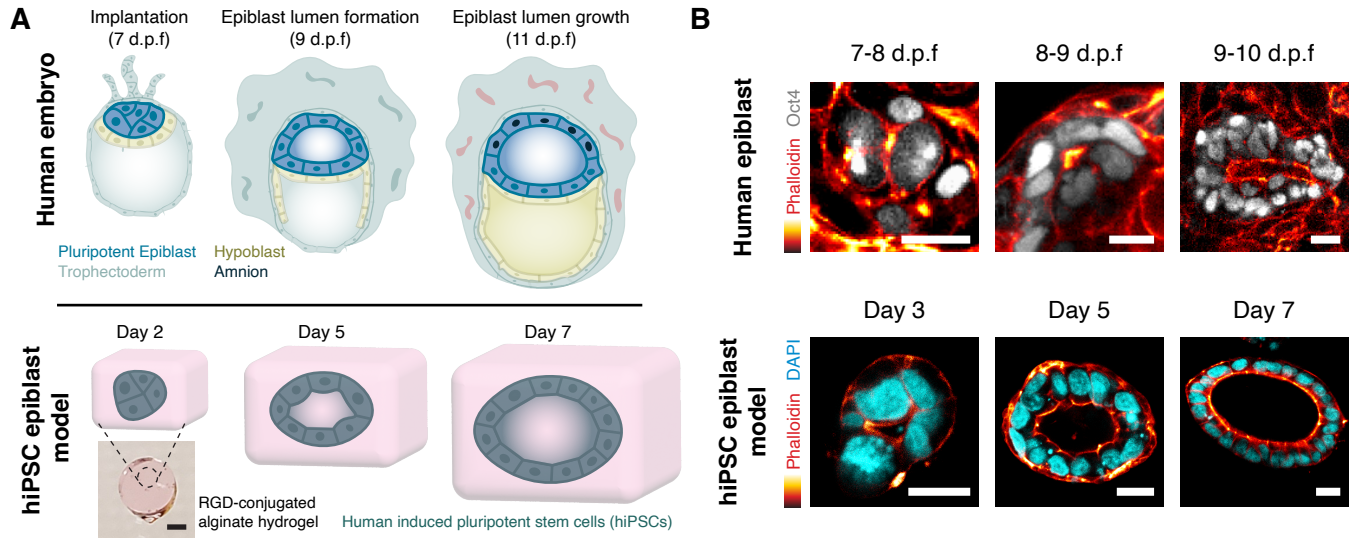

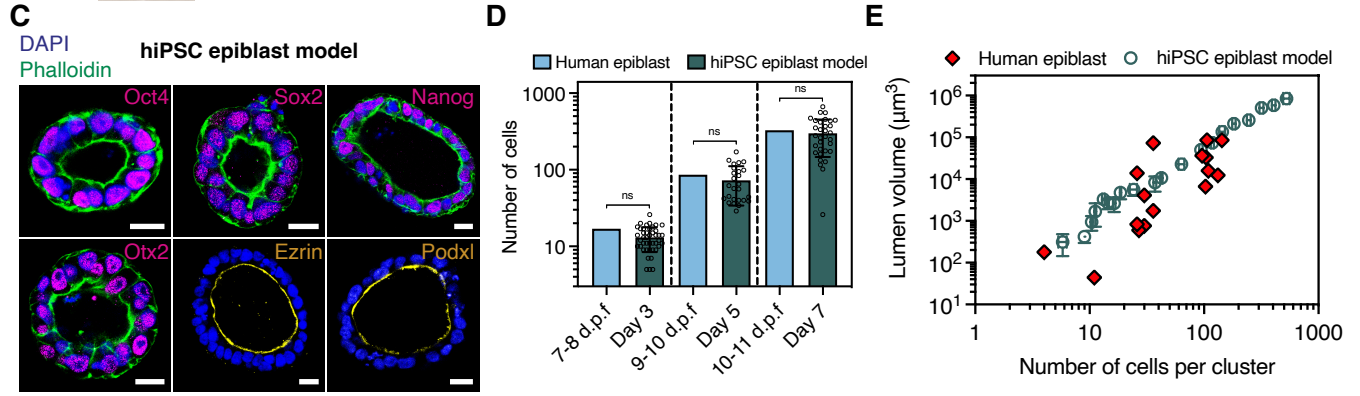

Osmotic pressure does not drive lumen growth in lumens smaller than 12 μm radius

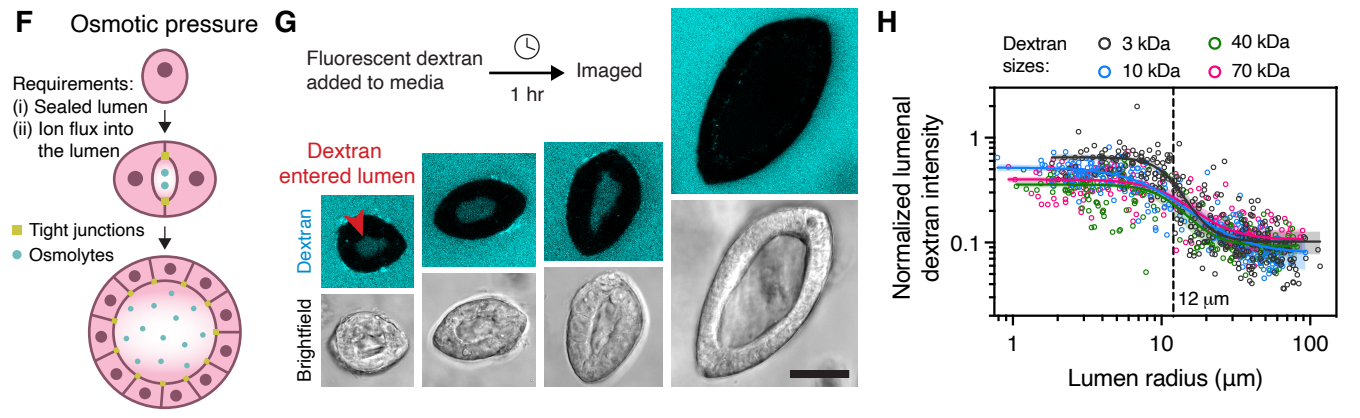

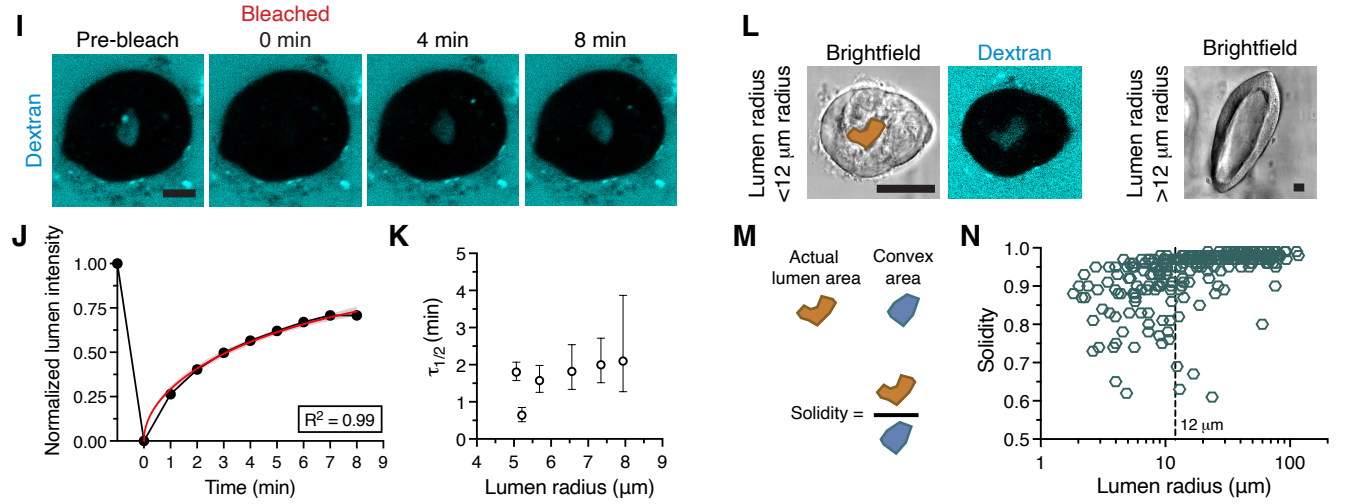

Figure

Lumen opening and growth in hiPSC epiblasts require force generation

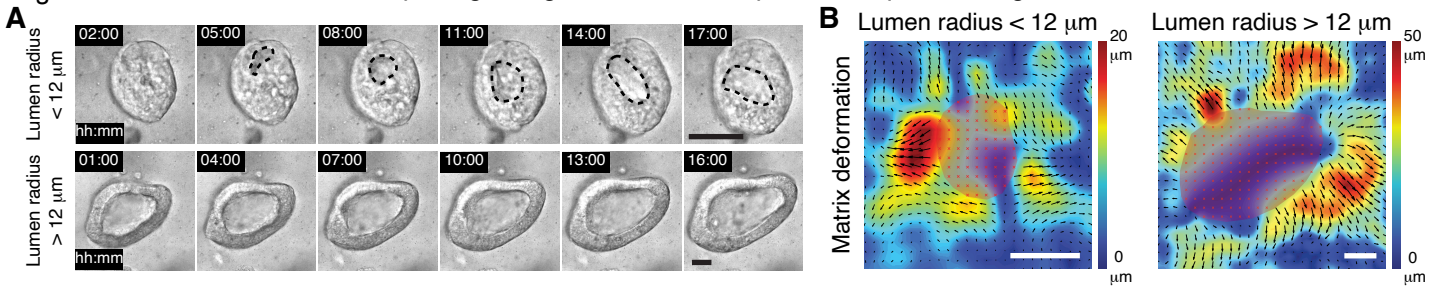

Actomyosin contractility does not drive lumen opening

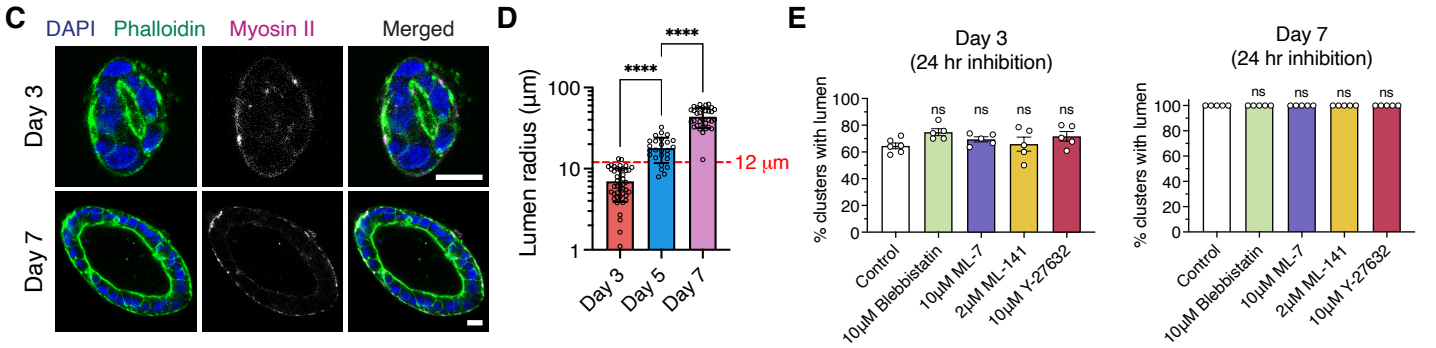

Actin forms a mesh-like structure apically that attains a mature size at 12 μm lumen radius

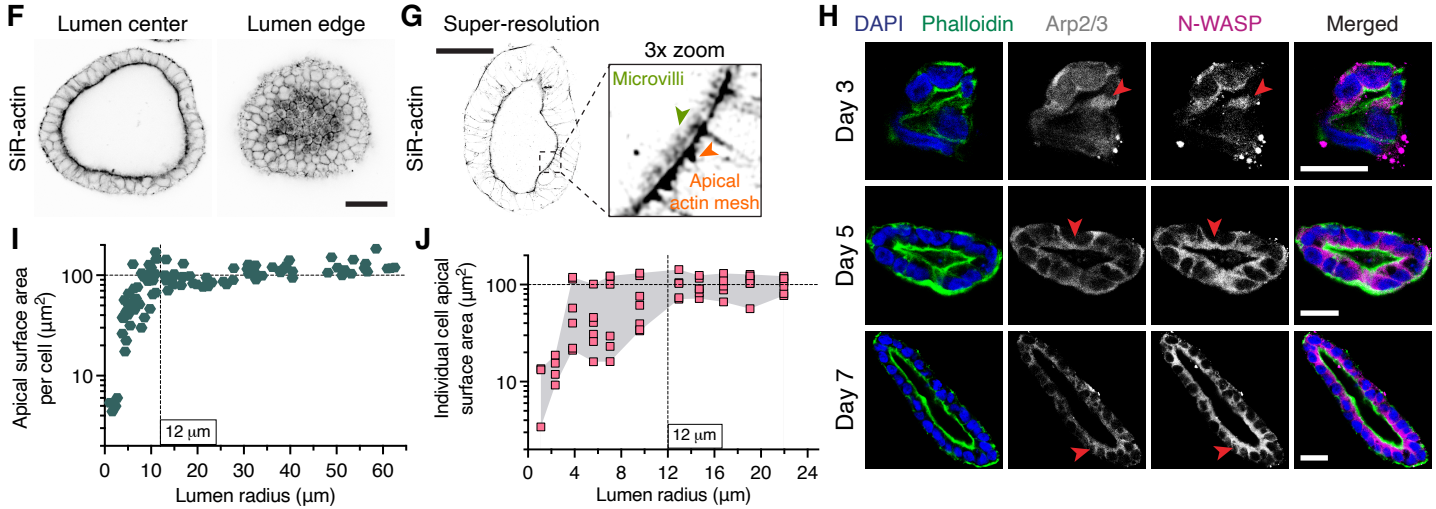

Lumen opening requires actin polymerization

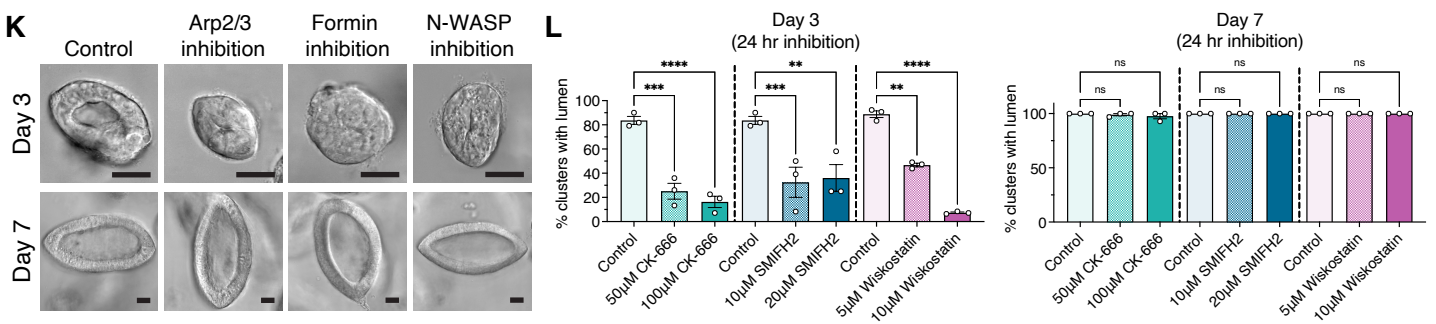

Figure

Apical actin polymerization drives lumen expansion in smaller epiblasts

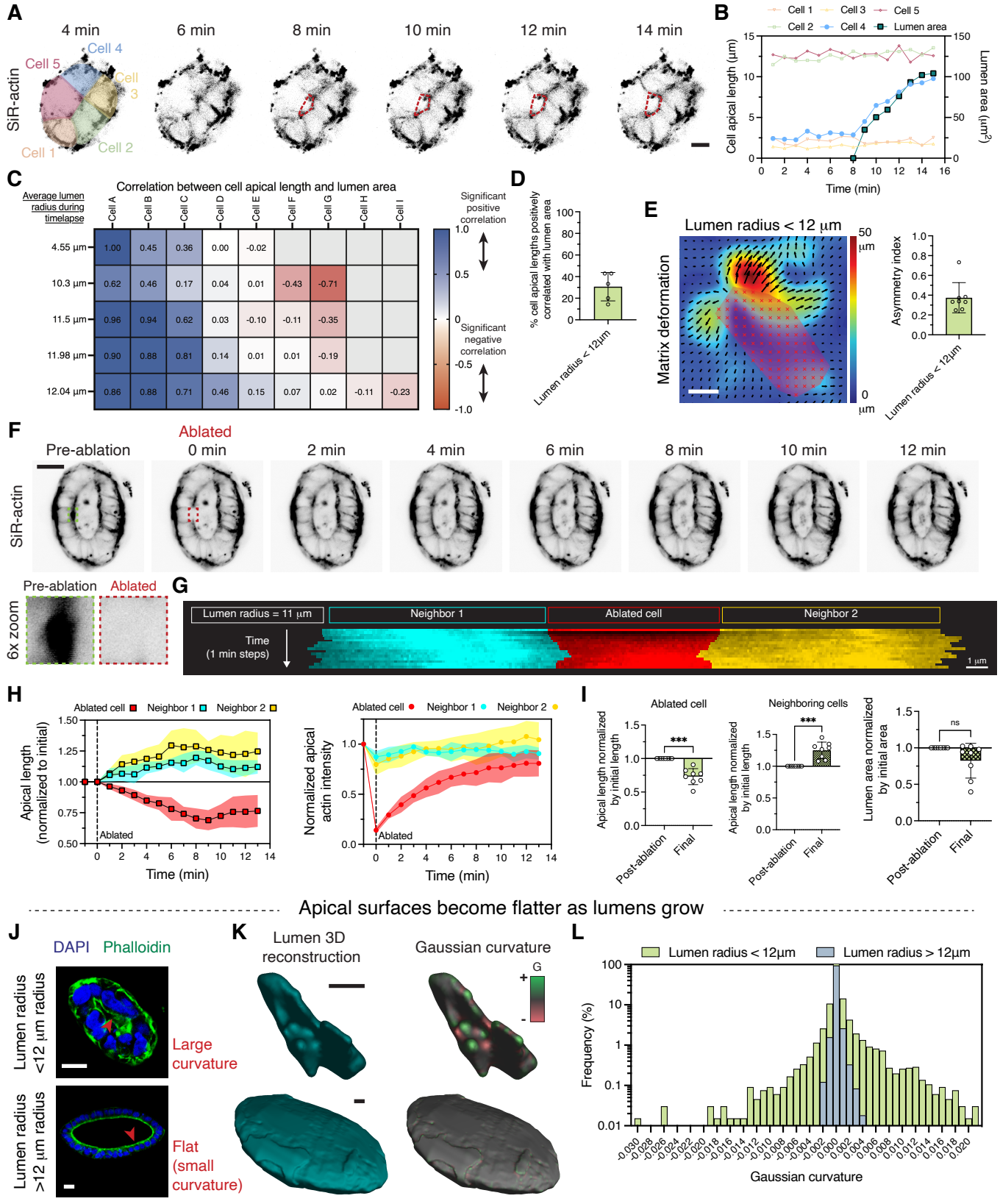

Figure

Cell geometric constraints dictate evolution of apical surface area and lumen size

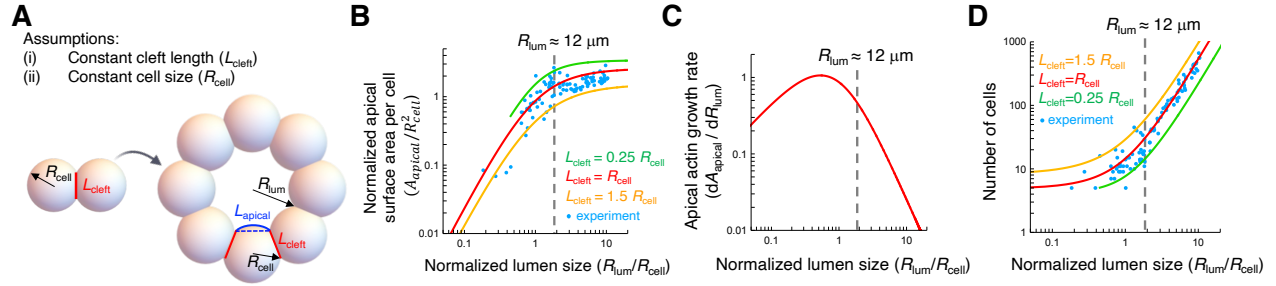

Physical model of actin polymerization driven lumen expansion

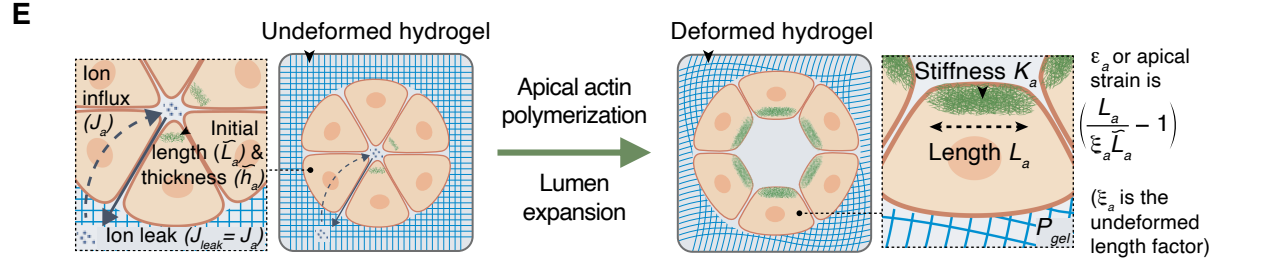

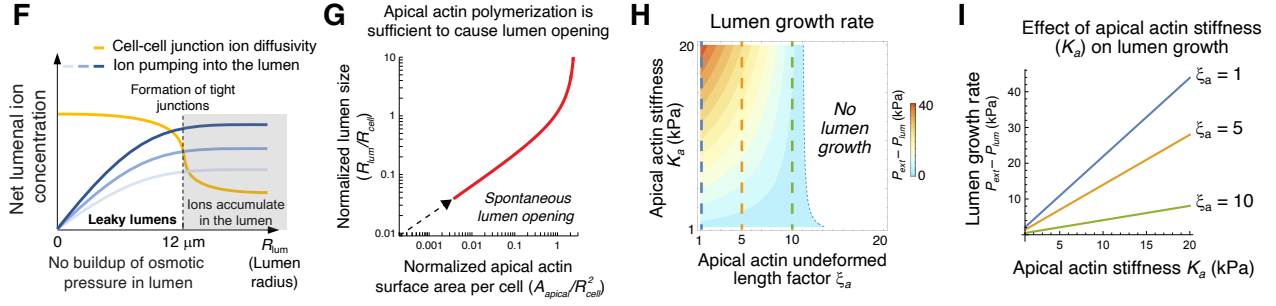

Transition to pressure-driven growth is necessary to avoid buckling of the cell layer

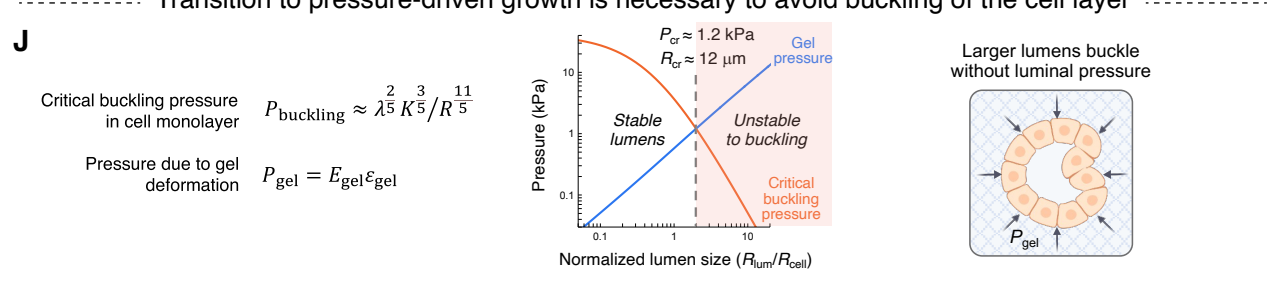

Figure

Osmotic pressure drives lumen growth in lumens >12 μm radius

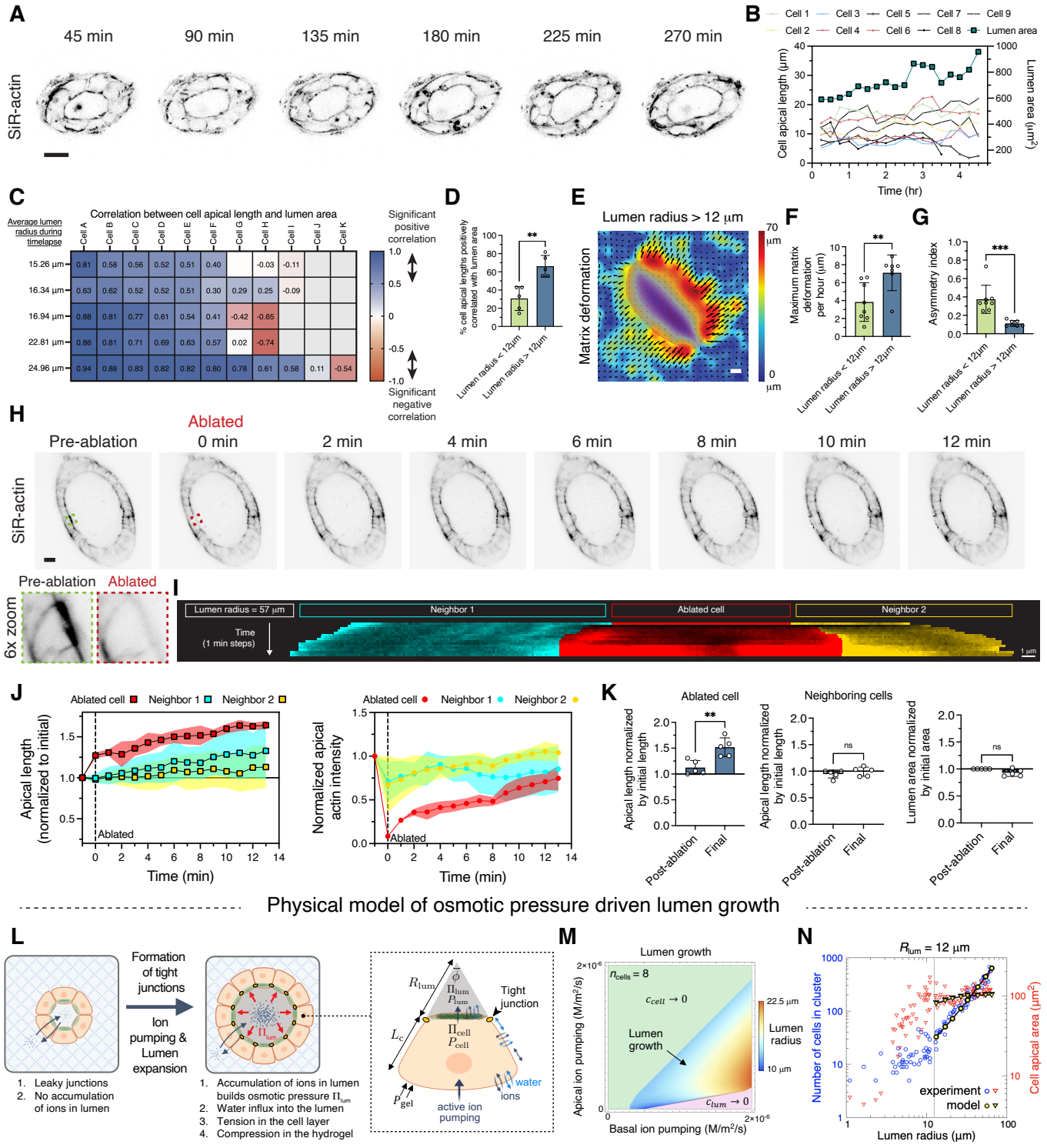

Physical model of osmotic pressure driven lumen growth

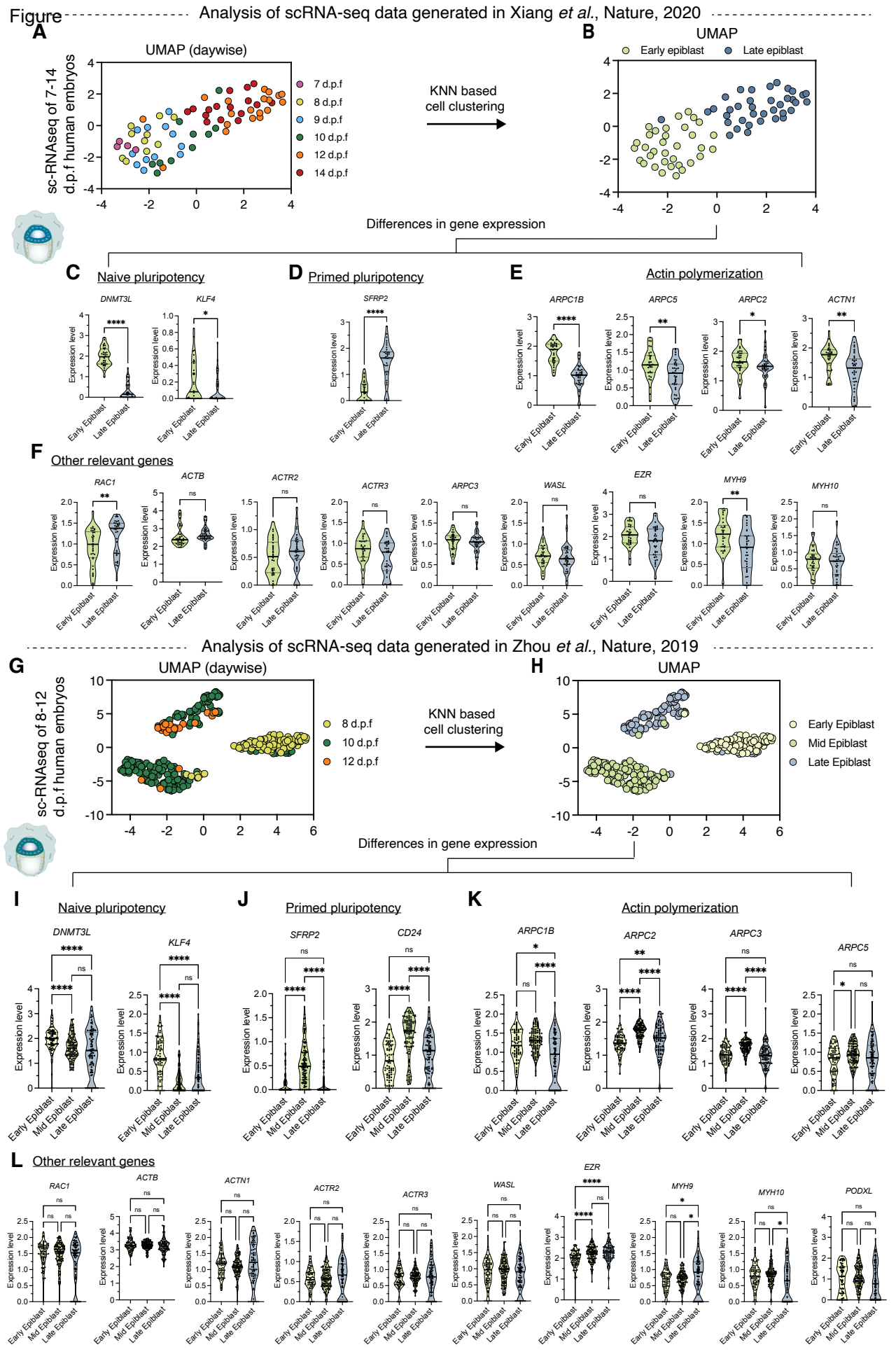
Figure
Analysis of scRNA-seq data generated in Xiang et al., Nature, 2020
A
UMAP (daywise)
sc-RNAseq of 7-14 d.p.f human embryos
7 d.p.f
8 d.p.f
9 d.p.f
10 d.p.f
12 d.p.f
14 d.p.f
KNN based cell clustering
B
UMAP
Early epiblast
Late epiblast
Differences in gene expression
C
Naive pluripotency
DNMT3L
KLF4
D
Primed pluripotency
SFRP2
E
Actin polymerization
ARPC1B
ARPC5
ARPC2
ACTN1
F
Other relevant genes
RAC1
ACTB
ACTR2
ACTR3
ARPC3
WASL
EZR
MYH9
MYH10
Expression level
Early Epiblast
Late Epiblast
Analysis of scRNA-seq data generated in Zhou et al., Nature, 2019
G
UMAP (daywise)
sc-RNAseq of 8-12 d.p.f human embryos
8 d.p.f
10 d.p.f
12 d.p.f
KNN based cell clustering
H
UMAP
Early Epiblast
Mid Epiblast
Late Epiblast
Differences in gene expression
I
Naive pluripotency
DNMT3L
KLF4
J
Primed pluripotency
SFRP2
CD24
K
Actin polymerization
ARPC1B
ARPC2
ARPC3
ARPC5
L
Other relevant genes
RAC1
ACTB
ACTN1
ACTR2
ACTR3
WASL
EZR
MYH9
MYH10
PODXL
Expression level
Early Epiblast
Mid Epiblast
Late Epiblast

Figure

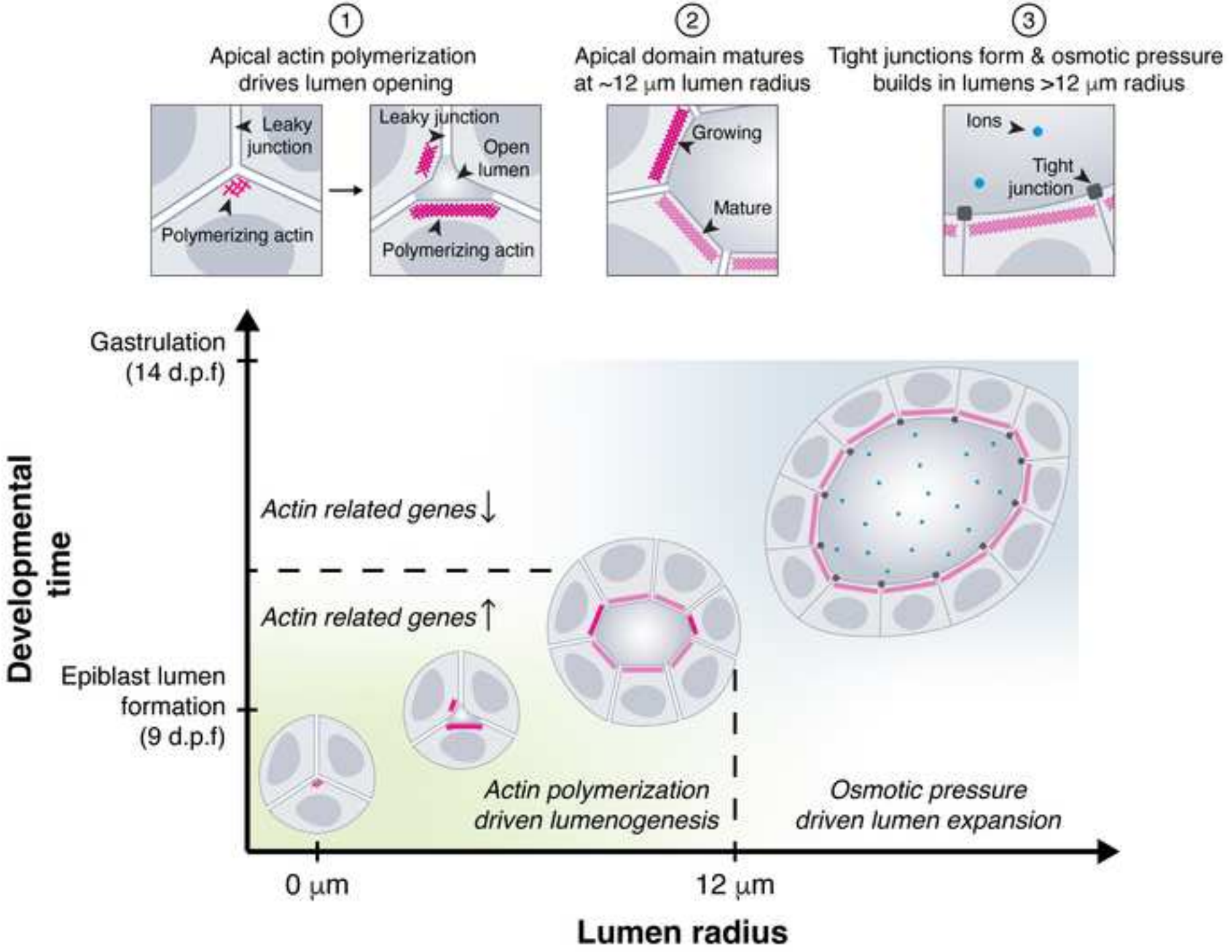

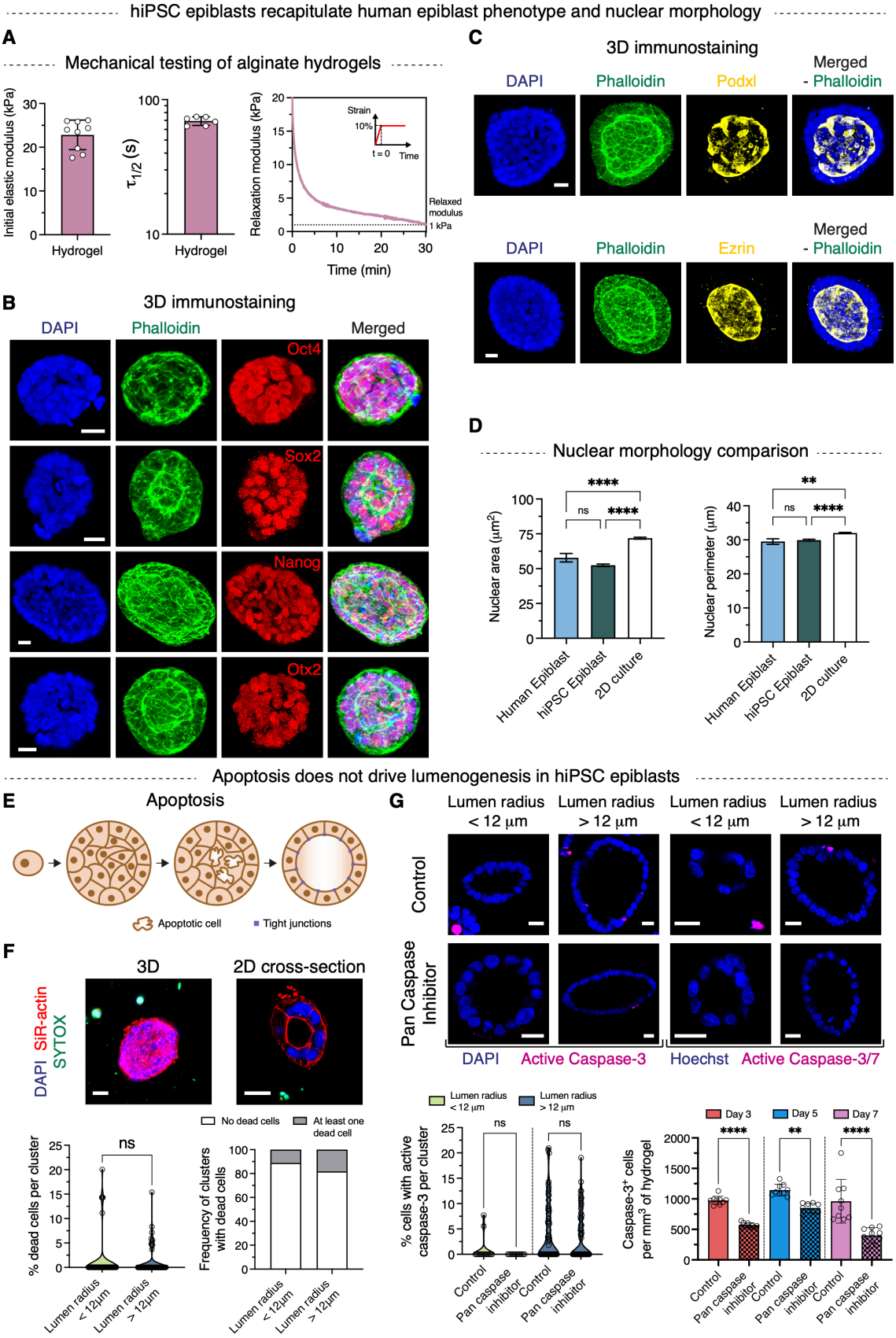
hiPSC epiblasts recapitulate human epiblast phenotype and nuclear morphology
A
Mechanical testing of alginate hydrogels
Initial elastic modulus (kPa)
Hydrogel
τ1/2 (s)
Hydrogel
Relaxation modulus (kPa)
Strain
10%
t = 0
Time
Relaxed modulus 1 kPa
Time (min)
B
3D immunostaining
DAPI
Phalloidin
Merged
Oct4
Sox2
Nanog
Otx2
C
3D immunostaining
DAPI
Phalloidin
Podxl
Merged - Phalloidin
DAPI
Phalloidin
Ezrin
Merged - Phalloidin
D
Nuclear morphology comparison
Nuclear area (μm²)
Nuclear perimeter (μm)
ns
****
**
Human Epiblast
hiPSC Epiblast
2D culture
Apoptosis does not drive lumenogenesis in hiPSC epiblasts
E
Apoptosis
Apoptotic cell
Tight junctions
F
3D
2D cross-section
DAPI SiR-actin SYTOX
% dead cells per cluster
Frequency of clusters with dead cells
No dead cells
At least one dead cell
Lumen radius < 12μm
Lumen radius > 12μm
G
Lumen radius < 12 μm
Lumen radius > 12 μm
Control
Pan Caspase Inhibitor
DAPI
Active Caspase-3
Hoechst
Active Caspase-3/7
% cells with active caspase-3 per cluster
Caspase-3⁺ cells per mm³ of hydrogel
Day 3
Day 5
Day 7
Control
Pan caspase inhibitor

Figure S1 [supporting Fig. 1]: hiPSC epiblasts model human epiblasts and apoptosis does not drive lumen growth in hiPSC epiblasts. (A) Mechanical characterization of viscoelastic alginate hydrogels using compression testing. Measurements of initial elastic modulus and stress relaxation were performed (mean ± s.d.; $n \geq 6$). $\tau_{1/2}$ is the timescale of stress relaxation, defined as the time when the relaxation modulus reaches 50% of initial value. Representative stress relaxation profile of alginate hydrogels at 10% compressive strain is shown. Inset indicates applied strain profile. Final relaxed modulus of alginate hydrogels is ~1 kPa. **(B)** Maximum intensity projections of 3D immunostains of pluripotency markers Oct4, Sox2, Nanog, Otx2 (formative pluripotency), phalloidin (F-actin) and DAPI (nucleus) in hiPSC epiblasts. **(C)** Maximum intensity projections of 3D immunostains of Podocalyxin, Ezrin (apical polarity), phalloidin (F-actin) and DAPI (nucleus) in hiPSC epiblasts. **(D)** Quantification of nuclear area and perimeter in human and hiPSC epiblasts, as well as in 2D culture of hiPSCs (mean ± s.e.m.; ****$p < 0.0001$, **$p < 0.01$, ns: not significant $p > 0.05$, one-way ANOVA; n = 137 (human epiblast nuclei), 435 (hiPSC epiblast nuclei), 2607 (2D culture nuclei); N = 3 biological replicates). See materials and methods section for sources of human epiblast and 2D culture images. **(E)** Schematic of apoptosis driven lumen growth. **(F)** SYTOX assay. Fluorescence images of live cells stained with SYTOX (dead cells), SiR-actin (F-actin) and DAPI (nucleus). Quantification of percentage dead cells per cluster (ns: not significant $p > 0.05$, Mann-Whitney; n = 54 (smaller epiblasts), 56 (larger epiblasts)), and quantification of frequency of clusters with and without dead cells (n = 54 (smaller epiblasts), 56 (larger epiblasts); N = 2 biological replicates). **(G)** Fluorescence images of live cells stained for active caspase-3/7 (apoptotic cells), and Hoechst (nucleus), and fixed cells stained for active caspase-3, and DAPI (nucleus), with and without a pan caspase inhibitor (Z-VAD-FMK). Quantification of percentage apoptotic cells per cluster (ns: not significant $p > 0.05$, Kruskal-Wallis; n = 16 (smaller epiblasts control), 13 (smaller epiblasts with pan caspase inhibitor), 62 (larger epiblasts control), 67 (larger epiblasts with pan caspase inhibitor); N = 2 biological replicates), and quantification of number of apoptotic cells with and without a pan caspase inhibitor (mean ± s.d.; ****$p < 0.0001$, **$p < 0.01$, one-way ANOVA; n = 9 (for all experimental groups); N = 2 biological replicates). Scale bars: 20 μm (B, C, F and G).

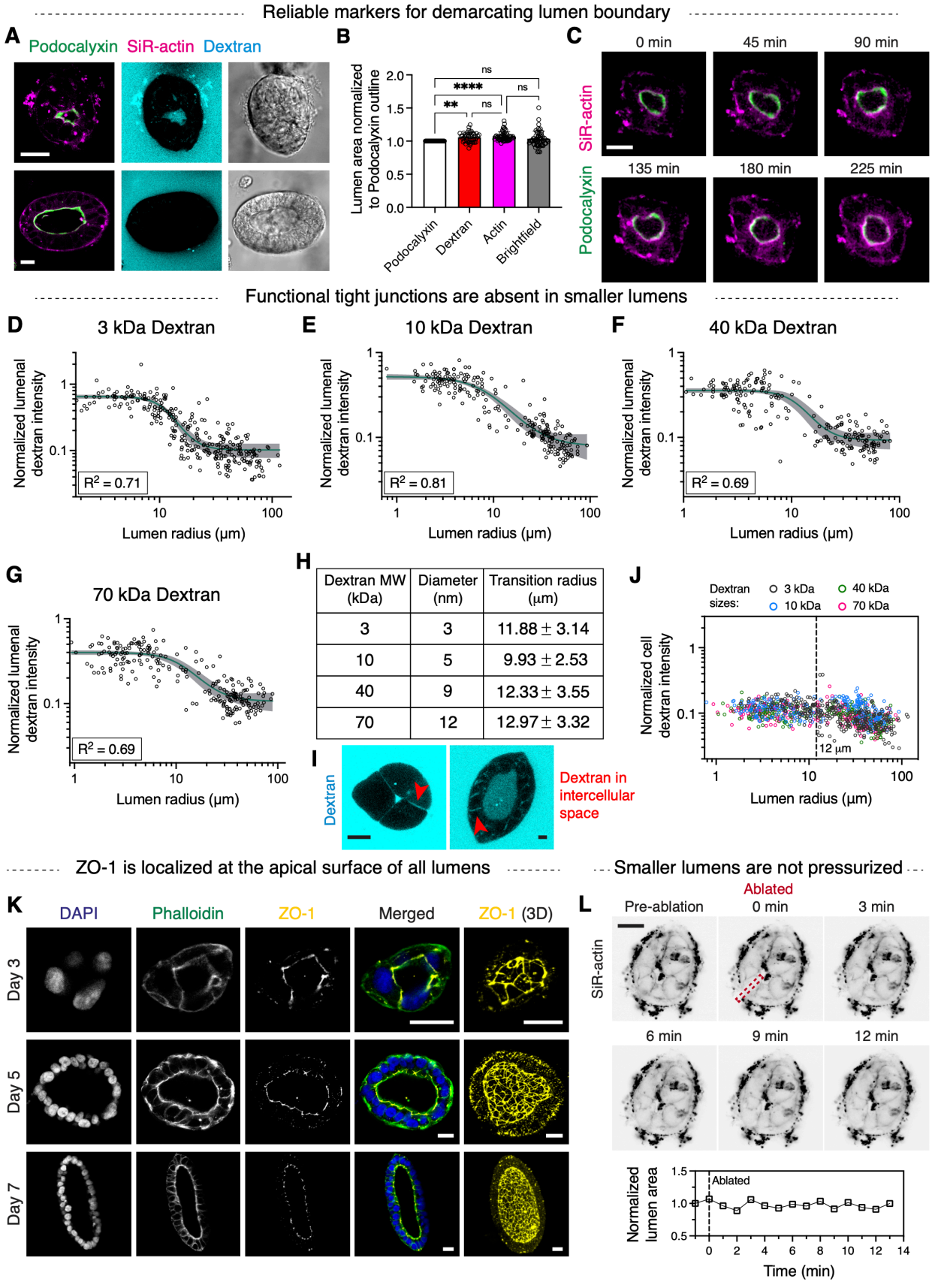
Reliable markers for demarcating lumen boundary
A
Podocalyxin SiR-actin Dextran
B
Lumen area normalized to Podocalyxin outline
ns
****
**
ns
ns
Podocalyxin
Dextran
Actin
Brightfield
C
0 min
45 min
90 min
135 min
180 min
225 min
SiR-actin
Podocalyxin
Functional tight junctions are absent in smaller lumens
D
3 kDa Dextran
E
10 kDa Dextran
F
40 kDa Dextran
Normalized lumenal dextran intensity
Lumen radius (μm)
R² = 0.71
R² = 0.81
R² = 0.69
G
70 kDa Dextran
R² = 0.69
H
Dextran MW (kDa) | Diameter (nm) | Transition radius (μm)
3 | 3 | 11.88 ± 3.14
10 | 5 | 9.93 ± 2.53
40 | 9 | 12.33 ± 3.55
70 | 12 | 12.97 ± 3.32
I
Dextran
Dextran in intercellular space
J
Dextran sizes: 3 kDa 10 kDa 40 kDa 70 kDa
Normalized cell dextran intensity
12 μm
ZO-1 is localized at the apical surface of all lumens
K
DAPI
Phalloidin
ZO-1
Merged
ZO-1 (3D)
Day 3
Day 5
Day 7
Smaller lumens are not pressurized
L
Ablated
Pre-ablation
0 min
3 min
6 min
9 min
12 min
SiR-actin
Normalized lumen area
Ablated
Time (min)

Figure S2 [supporting Fig. 1]: F-actin, dextran and brightfield images allow reliable demarcation of the lumen boundary and functional tight junctions are absent in smaller epiblasts. (A) Representative fluorescent images of podocalyxin (PODXL-EGFP cell line), F-actin (SiR-actin), and dextran as well as brightfield images of hPSC epiblasts. **(B)** Area of lumen outlines drawn using fluorescent images of podocalyxin (PODXL-EGFP cell line), F-actin (SiR-actin), dextran and brightfield images normalized to podocalyxin outlines (mean ± s.d.; ****$p < 0.0001$, **$p < 0.01$, ns: not significant $p > 0.05$, one-way ANOVA; $n = 56$ (podocalyxin, F-actin and brightfield), 47 (dextran); $N = 2$ biological replicates). **(C)** Timelapse images of hPSC epiblasts with fluorescently labelled podocalyxin (PODXL-EGFP cell line) and F-actin (SiR-actin). Scale bars: **(D to G)** Individual plots showing quantification of dextran intensity inside lumen for different dextran sizes: 3 kDa (D), 10 kDa (E), 40 kDa (F), 70 kDa (G). Lines indicate sigmoidal fits and 95% CI. (n, R^2) = 3 kDa: (290, 0.71), 10 kDa: (229, 0.81), 40 kDa: (213, 0.69), 70 kDa: (228, 0.69). **(H)** Table summarizing dextran sizes (from manufacturer) and respective IC50 or sigmoid fit inflection point values. **(I)** Representative fluorescence image of dextran (3 kDa) in smaller lumens. Image brightness was increased to visualize dextran in the intercellular spaces. **(J)** Quantification of fluorescent dextran intensity inside cells normalized to that in the hydrogel. This intensity value represents noise in imaging, as dextran is cell impermeable. **(K)** Immunostains and maximum intensity projections of 3D immunostains of ZO-1 (tight junction protein), phalloidin (F-actin) and DAPI (nucleus) in hiPSC epiblasts on different days of culture. **(L)** Laser ablation through an entire cell and quantification of lumen area pre- and post-ablation. No large change in lumen area is observed post-ablation, suggesting that smaller lumens are not pressurized. Scale bars: 20 μm (A, C, K, and L) and 10 μm (I).

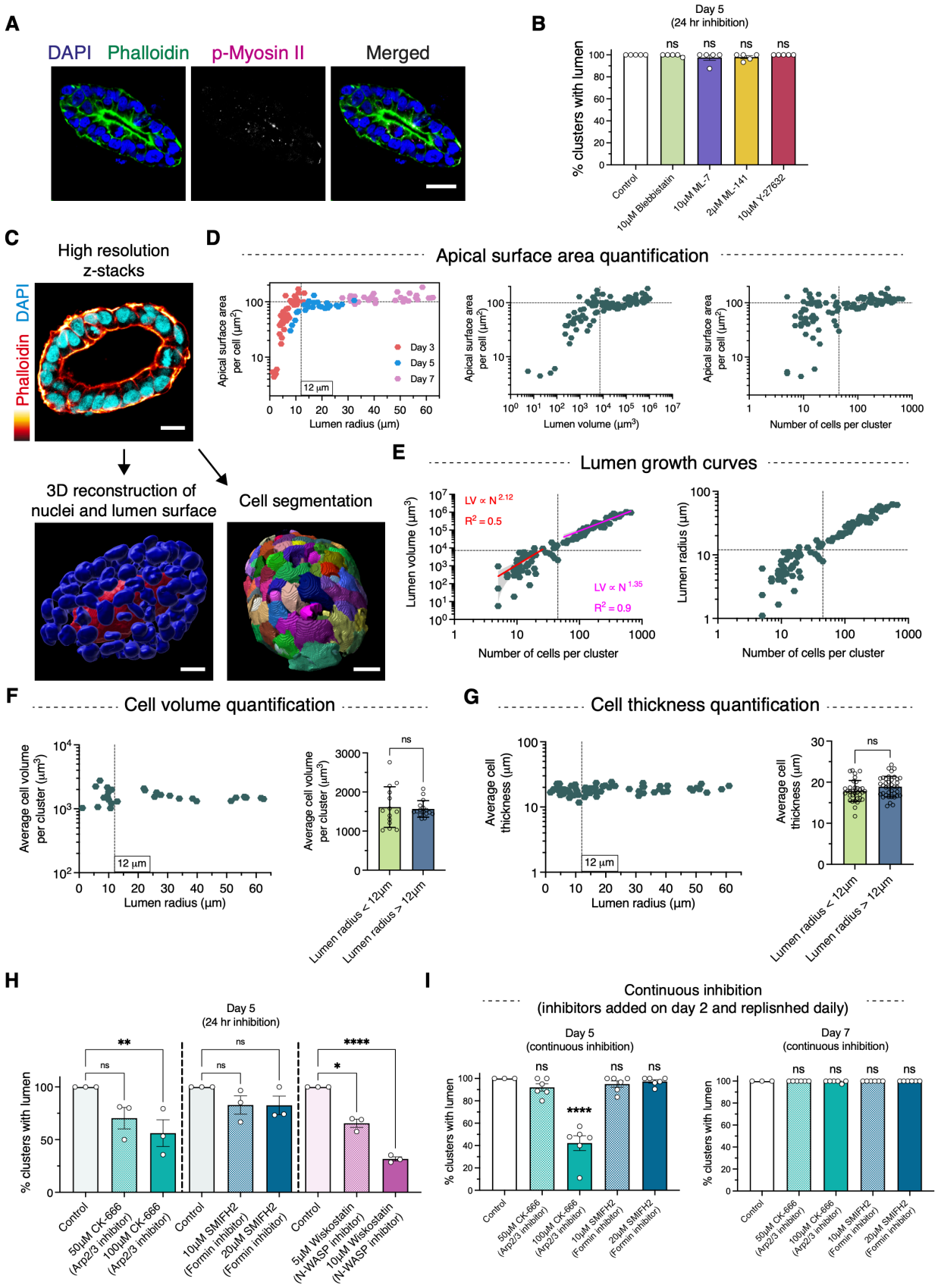
A
DAPI
Phalloidin
p-Myosin II
Merged
B
Day 5
(24 hr inhibition)
% clusters with lumen
ns
Control
10μM Blebbistatin
10μM ML-7
2μM ML-141
10μM Y-27632
C
High resolution
z-stacks
DAPI
Phalloidin
3D reconstruction of
nuclei and lumen surface
Cell segmentation
D
Apical surface area quantification
Apical surface area
per cell (μm²)
Lumen radius (μm)
12 μm
Day 3
Day 5
Day 7
Lumen volume (μm³)
Number of cells per cluster
E
Lumen growth curves
Lumen volume (μm³)
LV ∝ N 2.12
R² = 0.5
LV ∝ N 1.35
R² = 0.9
Lumen radius (μm)
Number of cells per cluster
F
Cell volume quantification
Average cell volume
per cluster (μm³)
Lumen radius (μm)
Lumen radius < 12μm
Lumen radius > 12μm
G
Cell thickness quantification
Average cell
thickness (μm)
H
Day 5
(24 hr inhibition)
50μM CK-666
(Arp2/3 inhibitor)
100μM CK-666
(Arp2/3 inhibitor)
10μM SMIFH2
(Formin inhibitor)
20μM SMIFH2
(Formin inhibitor)
5μM Wiskostatin
(N-WASP inhibitor)
10μM Wiskostatin
(N-WASP inhibitor)
I
Continuous inhibition
(inhibitors added on day 2 and replisnhed daily)
Day 5
(continuous inhibition)
Day 7
(continuous inhibition)

Figure S3 [supporting Fig. 2]: Actin polymerization is necessary for lumen growth and the two size-dependent mechanisms of lumen growth show distinct growth dynamics. (A) Immunostains of phosphorylated myosin II, phalloidin (F-actin) and DAPI (nucleus) in hiPSC epiblasts. **(B)** Percent epiblasts with lumen in the presence of different actomyosin contractility inhibitors on day 5 of culture (mean ± s.e.m.; ns: not significant $p > 0.05$, one-way ANOVA; $n \geq 5$; $N = 3$ biological replicates). **(C)** Image analysis pipeline for quantification of lumen and cell size metrics from 3D z-stacks of phalloidin (F-actin) and DAPI (nucleus) stained hiPSC epiblasts. **(D)** Quantification of average apical surface area per cell as a function of lumen radius, lumen volume or number of cells (n = 101 hiPSC epiblasts). **(E)** Quantification of lumen growth dynamics (n = 101 hiPSC epiblasts). Smaller lumens grow faster than large lumens for a fixed number of cells (N). Lines indicate power law fits. For smaller lumens, lumen volume (LV) $\propto N^{2.12}$ ($R^2 = 0.5$) and for larger lumens, LV $\propto N^{1.35}$ ($R^2 = 0.9$). **(F)** Quantification of cell volume as a function of lumen radius (mean ± s.d.; ns: not significant $p > 0.05$, Mann-Whitney; $n = 30$ hiPSC epiblasts; $N = 3$ biological replicates). **(G)** Quantification of cell layer thickness as a function of lumen radius (mean ± s.d.; ns: not significant $p > 0.05$, Mann-Whitney; $n = 71$ hiPSC epiblasts; $N = 3$ biological replicates). **(H to I)** Percent epiblasts with lumen in the presence of Arp2/3 (CK-666), formin (SMIFH2) and N-WASP (Wiskostatin) inhibitors for either 24 hr (H) or continuously from day 2 onwards (I) (mean ± s.e.m.; ****$p < 0.0001$, **$p < 0.01$, *$p < 0.05$, ns: not significant $p > 0.05$, one-way ANOVA; $n = 3$; $N = 3$ biological replicates). Scale bar: 20 μm (A and C).

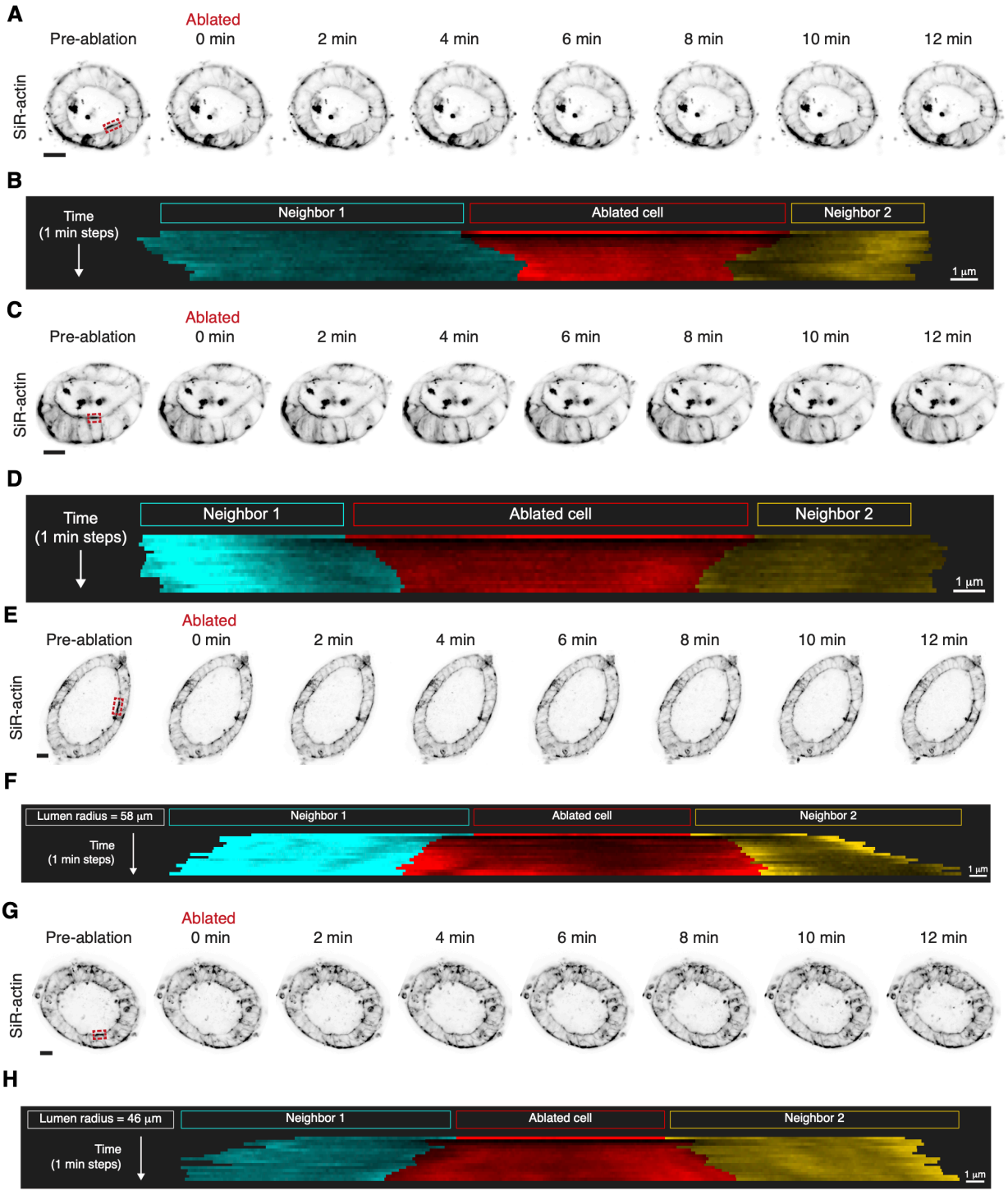

Figure S4 [supporting Figs. 3 and 5]: Apical actin ablation in hiPSC epiblasts. (A and C) Apical actin ablation and recovery in smaller epiblasts. Red outline indicates ablated surface. **(B and D)** Kymograph showing apical actin of ablated and neighboring cells for smaller epiblasts shown in (A) and (C) respectively. **(E and G)** Apical actin ablation and recovery in larger epiblasts.

Red outline indicates ablated surface. **(F and H)** Kymograph showing apical actin of ablated and neighboring cells for larger epiblasts shown in (E) and (G) respectively. Scale bars: 20 μm (A, C, E and G), 1 μm (B, D, F and H).

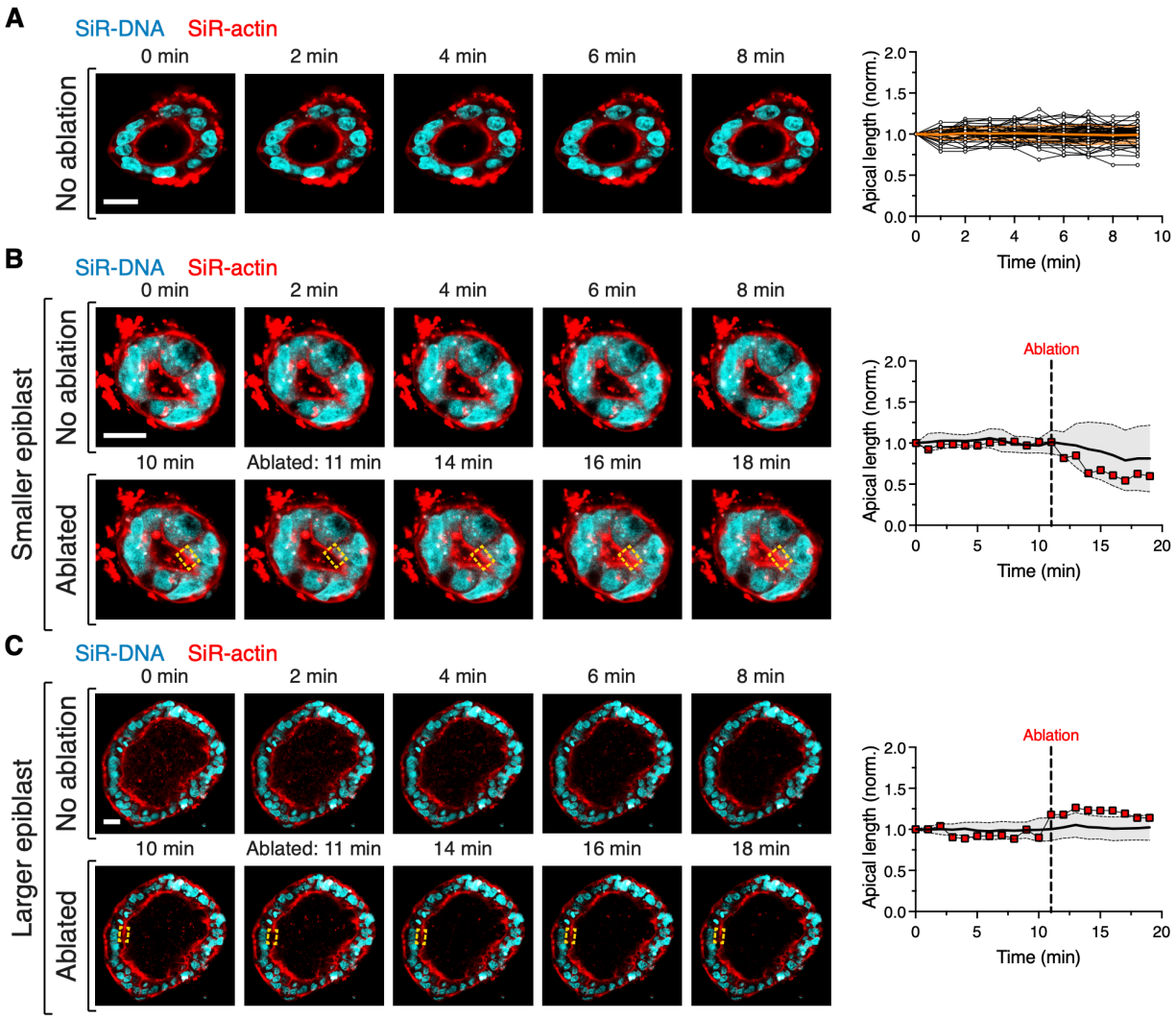

Figure S5 [supporting Figs. 3 and 5]: Laser ablation drastically alters apical length dynamics as compared to non-ablated controls on a timescale of minutes. (A) Fluorescent timelapse images of F-actin (SiR-actin) and nucleus (SiR-DNA) over 10 minutes (similar to the duration of ablation experiments) in hiPSC epiblasts and quantification of apical lengths of individual cells during this time period. Black lines indicate apical lengths of individual cells normalized to initial length. Yellow curve indicates the mean and s.d. of normalized apical lengths (n = 53 hiPSCs from 4 epiblasts). **(B and C)** Fluorescent timelapse images of F-actin (SiR-actin) and nucleus (SiR-DNA) in a smaller (B) and larger (C) epiblasts and quantification of apical lengths of individual cells during this time period. Yellow boxes indicate ablated cell. Black lines indicate mean and s.d. of normalized apical lengths (n = 8 hiPSCs for (B) and n = 29 hiPSCs for (C)). Red dots indicate normalized apical lengths of ablated cell pre- and post-ablation. Scale bars: 20 μm (A to C).

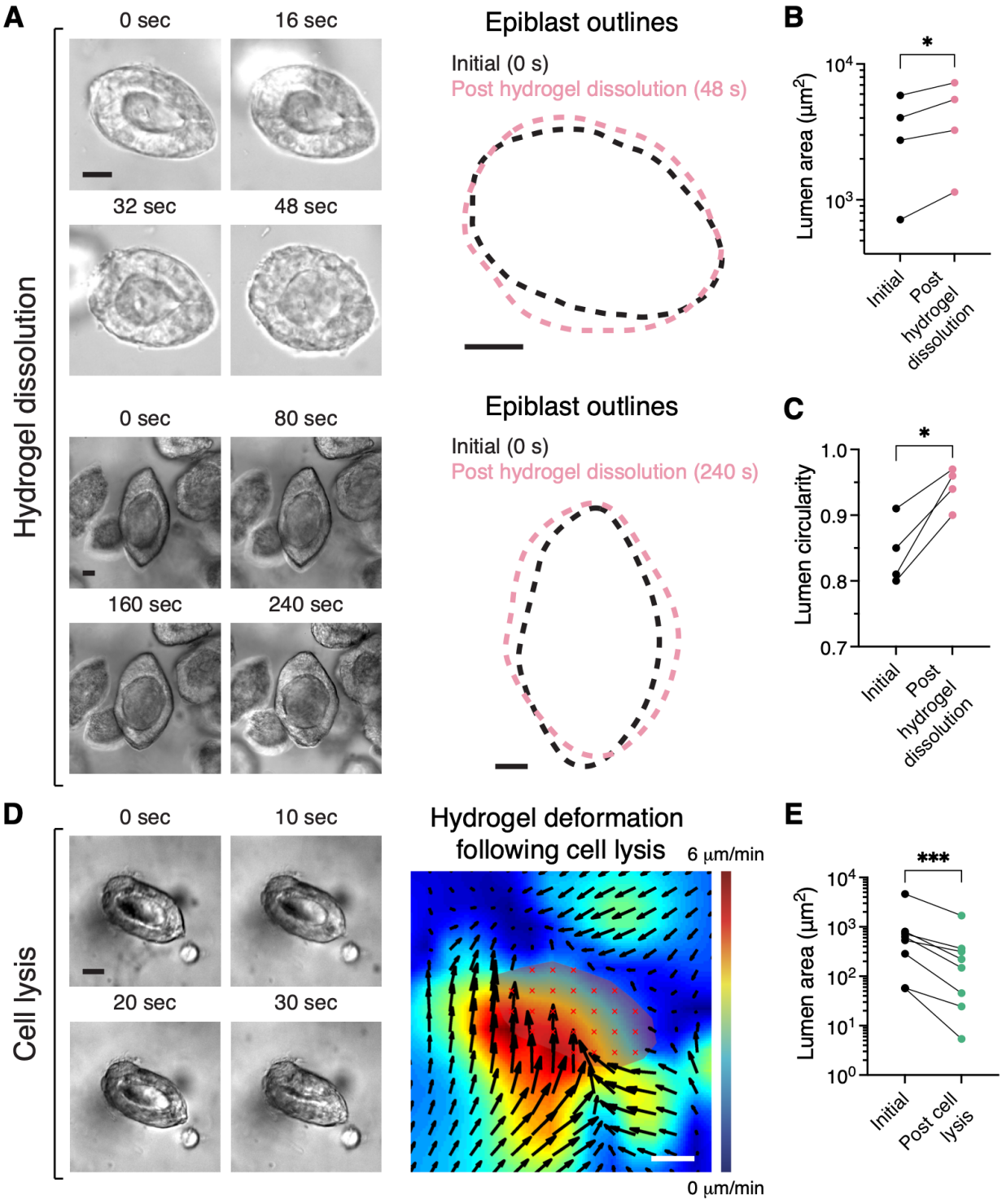

Figure S6 [supporting Figs. 3 and 5]: hiPSC epiblasts in alginate hydrogels are under compression and exert compressive stresses on the hydrogel. (A) Timelapse (brightfield) images of hiPSC epiblasts and epiblast outlines pre- and post-hydrogel dissolution. **(B)** Quantification of lumen area of hiPSC epiblasts pre- and post-hydrogel dissolution (*p < 0.05,

ratio paired t test; $n = 4$ (hiPSC epiblasts); $N = 4$ biological replicates). **(C)** Quantification of lumen circularity of hiPSC epiblasts pre- and post-hydrogel dissolution (*$p < 0.05$, ratio paired t test; $n = 4$ (hiPSC epiblasts); $N = 4$ biological replicates). Upon hydrogel dissolution, hiPSC epiblasts expand in size and become more spherical indicating that hiPSC epiblasts are under compression in alginate hydrogels. **(D)** Timelapse (brightfield) images of hiPSC epiblasts and quantification of respective hydrogel deformation upon cell lysis. Upon cell lysis, lumen collapses and hydrogel surrounding the epiblast expands into the epiblast indicating that hydrogel is under compression. **(E)** Quantification of lumen area of hiPSC epiblasts pre- and post-cell lysis (***$p < 0.001$, ratio paired t test; $n = 8$ (hiPSC epiblasts); $N = 4$ biological replicates). Scale bars: 20 μm (A and D).

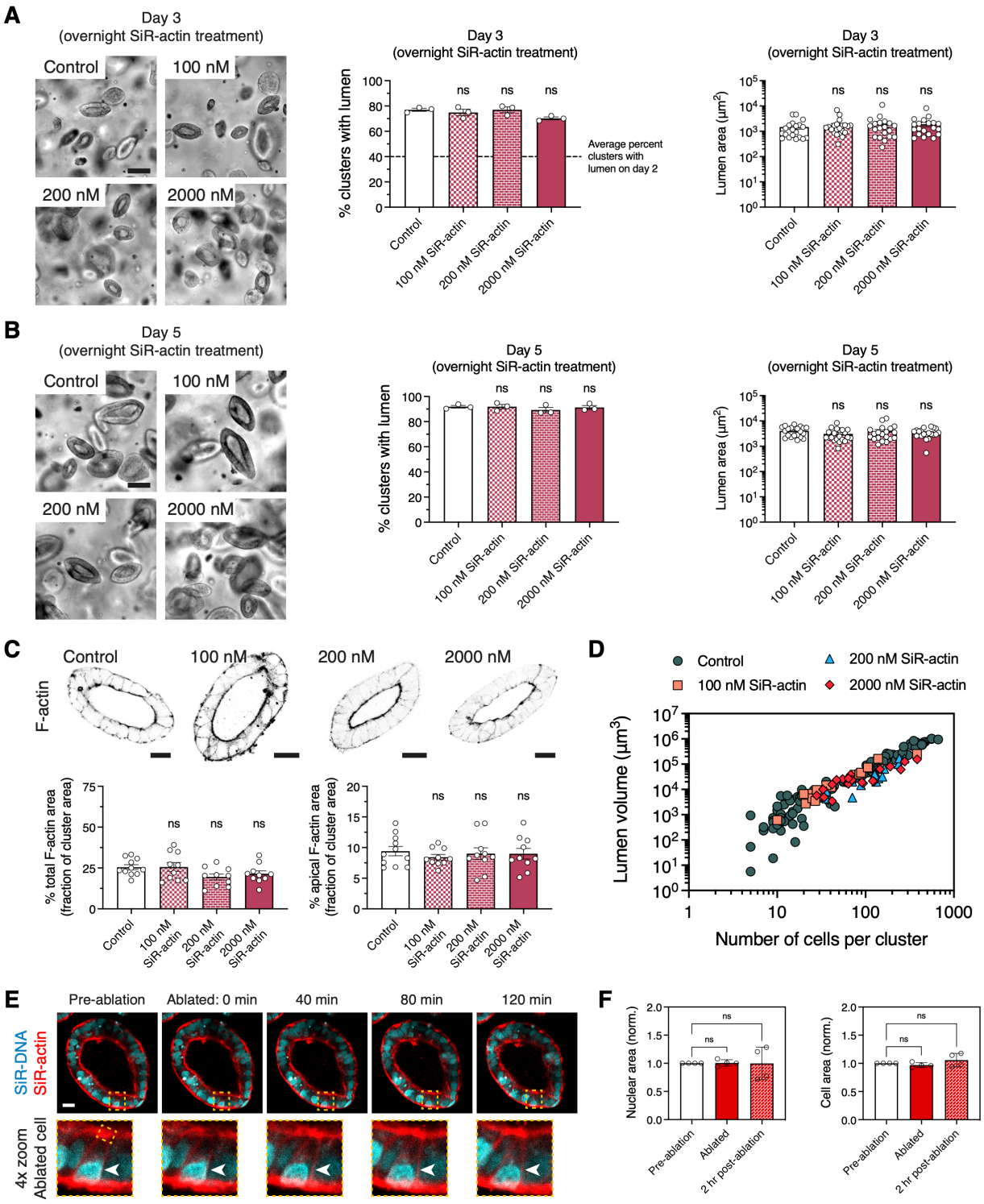

Figure S7 [supporting Figs. 3 and 5]: SiR-actin does not impact F-actin or hiPSC epiblast morphogenesis and laser ablation of apical surface does not disrupt cell viability. (A and B) Representative brightfield images and quantification of percent clusters with lumen and projected lumen area (μm^2) for control and samples treated overnight with 100 nM, 200 nM, or 2000 nM

SiR-actin on day 3 (A) and day 5 (B) of culture. For percent clusters with lumen plots, bars indicate mean ± s.e.m.; ns: not significant $p > 0.05$, one-way ANOVA; $n = 3$; $N = 3$ biological replicates per condition. For lumen area plots, bars indicate mean ± s.e.m.; ns: not significant $p > 0.05$, one-way ANOVA; $n = 20$ hiPSC epiblasts per condition; $N = 3$ biological replicates. Over the duration of treatment with SiR-actin, clusters in both control and SiR-actin treated samples showed lumen growth. Concentration of SiR-actin used for all other experiments is 100 nM. **(C)** Representative fluorescence images of F-actin (phalloidin or SiR-actin), and quantification of total and apical F-actin area as a percentage of total cluster area for control and samples treated overnight with 100 nM, 200 nM, or 2000 nM SiR-actin on day 3 and day 5 of culture. Bars indicate mean ± s.e.m.; ns: not significant $p > 0.05$, one-way ANOVA; $n = 10$ hiPSC epiblasts per condition; $N = 3$ biological replicates. **(D)** Quantification of lumen volume (μm^3) and cell numbers for control and samples treated overnight with 100 nM, 200 nM, or 2000 nM SiR-actin on day 3 and day 5 of culture. **(E)** Representative timelapse images of F-actin (SiR-actin) and DNA (SiR-DNA) pre- and post-ablation of apical surface of a single cell in hiPSC epiblasts. Yellow outlines and white arrows indicate ablated cell. **(F)** Quantification of nuclear and cell area of ablated cell pre- and 2 hr post-ablation (ns: not significant $p > 0.05$, one-way ANOVA; $n = 4$ (hiPSC epiblasts); $N = 2$ biological replicates). Scale bars: 100 μm (A and B), 25 μm (C) and 20 μm (E).

Methods S1 [supporting Figs. 4 and 5]: Procedures for computational modeling

In this Supplementary Methods section, we provide a detailed description of our model for lumen growth. This includes discussion of the main assumptions, equations and methods employed in our computations.

Model of lumen growth

As our experiments revealed two distinct mechanisms of lumen expansion (Supplementary Methods Fig. 1), we develop different modeling approaches to describe the observed behavior. In smaller epiblasts, the lack of functional tight junctions results in high permeability of intracellular clefts to ions and water, and absence of osmotic gradients across the cell layer. Despite this, epiblasts demonstrate spontaneous lumen opening, characterized by extensive actin network remodeling on the apical side of enclosing cells (Supplementary Methods Fig. 1). Once tight junctions form, ions start to accumulate in the lumen increasing its osmotic pressure, which is concomitant with a noticeable reduction in apical actin polymerization. Hence, the initial lumen opening is predominantly driven by mechanical forces exerted by cells, whereas lumen expansion at later stages becomes reliant on osmotic pressure forces generated by the lumen. This allows us to ignore osmotic effects in smaller lumens and examine the dependence of lumen opening on the geometrical constraints and mechanical properties of cell layer. At later stages, we describe lumen expansion using an osmotic model. The following sections detail the models and our choice of model parameters.

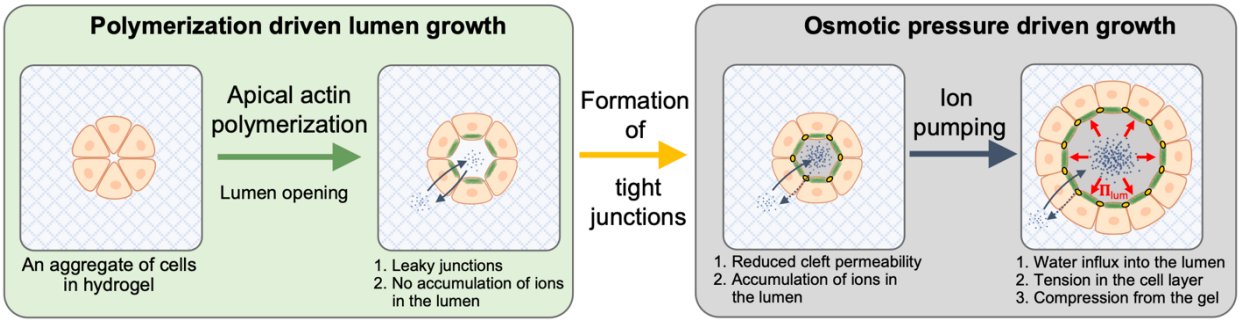

Supplementary Methods Fig. 1: Schematic of the two distinct lumen-sized dependent mechanisms of lumen growth.

A. Analytic predictions

For the purpose of analytical treatment, we employ a particle-based description and adopt a simplified geometry of a lumen-containing hiPSC epiblast. In this description, we model the monolayer of cells surrounding the lumen as a collection of spheres of radius R_{cell} that are closely packed on a spherical surface of a larger radius. Assuming rotational symmetry, we consider only the equatorial cross-section of the cell layer, which consists of n_{cells} spheres (Supplementary Methods Fig. 2A). To account for cell-cell adhesion, the spheres partly overlap forming a contact line of length L_{cleft}, which represents the effective surface tension and is influenced by the adhesion strength between cells. Increased adhesion will result in larger contact length and higher contact angle. Based on our experimental evidence that cell volume and cell layer thickness are conserved during lumen growth, in our model we assume that the cell radius and contact between cells, L_{cleft}, remain constant. These geometric constraints dictate how the lumen radius (R_{lum}) and the cell apical length (L_{apical}) depend on both the number of cells in the layer and the shape of individual cells:

$$R_{lum} = cot\frac{\pi}{n_{cells}}r - \frac{L_{cleft}}{2} \quad [1]$$

$$L_{apical} = R_{cell}(\pi - \frac{2\pi}{n_{cells}} - 2\arccos(\frac{r}{R_{cell}})) \quad [2]$$

where $r = \sqrt{R_{cell}^2 - L_{cleft}^2/4}$ is the distance between the cell center and the cleft.

The dependence of the normalized lumen radius on the apical length of cells at different cleft lengths are shown in Supplementary Methods Fig. 2B. The equatorial geometry can be translated into close packing of cells on a spherical surface, and, thus, the apical surface area of cells located at radius R_{lum} from the sphere center can be found as $A_{apical} \approx 2\sqrt{3}\,R_{cell}^2\,sin^2(\frac{L_{apical}}{2\,R_{cell}})$. When the cleft length decreases, for example due to reduced adhesion between cells, the model predicts spontaneous lumen opening since apical lengths increase. The imposed geometric constraints require rapid apical growth in smaller epiblasts (Supplementary

Methods Fig. 2C), reaching a maximum in epiblasts with a lumen radius of ~3 μm, which is predicted to monotonically decrease as lumen grows. This spontaneous lumen opening can be easily accommodated with a small increase in the number of cells. The predicted number of cells in a spherical epiblast can be found as $N_{cells} \approx 4\pi R_{lum}^2/A_{apical}$. The model's predictions for the number of cells at different lumen sizes is in excellent agreement with our experimental data (Supplementary Methods Fig. 2D). Furthermore, the model predicts that lumen expansion at earlier stages of epiblast growth requires a rapid increase in apical lengths, a process associated with dynamic formation and polymerization of the actin network.

As epiblasts are embedded in a gel that becomes compressed as the lumen expands, it is important to determine the critical lumen size at which the epiblast becomes unstable due to the pressure exerted by the gel. This critical size corresponds a configuration where the cell layer is prone to inward buckling to reduce deformations in the gel. The gel pressure is proportional to the Young's modulus of the gel E_{gel} and the amount of strain ε_{gel}, and reads as

$$P_{gel} = E_{gel}\varepsilon_{gel} \approx E_{gel}(\frac{R_{out}}{R_{out}^{ini}} - 1) \quad [3]$$

where $R_{out} = \frac{R+R_{cell}+R_{lum}+L_{cleft}}{2}$ is the average epiblast radius on the outer side of cells. Following Trusko et al. [S3], an approximation for the critical buckling pressure for an epithelium of thickness h, Young's modulus E, and Poisson ration ν can be written as

$$P_{buckling} \approx \lambda^{\frac{2}{5}} K^{\frac{3}{5}} / R^{\frac{11}{5}} \quad [4]$$

where $\lambda = Eh/(1-\nu^2)$, $K = Eh^3/(1-\nu^2)$ are compressional and bending rigidities of the monolayer, respectively, and R is the radius [S3]. Assuming an incompressible ($\nu = 0.5$) cell monolayer of thickness $h = L_{cleft} = R_{cell} = 6$ μm, apparent Young's modulus $E = 20$ kPa (following Harris et al. [S4]) and constrained by gel with modulus E_{gel} = 1 kPa, the buckling instability is predicted to occur when the lumen radius exceeds $R_{lum}/R_{cell} \approx 1.95$, corresponding to $R_{lum} \approx 12$ μm (Supplementary Methods Fig. 2E). This suggests that larger epiblasts are required to develop higher pressure in the lumen to counteract the force exerted by the gel and maintain their shape. However, lumens can maintain their symmetry when compression from the gel is small.

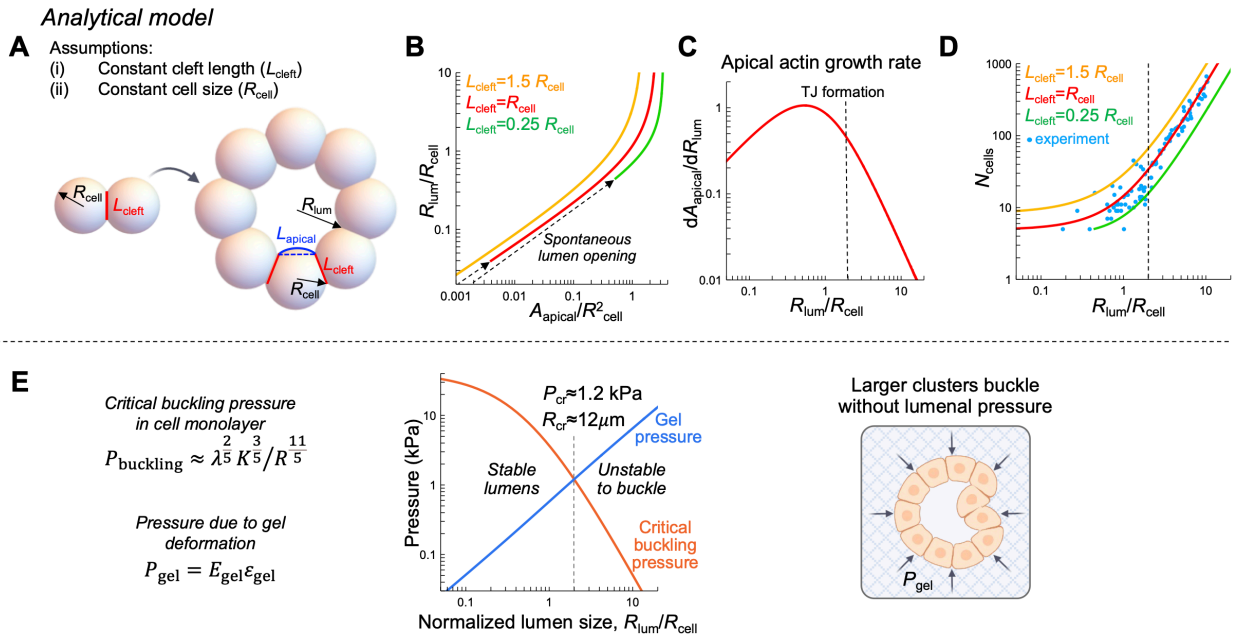

Supplementary Methods Fig. 2: Analytical model. (A to D) Schematic depicting our analytical model, designed to estimate the dependence of cell apical surface area and cell number on lumen size. The model assumes constant cell volume and cleft lengths. **(E)** Based on buckling pressure considerations, the onset of pressure driven lumen growth is predicted to occur when the lumen radius reaches approximately 12 μm. At this point the cell layer becomes unstable to buckling due to the pressure exerted by the surrounding gel.

Apical cortex stiffening drives water influx in smaller epiblasts

Through our experiments, we have discovered that smaller epiblasts lack tight junctions, which are essential for osmotic pressure buildup. In light of this finding, we explore and provide theoretical arguments to elucidate the role of actin polymerization in driving lumen growth (Supplementary Methods Fig. 3A and 3B).

The cell membrane's shape and size are regulated by the mechanical tension, primarily controlled by cortical stiffness and active actomyosin contractility. The resulting cortex stress depends on passive stresses σ^p due to deformations in the actin network, and active stress σ^a resulting from myosin motor activity. Assuming a linear stretch-stress relation for the passive stress, the passive stress at apical and basal sides of the cell can be written as $\sigma_a^p = K_a\left(\frac{L_a}{\xi_a \widetilde{L_a}} - 1\right), \sigma_b^p = K_b(\frac{L_b}{\widetilde{L_b}} - 1)$, respectively, where K_a, K_b are effective stiffnesses of the cortex,

L_a, L_b are apparent lengths of the cortex, $\widetilde{L_a}, \widetilde{L_b}$ are reference lengths of the cortex in an undeformed state, and ξ_a is the apical actin length factor that represents the growth on the apical side.

In the mechanical equilibrium, cell membrane tension, size of the cell (R_{cell}) and pressure difference across the membrane are related through the Laplace law, which for the apical and basal sides reads as

$$\Delta P_a = P_{cell} - P_{lumen} = \frac{2\xi_a h_a(\sigma_a^p + \sigma_a^a)}{R_{cell}} = \frac{2\xi_a h_a\left(K_a\left(\frac{L_a}{\xi_a \widetilde{L_a}} - 1\right) + \sigma_a^a\right)}{R_{cell}}, \quad [5]$$

$$\Delta P_b = P_{cell} - P_{ext} = \frac{2h_b(\sigma_b^p + \sigma_b^a)}{R_{cell}} + P_{gel} = \frac{2h_b\left(K_b(\frac{L_b}{\widetilde{L_b}} - 1) + \sigma_b^a\right)}{R_{cell}} + P_{gel}, \quad [6]$$

where $\Delta P_b, \Delta P_a$ are the gradients in the hydrostatic pressure, h_b, h_a are thicknesses of the cortical layer, and P_{gel} is the pressure from gel due to its deformation as lumen grows.

Our experimental findings demonstrated that cells do not change their size and retain a spherical shape in small lumens (Figures 1B-C). Additionally, our observations revealed that significant actin network rearrangements occur at the apical side, even when stresses on the apical side remain small (Figures 3F-I). Based on these findings, the difference in hydrostatic pressure jump across basal and apical sides will be equal to the pressure difference between the lumen and external media

$$\Delta P_b - \Delta P_a = P_{lum} - P_{ext}, \quad [7]$$

which is proportional to a water flux into the lumen in the absence of osmotic gradients and tight junctions. To generate water influx into the lumen (corresponds to $\Delta P_b - \Delta P_a > 0$), stiffness of the actin network at the apical side K_a has to increase or the elongation factor ξ_a is decreasing, making ΔP_a smaller in Equation (5). But during lumen expansion the apical cortex sufficiently elongates, and thus, to facilitate water influx, actin network must stiffen, for example through densification or crosslinking between actin filaments.

In Supplementary Methods Fig. 3C we plot the predicted dependence of the lumen growth rate on both cortex stiffness (K_a) and undeformed length factor (ξ_a) assuming constant strain in the cortex ($\frac{L_b}{\widetilde{L_b}} = 1, \frac{L_a}{\widetilde{L_a}} = 12$). Our model predicts that increasing undeformed length factor (ξ_a) leads to decreased stress on the apical side and, as a result, the pressure difference also decreases, whereas increasing stiffness (K_a) leads to the opposite effect and lumen expansion is predicted to be faster. Since it is experimentally challenging to measure the actual stiffness and the undeformed

length factor in the cortex, we expect that they are both increased but stiffness increase outcompetes any increase in undeformed length factor to drive lumen growth.

Overall, the above model predictions allow us to conclude that (i) apical actin polymerization, associated with actin network stiffening, may promote lumen growth in smaller epiblasts, (ii) cell size and cell contact or cleft length remain constant during lumen growth, which we verified experimentally, and (iii) in larger epiblasts, lumen pressure is required to balance the pressure from the gel to avoid buckling. To examine the lumen growth at later stages, where lumen pressure is necessary to avoid buckling, we employ a model for pressure-driven lumen growth that accounts for ion and water fluxes through the cell layer and the intercellular space and results in pressure gradients sufficient to drive lumen growth.

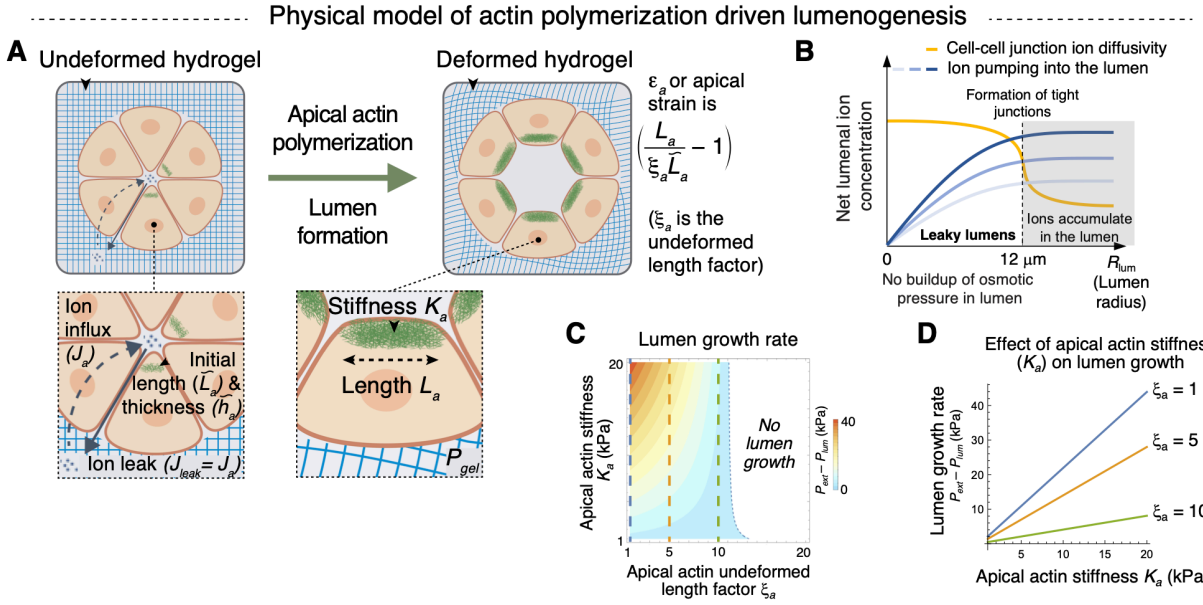

Supplementary Methods Fig. 3: Physical model of lumen growth in small hiPSC epiblasts. **(A)** Schematic of the theoretical model of actin polymerization driven lumen growth. $\tilde{L}_a$: initial length of apical actin mesh; L_a: apparent length of apical actin mesh; ξ_a: undeformed length factor; K_a: stiffness of apical actin mesh; J_a: ion flux into lumen; J_{leak}: ion leak along the leaky junctions; P_{gel}: stress exerted by the hydrogel on the cell cluster. **(B)** Model shows that osmotic pressure does not build in leaky lumens. Ions pumped into the lumen diffuse out along the leaky junctions in smaller epiblasts preventing buildup of osmotic pressure. **(C and D)** Plots showing that increase in apical actin stiffness (K_a) and decrease in undeformed length factor (ξ_a) result in higher lumen

growth rates. Lumen growth rates as a function of apical actin stiffness (K_a) for given values of undeformed length factor (ξ_a) are shown in (C). All other parameters were kept constant. $h_a = h_b = 0.6$ μm, $R_{cell} = 6$ μm, $L_a/\tilde{L}_a = 12$, $L_b/\tilde{L}_b = 1$.

B. Pressure driven lumen growth in larger hiPSC epiblasts

Since formation of tight junctions between cells is observed only in hiPSC epiblasts larger than 12 μm, the permeability of clefts to ions and water is high in small lumens, preventing the accumulation of ions in the lumen. As epiblasts grow larger and tight junctions become functional, the ion concentration in the lumen increases, surpassing that in the external media. This establishes a concentration gradient across the cell layer, leading to water influx into the lumen, elevated osmotic pressure and lumen expansion (Supplementary Methods Fig. 4A). In this section, we investigate lumen expansion in larger epiblasts that exhibit growth despite increased pressure from the surrounding hydrogel. Our model incorporates passive ion and water transport, active ion pumping, and cell mechanics to predict equilibrium lumen size and cell shape (Supplementary Methods Fig. 4B). Our findings reveal an interplay between fluid and ion flows through the cell membrane and clefts, and its influence on lumen formation.

Ion transport in the lumen and cells

The change in the total number of ions in the cell is proportional to the total ion flux across the cellular membrane. The ion transport includes passive fluxes due to the difference in the osmotic pressure between the two sides of cell membrane, and the active fluxes that are provided through selective ion transport by ion pumps. The equilibrium osmotic pressure, Π, is related to the molar concentration, c, and the number of ions, N^i, by van't Hoff's equation as $\Pi = RTc = RTN^i/V$, where R is the gas constant, T is the temperature, and V is the volume. Due to the apical-basal polarity in cells, the active fluxes are directional, and, in general, they are different at the basal and apical sides. The change in the number of ions in the cell is given by

$$d_t N^i_{cell} = J^i_b - J^i_a - 2J^i_c \,, \qquad [8]$$

where $J^i_b = L_b(\omega\Delta\Pi_b + j_b), J^i_a = L_a(\omega\Delta\Pi_a + j_a), J^i_c = L_c\omega\Delta\Pi_c$ are the fluxes through the basal, apical and cleft side, respectively. The osmotic pressure differences, $\Delta\Pi_b = \Pi_{ext} - \Pi_{cell}$, $\Delta\Pi_a = \Pi_{cell} - \Pi_{lum}$, $\Delta\Pi_c = \Pi_{cell} - \Pi_{cleft}$ determine the passive ion transport through the cell membrane

with ion permeability ω. The osmotic pressure inside the cleft can be averaged as $\Pi_{cleft} = (\Pi_{lum} + \Pi_{ext})/2$. The density of ion pumps and pumping rate, j_a, j_b on both sides are assumed to be constant. Then total flux through a particular side of the cell is proportional to the respective lengths, L_b, L_a, L_c for the basal, apical, and cleft sides.

The change in the total number of ions, N^i_{lum} in the lumen is determined by the difference between influx of ions through the apical side of the cell and the leakage of ions through the clefts:

$$d_t N^i_{lum} = J^i_a - J^i_{leak}\,, \qquad [9]$$

where the ion leak through the cleft is assumed to be proportional to the difference in concentrations between the lumen and the external solution, and it also depends on the ion diffusivity D and the cleft width h_c as $J^i_{leak} = \frac{D\,h_c}{L_c}(c_{lum} - c_{ext})$.

Lumen and cell size regulation

Due to the water incompressibility, the cell and lumen sizes change proportional to the total amount of water fluxes. The change in the cell size is then given by fluxes through the cell membrane

$$d_t A_{cell} = J^w_b - J^w_a - 2J^w_c \qquad [10]$$

The water fluxes are passive and defined by hydrostatic, ΔP, and osmotic pressure, $\Delta\Pi$, differences across the corresponding side of the cell membrane. Assuming that water permeability through the cell membrane, Λ_m, is constant, the fluxes through the basal, apical and cleft sides are $J^w_b = L_b\Lambda_m(\Delta \mathrm{P}_b - \Delta\Pi_b)$, $J^w_a = L_a\Lambda_m(\Delta \mathrm{P}_a - \Delta\Pi_a)$, and $J^w_c = L_c\Lambda_m(\Delta \mathrm{P}_c - \Delta\Pi_c)$, where $\Delta P_b = P_{ext} - P_{cell}$, $\Delta P_a = P_{cell} - P_{lum}$, and $\Delta P_c = P_{cell} - P_{cleft}$.

The change in the lumen size is proportional to the sum of water fluxes through the apical side and the leakage through the cleft

$$d_t A_{lum} = J^w_a - J^w_{leak}\,, \qquad [11]$$

where $J^w_{leak} = \frac{\Lambda_{leak}\,h_c}{L_c}(\Delta P_{leak} - \Delta\Pi_{leak})$, $\Delta P_{leak} = P_{lum} - P_{ext} = -\Delta P_b - \Delta P_a$ and $\Delta\Pi_{leak} = \Pi_{lum} - \Pi_{ext} = -\Delta\Pi_b - \Delta\Pi_a$. The water leak through the cleft depends on permeability of the intercellular gap Λ_{leak} to water and it can be different from the cell membrane permeability Λ_m.

Stresses in the cortical layer and in the gel depend on pressure differences and determine the lumen size

The hydrostatic pressure difference between the cell and external medium is determined by the Laplace law that relates the tension along the cell surface γ, and the curvature radius of the cell R with the pressure difference as $\Delta P = \frac{2\gamma}{R}$. Since the plasma membrane is a fluid-like structure, we assume that only stresses in the comparatively stiff cell cortex contribute to the tension γ.

The cortical stress on the apical side has passive, σ_a^p, and active, σ_a^a, components and can be written as

$$\sigma_a = \sigma_a^p + \sigma_a^a = \frac{R_a}{2h}\Delta P_a \ , \qquad [12]$$

where R_a is the curvature radius of the side, and h is the cortex thickness. The active stress arises due to the actomyosin-mediated contractility in the cortex, and it is assumed to be constant. The passive stress is caused by external load and for simplicity it can be assumed to be linearly proportional to the strain on the apical side,

$$\sigma_a^p = \frac{K_a}{2}\left(\frac{L_a}{\zeta_a L_a^{ini}} - 1\right) , \qquad [13]$$

where K_a is the stiffness of the cortical layer at the apical side, L_a, L_a^{ini} are the actual and the initial lengths of the apical side, respectively. The passive stress also depends on the polymerization on the apical side, which increases the reference length of this side by factor $\zeta_a \geq 1$.

The stress on the basal side can be written as

$$\sigma_b = \sigma_b^p + \sigma_b^a = -\frac{R_b}{2h}(\Delta P_b + \sigma_{gel}) , \qquad [14]$$

where σ_b^a is the constant active stress and $\sigma_b^p = \frac{K_b}{2}\left(\frac{L_b}{L_b^{ini}} - 1\right)$ is the passive stress at the basal side, K_b is the stiffness of the cortical layer, L_b, L_b^{ini} are the actual and the initial lengths of the basal side, respectively. The compressive stress from the gel, σ_g , acts in addition to the external pressure and increases the hydrostatic pressure in the cell. The normal stress on the basal side due to deformations in the gel with effective stiffness E_g is proportional to the increase in the lumen size and given by

$$\sigma_{gel} = E_{gel}\varepsilon_{gel} = \frac{E_{gel}}{2}\left(\frac{R_b}{R_b^{ini}} - 1\right) . \qquad [15]$$

This acts to decrease the surface tension caused by the pressure difference across the basal side and builds up a higher hydrostatic pressure in the cell. In the initial state, when there are no passive stresses ($\sigma_b^p = 0, \sigma_{gel} = 0$), there still has to be a small unavoidable hydrostatic pressure difference $\Delta P_b = -\frac{2h\sigma_b^a}{R_b^{ini}}$ required to balance the constant active stress produced by myosin motors.

We note that the assumption of the material as linearly elastic is a simplification of the viscoelastic and viscoplastic gels used in the experimental studies. We expect that our fundamental findings from the models would still hold, though the stresses remaining in the gel following lumen opening and hiPSC epiblast expansion would be expected to relax in the experimental condition.

The cell shape and the number of cells (n_{cells}) in a perfectly symmetrical epiblast is defined by the sector angle $\phi = 2\pi/n_{cells}$. In larger hiPSC epiblasts with increased number of cells, each individual cell occupies a smaller sector but the lumen size increases. The curvature of the cell membrane on the basal side ($1/R_b$) depends on the apparent radius of the epiblast, whereas the apical curvature is assumed to be small, similar to the experimental observations.

Thus, the hydrostatic pressure differences ΔP_b and ΔP_a depend both on the stresses in the cortex and in the gel that are defined by the lumen and cell sizes A_{lum}, A_{cell}, the number of cells n, and the curvature radius R_a at the apical side.

Simulation results for larger lumens

Larger epiblasts primarily grow due to increasing osmotic pressure in the lumen because apical actin polymerization becomes stabilized and compression from the surrounding gel exceeds the buckling threshold. Here, we investigate the role of active ion pumping in determining lumen size.

The mechanical equilibrium lumen size at constant number of cells depends both on apical and basal ion pumping (Supplementary Methods Fig. 4C). For an epiblast consisting of 8 cells, the model predicts that the lumen forms only if there is a sufficient amount of ion influx into the cell through the basal side (>0.3×10^{-6} M/m^2/s). This generates the necessary osmotic pressure in the cell, which maintains the cell size, cleft length and also increases the passive ion transport into the lumen. For basal ion pumping slightly above the minimal threshold (>0.3×10^{-6} M/m^2/s), small lumens exist even without active pumping through the apical side. However, higher levels of basal ion pumping at small apical pumping restricts the lumen formation (purple region in Supplementary Methods Fig. 4C) due to the large ion concentration in the cell that significantly increases accumulation of water in the cell and leads to increased cell size and higher pressure from the hydrogel. In addition, the osmotic pressure difference on the apical side becomes much larger than the hydrostatic pressure difference, leading to transport of water from the lumen into the cell and preventing lumen formation.

In the other limit, when ion pumping on apical side is greater than that on the basal side, the model predicts a reduction in cell size due to decreasing osmotic pressure in the cells. As a result, the cleft length decreases and ions easily leak from the lumen, preventing lumen formation (green region in Supplementary Methods Fig. 4C).

In the intermediate regime at high enough basal ion pumping that is balanced by leakage and pumping ions out of the cell through the apical side, the lumen size is shown to be strongly dependent on the ratio between active transport on both sides. Interestingly, lumens are predicted to become larger with increasing pumping through the basal side because it intensifies the passive ion leak into the lumen, and it also increases the size of cleft and cell. Whereas dependence of lumen growth on pumping across the apical side is also influenced by the pumping rate through basal side. When basal ion pumping is relatively small, lumens are predicted to become larger with increase in apical pumping. However, at higher basal pumping levels, lumens become smaller with increase in apical pumping.

In order to capture the experimental observations in large hiPSC epiblasts, our model was employed to predict lumen growth in a scenario characterized by a substantial increase in the number of cells. For that, we fixed the number of cells and allowed the system to grow to an equilibrium size while keeping the rest apical and basal lengths constant (the rest lengths in undeformed state correspond to the case with 8 cells in the cluster). In Fig. 4D of Supplementary Methods, we present the model predictions for the number of cells and cell apical area depending on the lumen radius. The simulation results are in an excellent agreement with our experimental observations and indicate that in large epiblasts, cells necessitate rapid proliferate, even though the apical area of individual cells remains relatively constant. This behavior sharply contrasts with that in smaller epiblasts where cells require intensive growth and stiffening at the apical side to facilitate lumen expansion. This again indicates that in matured epiblasts, apical growth alone is insufficient to drive lumen growth, and that there must be lumenal osmotic pressure that surpasses the pressure exerted by the surrounding gel and also promotes cell division due to the stretching in the cell layer. Physical parameters used in our model are listed in Supplementary Methods Table 1.

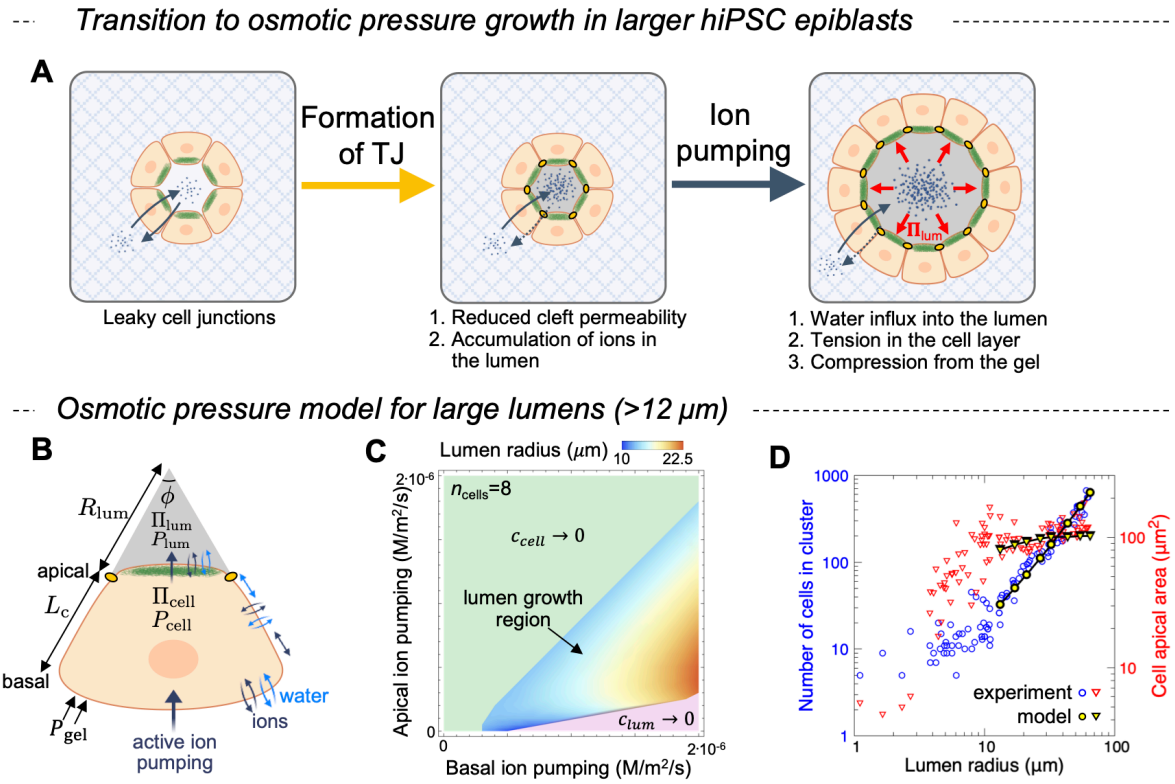

Supplementary Methods Fig. 4: Physical model of osmotic pressure driven lumen growth in large hiPSC epiblasts. (A) Summary of lumen growth mechanism in larger hiPSC epiblasts. **(B)** Schematics of the cell and lumen geometry in the model for osmotic pressure driven lumen growth. **(C)** Model predictions for the dependence of lumen size on ion pumping through the basal and apical sides of the cells. The region of predicted lumen growth (colored domain) is limited by regions where lumens do not form due lack of ions in the cell (green region) or in the lumen (purple region). **(D)** Model predictions (black circles and triangles) closely match our experimental observations for the lumen radius, number of cells and cell apical surface area in larger epiblasts.

Parameter	Description	Value
R_{cell}	initial cell radius [μm]	6
R_b^{ini}	initial epiblast size [μm]	12
L_c^{ini}	initial cleft length [μm]	12
h_c	cleft width [nm]	20
σ_a^a, σ_b^a	active cortical stress [Pa]	100
P_{ext}	external hydrostatic pressure [kPa]	100
c_{ext}	external ion concentration [mM]	300
ω	ion permeability of the cell membrane [mol.m^{-2}s^{-1}Pa^{-1}]	1.5×10^{-9}
D	ion diffusivity in the cleft [m^{2}s^{-1}]	2×10^{-9}
Λ_m	water permeability of the cell membrane [mol.m^{-2}s^{-1}Pa^{-1}]	7×10^{-12}
Λ_{leak}	water permeability of the cleft [mol.m^{-2}s^{-1}Pa^{-1}]	2×10^{-14}
K_b	effective stiffness of the cortical layer at basal side [kPa]	6
$h_{a,b}$	cortical layer thickness [μm]	0.6
E_{gel}	Young's modulus of the hydrogel [kPa]	1
E	Young's modulus of the cell monolayer [kPa]	20

Supplementary Methods Table 1: Model parameters

In our experiments, measured cell volume lies in the range of $1000 - 1500\ \mu m^3$, from which we ascertain lower value $R_{cell} = 6\ \mu m$ for cells of spherical shape. Assuming that epiblast development starts with a single cell, the initial epiblast size can be estimated as $R_b^{ini} = 12\ \mu m$. Our experiments demonstrated that cell layer thickness remains constant, thus the reference cleft length corresponds to the cell size $L_c^{ini} = 12\ \mu m$. The intercellular cleft width lies in the range of $10 - 20\ nm$, for which we use upper value in our computations [S5]. Experimentally reported values for cortex tension in progenitor cells were estimated [S6] as $\approx 50\ pN/\mu m$, leading to cortical stress value $\sigma^a \approx 100\ Pa$. We use membrane leak channel ion permeability $\omega \approx 1.5 \times 10^{-9}$, following McEvoy et al. [S7], obtained under assumption that fluxes through leak channels and active pumping are of the same order. Approximate diffusion coefficients for K^+, Na^+ and Cl^- ion species in water at 25° C lie in the range [S8] of $1.33 - 2.03 \times 10^{-9}\ m^2/s$. Assuming solvent permeability of the lipid membranes lies within the range [S9] of $10^{-5} - 10^{-4}\ m/s$, the upper value for water permeability factor can be estimated as $\Lambda_m \approx 7 \times 10^{-12}$.

The cortical layer stiffness $K_{a,b}$ has been reported to vary [S10, S11] from $0.1 - 100\,kPa$, depending on type of measurements, for which we assume the reference value $6\,kPa$. The thickness of cortical layer has been shown to depend on mechanical state of the cell [S12, S13], and lies within the range $0.1 - 0.6\,\mu m$, from which we assume the upper value. Our mechanical characterization of viscoelastic alginate hydrogels performed at 10% compressive strain demonstrated final relaxed modulus of ~1 kPa, that we use as the reference value for E_{gel}. We assumed the apparent Young's modulus of the cell monolayer as $E = 20$ kPa, following Harris et al. [S4], where Young's modulus of MDCK cell monolayers were quantified. Although direct measurements of this value were not conducted in our experiments, we hypothesize that mechanical properties of MDCK cell monolayers are likely to align closely with those of hiPSC epiblasts.

References

S1. Zhou, F., Wang, R., Yuan, P., Ren, Y., Mao, Y., Li, R., Lian, Y., Li, J., Wen, L., Yan, L., et al. (2019). Reconstituting the transcriptome and DNA methylome landscapes of human implantation. Nature *572*, 660-664. 10.1038/s41586-019-1500-0.

S2. Xiang, L., Yin, Y., Zheng, Y., Ma, Y., Li, Y., Zhao, Z., Guo, J., Ai, Z., Niu, Y., Duan, K., et al. (2020). A developmental landscape of 3D-cultured human pre-gastrulation embryos. Nature *577*, 537-542. 10.1038/s41586-019-1875-y.

S3. Trushko, A., Di Meglio, I., Merzouki, A., Blanch-Mercader, C., Abuhattum, S., Guck, J., Alessandri, K., Nassoy, P., Kruse, K., Chopard, B., and Roux, A. (2020). Buckling of an Epithelium Growing under Spherical Confinement. Developmental Cell *54*, 655-668.e656. https://doi.org/10.1016/j.devcel.2020.07.019.

S4. Harris, A.R., Peter, L., Bellis, J., Baum, B., Kabla, A.J., and Charras, G.T. (2012). Characterizing the mechanics of cultured cell monolayers. Proceedings of the National Academy of Sciences *109*, 16449-16454. doi:10.1073/pnas.1213301109.

S5. Hou, J. (2020). Chapter 1 - Introduction. In A Laboratory Guide to the Tight Junction, J. Hou, ed. (Academic Press), pp. 1-32. https://doi.org/10.1016/B978-0-12-818647-3.00001-5.

S6. Krieg, M., Arboleda-Estudillo, Y., Puech, P.H., Käfer, J., Graner, F., Müller, D.J., and Heisenberg, C.P. (2008). Tensile forces govern germ-layer organization in zebrafish. Nature Cell Biology *10*, 429-436. 10.1038/ncb1705.

S7. McEvoy, E., Han, Y.L., Guo, M., and Shenoy, V.B. (2020). Gap junctions amplify spatial variations in cell volume in proliferating tumor spheroids. Nature Communications *11*, 6148. 10.1038/s41467-020-19904-5.

S8. Yuan-Hui, L., and Gregory, S. (1974). Diffusion of ions in sea water and in deep-sea sediments. Geochimica et Cosmochimica Acta *38*, 703-714. https://doi.org/10.1016/0016-7037(74)90145-8.

S9. Marrink, S.-J., and Berendsen, H.J.C. (1994). Simulation of water transport through a lipid membrane. The Journal of Physical Chemistry *98*, 4155-4168. 10.1021/j100066a040.

S10. Poh, Y.-C., Chowdhury, F., Tanaka, T.S., and Wang, N. (2010). Embryonic Stem Cells Do Not Stiffen on Rigid Substrates. Biophysical Journal *99*, L19-L21. 10.1016/j.bpj.2010.04.057.

S11. Sthanam, L.K., Barai, A., Rastogi, A., Mistari, V.K., Maria, A., Kauthale, R., Gatne, M., and Sen, S. (2017). Biophysical regulation of mouse embryonic stem cell fate and genomic integrity by feeder derived matrices. Biomaterials *119*, 9-22. https://doi.org/10.1016/j.biomaterials.2016.12.006.

S12. Kumar, R., Saha, S., and Sinha, B. (2019). Cell spread area and traction forces determine myosin-II-based cortex thickness regulation. Biochimica et Biophysica Acta (BBA) - Molecular Cell Research *1866*, 118516. https://doi.org/10.1016/j.bbamcr.2019.07.011.

S13. Clark, Andrew G., Dierkes, K., and Paluch, Ewa K. (2013). Monitoring Actin Cortex Thickness in Live Cells. Biophysical Journal *105*, 570-580. 10.1016/j.bpj.2013.05.057.